

**THE EFFECT OF DISSOLUTION ON
MICROSTRUCTURE OF MAGNESIUM OXIDE
THIN FILM**



**A Thesis Submitted in Partial Fulfillment of the Requirements for
the Degree of Doctor of Philosophy in Materials Engineering**

Suranaree University of Technology

Academic Year 2019

ผลกระทบของการละลายที่มีผลต่อโครงสร้างทางจุลภาคของฟิล์มบาง
แมกนีเซียมออกไซด์



นางสาวสิริพร ชิกันทา

วิทยานิพนธ์นี้เป็นส่วนหนึ่งของการศึกษาตามหลักสูตรปริญญาวิศวกรรมศาสตรดุษฎีบัณฑิต
สาขาวิชาวิศวกรรมวัสดุ
มหาวิทยาลัยเทคโนโลยีสุรนารี
ปีการศึกษา 2562

**THE EFFECT OF DISSOLUTION ON MICROSTRUCTURE OF
MAGNESIUM OXIDE THIN FILM**

Suranaree University of Technology has approved this thesis submitted in partial fulfillment of the requirements for the Degree of Doctor of Philosophy.

Thesis Examining Committee



(Dr. Somchai Tancharakorn)

Chairperson



(Assoc. Prof. Dr. Soodkhet Pojprapai)

Member (Thesis Advisor)



(Dr. Pinit Kidkhunthod)

Member (Thesis Co-Advisor)



(Dr. Laddawan Supadee)

Member



(Dr. Narong Chanlek)

Member



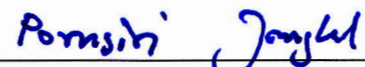
(Assoc. Prof. Dr. Sukanda Jiansirisomboon)

Member



(Assoc. Prof. Dr. Sirirat Rattanachan)

Member



(Assoc. Prof. Dr. Pornsiri Jongkol)



(Assoc. Prof. Ft. Lt. Dr. Kontorn Chamniprasart)

Vice Rector for Academic Affairs
and Internationalization

Dean of Institute of Engineering

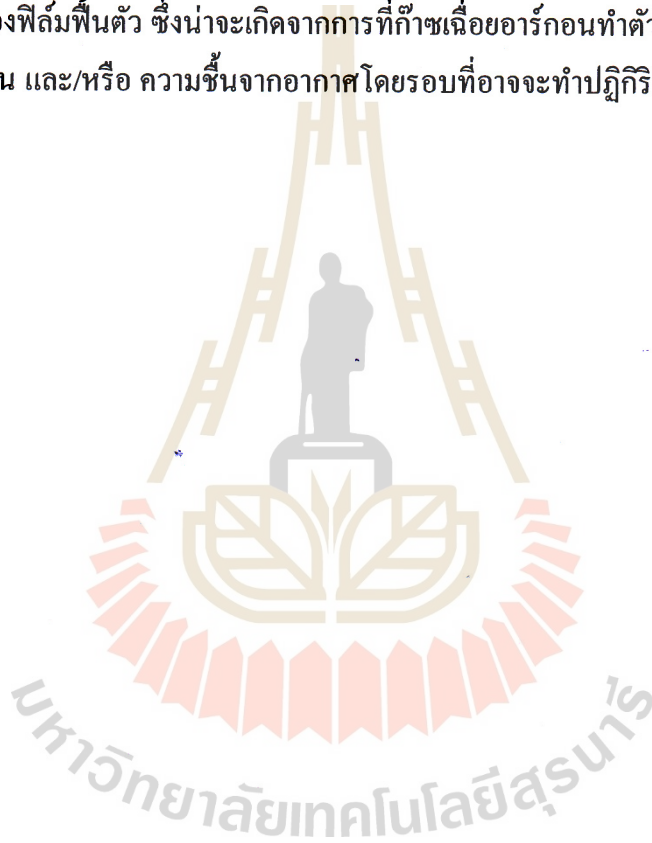
สิริพร ชิกันทา : ผลกระทบของการละลายที่มีผลต่อโครงสร้างทางจุลภาคของฟิล์มบางแมกนีเซียมออกไซด์ (THE EFFECT OF DISSOLUTION ON MICROSTRUCTURE OF MAGNESIUM OXIDE THIN FILM) อาจารย์ที่ปรึกษา : รองศาสตราจารย์ ดร. สุกเขตต์ พจน์ประไพ, 116 หน้า.

การลดลงของความหนาของฟิล์มบางแมกนีเซียมออกไซด์ (MgO thin film) เนื่องจากการละลายน้ำในระหว่างกระบวนการผลิต เป็นปัญหาร้ายแรงสำหรับเซนเซอร์แม่เหล็กที่ใช้ฟิล์มบางแมกนีเซียมออกไซด์เป็นส่วนประกอบ อาทิ เซนเซอร์หัวอ่านฮาร์ดดิสก์ไดรฟ์ (Hard disk drives, HDDs) ดังนั้นวิทยานิพนธ์นี้จึงมีวัตถุประสงค์เพื่อตรวจสอบพฤติกรรมการละลายและการคายน้ำของฟิล์มบางแมกนีเซียมออกไซด์

ในส่วนแรก วิทยานิพนธ์นี้ได้ศึกษาถึงอิทธิพลของบรรยากาศก๊าซต่าง ๆ เช่น ก๊าซไนโตรเจน (N_2) ก๊าซออกซิเจน (O_2) และก๊าซคาร์บอนไดออกไซด์ (CO_2) ที่มีผลต่อพฤติกรรมการละลายของฟิล์มบางแมกนีเซียมออกไซด์ ผลจากการวิจัยพบว่า ฟิล์มบางแมกนีเซียมออกไซด์ดูดซับโมเลกุลของน้ำเข้าสู่ชั้นในของฟิล์มและเปลี่ยนองค์ประกอบทางเคมีเป็นแมกนีเซียมไฮดรอกไซด์ ($Mg(OH)_2$) และเมื่อชั้นไฮดรอกไซด์เหล่านี้ได้สัมผัสกับน้ำ จะเกิดการละลายโดยการปล่อยแมกนีเซียมไอออน (Mg^{2+}) และไฮดรอกไซด์ไอออน (OH^-) ลงสู่น้ำ ส่งผลให้ความหนาของฟิล์มบางแมกนีเซียมออกไซด์ลดลง โดยพบว่าความหนาของฟิล์มจะลดลงเพียงเล็กน้อยภายใต้บรรยากาศก๊าซไนโตรเจนและออกซิเจน แต่จะลดลงอย่างมากในการละลายภายใต้บรรยากาศก๊าซคาร์บอนไดออกไซด์ สาเหตุเนื่องมาจากก๊าซคาร์บอนไดออกไซด์ทำปฏิกิริยากับน้ำและสร้างกรดคาร์บอนิก (H_2CO_3) และ/หรือกรดไบคาร์บอเนต (HCO_3^-) ขึ้น ส่งผลให้ความเป็นกรดต่างของน้ำลดลง ดังนั้นอัตราการละลายของฟิล์มบางแมกนีเซียมออกไซด์ภายใต้ก๊าซคาร์บอนไดออกไซด์จึงสูงกว่าก๊าซออกซิเจนและไนโตรเจน ที่ไม่มีการสร้างปฏิกิริยากับน้ำ

เพื่อเพิ่มความเข้าใจพฤติกรรมการละลายของฟิล์มบางแมกนีเซียมออกไซด์ให้มากขึ้น ในส่วนต่อมา วิทยานิพนธ์นี้จึงได้ศึกษาเกี่ยวกับอิทธิพลของอุณหภูมิของน้ำต่อการละลายของฟิล์มบางแมกนีเซียมออกไซด์ จากการศึกษาพบว่านอกจากบรรยากาศก๊าซแล้ว อุณหภูมิของน้ำก็เป็นหนึ่งในตัวแปรที่สำคัญที่สามารถส่งผลต่อพฤติกรรมการละลายได้ โดยผลการทดลองชี้ให้เห็นว่าความหนาของฟิล์มแมกนีเซียมออกไซด์จะลดลงมากขึ้น เมื่อเพิ่มอุณหภูมิของน้ำ เนื่องจากการเพิ่มขึ้นของอุณหภูมิของน้ำ จะส่งผลให้พลังงานจลน์ของโมเลกุลของน้ำสูงขึ้น จึงนำไปสู่อัตราการละลายที่สูงขึ้น

นอกเหนือจากการศึกษาปฏิกิริยาการละลายของฟิล์มบางแมกนีเซียมออกไซด์แล้ว ในวิทยานิพนธ์นี้ยังแสดงให้เห็นถึงพฤติกรรมการคายน้ำของฟิล์มบางแมกนีเซียมออกไซด์ โดยผลจากการศึกษาชี้ให้เห็นว่าฟิล์มบางจะสร้างกลุ่มก้อนขึ้นมาจากผิวฟิล์มหลังจากที่ถูกเปิดให้สัมผัสกับความชื้นเป็นเวลา 24 ชั่วโมง ส่งผลให้ความหนาและความหนาของฟิล์มเพิ่มขึ้น แต่อย่างไรก็ตามหลังจากที่ฟิล์มถูกอบอ่อน (Anneal) ที่สภาวะต่างๆ แล้ว จำนวนของกลุ่มก้อน ความหนาของผิวและความหนาของฟิล์มกลับลดลง เมื่ออุณหภูมิถูกเพิ่มสูงขึ้น โดยจะพบว่าที่การอบอ่อนที่ 400 องศาเซลเซียส ภายใต้บรรยากาศก๊าซอาร์กอน จะมีประสิทธิภาพสูงที่สุดในการที่จะทำให้ความหนาผิวและความหนาของฟิล์มพื้นผิว ซึ่งน่าจะเกิดจากการที่ก๊าซเฉื่อยอาร์กอนทำตัวเสมือนชั้นที่ปกป้องผิวฟิล์มจากสิ่งเจือปน และ/หรือ ความชื้นจากอากาศโดยรอบที่อาจจะทำปฏิกิริยากับฟิล์มในระหว่างที่ฟิล์มถูกอบอ่อน



สาขาวิชา วิศวกรรมเซรามิก

ปีการศึกษา 2562

ลายมือชื่อนักศึกษา Sun Tung

ลายมือชื่ออาจารย์ที่ปรึกษา [Signature]

ลายมือชื่ออาจารย์ที่ปรึกษาร่วม นง กัญญา

SIRIPORN TIGUNTA : THE EFFECT OF DISSOLUTION ON
MICROSTRUCTURE OF MAGNESIUM OXIDE THIN FILM. THESIS
ADVISOR : ASSOC. PROF. SOODKHET POJPRAPAI, Ph.D., 117 PP.

MAGNESIUM OXIDE/THIN FILM/MAGNETIC TUNNELING
JUNCTIONS/DISSOLUTION/DEHYDRATION

Dissolution of the magnesium oxide (MgO) thin film in water during the manufacturing process can thin the thickness of the film. This is a critical problem for magnetic sensors containing MgO thin film such as the read head sensors of hard disk drives (HDDs). Therefore, this thesis aims to investigate the dissolution and dehydration behavior of the MgO thin film.

The thesis first investigates the influence of the gas atmospheres including nitrogen gas (N₂), oxygen gas (O₂) and carbon dioxide gas (CO₂) on the dissolution behavior of the MgO thin film. Results reveal that the MgO thin film absorbs molecules of water into its inner layer and transforms its chemical composition into Mg(OH)₂ after being exposed to deionized water. These Mg(OH)₂ layers could dissolve by releasing Mg²⁺ ions and OH⁻ ions into water resulting in the decrease of the film thickness. It is found that the thickness of the film slightly decreases in the sample with N₂ and O₂ atmosphere while that decreases considerably in sample with CO₂ atmosphere. This is because CO₂ reacts with water and generates carbonic acid (H₂CO₃) and/or bicarbonate acid (HCO₃⁻) leading to the reduction of pH. Consequently, the dissolution rate of the film under CO₂ atmosphere is much faster than that under O₂ atmosphere while N₂ has no reaction with water.

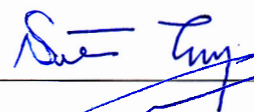
To expand our understanding of the dissolution behavior of the MgO thin film, the effect of water temperature on the dissolution of the film was investigated. It is found that temperature is one of the crucial factors that strongly influence the dissolution behavior of the film. Results reveal that the thickness of the film decreases with an increase in water temperature. This is because the increase of water temperature can increase the kinetic energy of water molecules leading to an increase in the dissolution rate of the film.

Besides the investigation of the dissolution reaction of the MgO thin film, this thesis demonstrates the dehydration behavior of the MgO thin film. Results indicate that the MgO thin film creates clusters over its surface after being exposed to a humid environment for 24 hours. This results in an increase of surface roughness and thickness of the film. However, after the films were annealed at various conditions, the number of clusters and the surface roughness and thickness of the film decreased with an increase of the annealing temperature. It is found that the annealing at 400°C in Ar atmosphere efficiently recovers the surface roughness and thickness of the MgO thin film. The possible reason could be that the inert Ar gas may act as a protective layer that prevents contamination and/or humidity from the air which may react with the film during the annealing.

School of Ceramics Engineering

Academic Year 2019


Student's Signature



Advisor's Signature



Co-Advisor's Signature



ACKNOWLEDGEMENTS

The work in this dissertation could not have been performed and completed without the supports of many people, whom I would like to express my deepest gratitude at this time.

First of all, I would like to express my sincere acknowledgment to the Thailand Research Fund (TRF) and Synchrotron Light Research Institute (SLRI) for their joint financial support throughout this study through the Royal Golden Jubilee Ph.D. scholarship. Western Digital Co. Ltd. also thanks for providing me the MgO sample throughout this study.

Secondly, I must give a special thanks to my supervisor, Associate Professor Dr. Soodkhet Pojprapai for his guidance and valuable advice throughout every stage of my study at Suranaree University of Technology. I would like to thank my co-supervisors, Dr. Pinit Kidkhunthod, for suggestions and fruitful discussions about X-ray absorption spectroscopy analysis. Also, I would like to extend my appreciation to the committee members, Associate Professor Dr. Sukanda Jiansirisomboon and Associate Professor Dr. Sirirat Rattanachan and especially, the external committee members, Dr. Somchai Tuncharakorn, Dr. Narong Chanlek, Dr. Laddawan Supadee, for their advice, comments and suggestions that useful for this thesis.

Next, my gratitude also goes to Professor Dr. Nagarajan Valanoor for giving me the opportunities to be a visiting student in his group at the University of New South Wales (UNSW) twice. I would also like to give my sincere acknowledgment to Dr. Daniel Sando, Dr. Peggy Zhang and other members of Nagy's group for their warm

welcome, their kindly helps and invaluable knowledge, detailed technical advice in plentiful ways during my visit to UNSW. Thanks to all senior alumni and members of my former research group at Chiang Mai University, especially Associate Professor Dr. Kamonpan Pengpat, my former supervisor, for helping me, giving me advice, supporting me and always counting on me like I am still one of the group members.

Surely, I could never come this far without the endless love, understanding and supports from my lovely family. I would like to thank and dedicate this Ph.D. thesis to my beloved parents, Mr. Sawat and Mrs. Darawan Tigunta. They did not only give me life but also educated me, raised me with much love and care, always believe in me and encourage me to achieve my goals in all possible ways through my entire life.

Lastly, I immensely appreciate the obstacles, the challenges and the hard times through the period of my Ph.D. candidate which strengthened me, taught me the greatest lessons and shaped me into the person like I am today. Without these difficulties, I would never know how strong I can be. I also thank myself for being determined, patient, struggling to overcome those obstacles until I finally achieved it today.

มหาวิทยาลัยเทคโนโลยีสุรนารี

Siriporn Tigunta

TABLE OF CONTENTS

	Page
ABSTRACT (THAI).....	I
ABSTRACT (ENGLISH).....	III
ACKNOWLEDGEMENTS.....	V
TABLE OF CONTENTS.....	VII
LIST OF TABLES.....	XIII
LIST OF FIGURES.....	XIV
SYMBOL AND ABBREVIATIONS.....	XX
CHAPTER	
I INTRODUCTION.....	1
1.1 Significance of the Problem.....	1
1.2 Research Objective.....	3
1.3 Hypotheses.....	3
1.4 Scope of Thesis.....	4
1.5 Usefulness of the Research.....	5
1.6 Outline of Thesis.....	5
1.7 References.....	6
II THEORETICAL BACKGROUND AND	
LITERATURE REVIEW.....	14
2.1 Magnesium Oxide (MgO).....	14

TABLE OF CONTENTS (Continued)

	Page
2.1.1 Properties of Magnesium oxide.....	15
2.1.2 Application of Magnesium Oxide Thin Film.....	16
2.1.3 The Interaction Between the MgO and Water.....	17
2.1.4 The Dehydration Reaction of MgO.....	20
2.2 Magnetic Tunneling Junctions (MTJs).....	21
2.2.1 Tunneling Barrier of MTJs.....	23
2.3 Thin Film Characterization.....	24
2.3.1 X-Ray Photoelectron Spectroscopy (XPS).....	24
2.3.1.1 The Basic Principle of XPS.....	24
2.3.2 X-Ray Absorption Spectroscopy (XAS).....	26
2.3.2.1 The Basic Principle of XAS.....	26
2.3.3 X-Ray Reflectivity (XRR).....	27
2.3.3.1 The Basic Principle of XRR.....	28
2.3.4 Transmission Electron Microscopy (TEM).....	30
2.3.4.1 The Basic Principle of TEM.....	30
2.3.5 A Comparison of Usefulness and Limitation of Each Characterization Technique.....	31
2.4 References.....	32

TABLE OF CONTENTS (Continued)

	Page
III INFLUENCE OF GAS ATMOSPHERE ON	
THE DISSOLUTION BEHAVIOR OF	
MAGNESIUM OXIDE THIN FILM.....	39
3.1 Introduction.....	39
3.2 Experimental Procedure.....	40
3.2.1 Sample Preparation.....	40
3.2.2 Characterizations.....	41
3.3 Results and Discussion.....	43
3.3.1 XPS Results.....	43
3.3.1.1 Thickness of The MgO Thin Film.....	43
3.3.1.2 Formation of Mg(OH) ₂	48
3.3.2 SEM Results.....	54
3.3.3 FIB-SEM Cross-Sectional Result.....	56
3.3.4 Atomic Absorption Spectroscopy (AAS).....	57
3.3.5 Effect of Deionized Water pH.....	59
3.3.6 MgO Dissolution Mechanism.....	61
3.4 Chapter Summary.....	63
3.5 References.....	63

TABLE OF CONTENTS (Continued)

	Page
IV EFFECT OF WATER TEMPERATURE ON THE DISSOLUTION BEHAVIOR OF MAGNESIUM OXIDE THIN FILM.....	69
4.1 Introduction.....	69
4.2 Experimental Procedure.....	70
4.2.1 Sample Preparation.....	70
4.2.2 Characterizations.....	71
4.2.2.1 X-ray Photoelectron Spectroscopy (XPS).....	71
4.2.2.2 Scanning Electron Microscope (SEM).....	72
4.3 Results and Discussion.....	73
4.3.1 Surface Morphology.....	73
4.3.2 Remaining Thickness of the Films.....	74
4.3.3 Depth Profiling of the Film.....	78
4.3.4 Dissolution Mechanism of the MgO Thin Films.....	80
4.4 Chapter Summary.....	82
4.5 References.....	83
V ROLE OF TEMPERATURE AND ATMOSPHERE ON THE DEHYDRATION CHARACTERISTIC OF HYDRATED MAGNESIUM OXIDE THIN FILM.....	86

TABLE OF CONTENTS (Continued)

	Page
5.1 Introduction.....	86
5.2 Experimental Procedure.....	87
5.2.1 Sample Preparation.....	87
5.2.2 Characterizations.....	90
5.2.2.1 Atomic Force Microscopy (AFM).....	90
5.2.2.2 X-Ray Reflectivity (XRR).....	90
5.2.2.3 Transmission Electron Microscopy (TEM).....	90
5.2.2.4 X-Ray Absorption Spectroscopy (XAS).....	90
5.3 Results and Discussion.....	91
5.3.1 Topography of the Film.....	91
5.3.2 Thickness of the Film.....	94
5.3.2.2 X-Ray Reflectivity (XRR).....	94
5.3.2.2 Transmission Electron Microscopy (TEM).....	97
5.3.3 Electronic Structure of the MgO Thin Film.....	100
5.3.4 Dehydration Mechanism of the MgO Thin Film.....	103
5.4 Chapter Summary.....	104
5.5 References.....	104
VI GENERAL DISCUSSION.....	107
6.1 Influence of Gas Atmospheres on the Dissolution in Water of Magnesium Oxide Thin Film.....	107

TABLE OF CONTENTS (Continued)

	Page
6.2 Effect of Water Temperatures on the Dissolution Behavior of Magnesium Oxide Thin Film.....	109
6.3 Role of Temperature and Atmosphere on the Dehydration Characteristic of Magnesium Oxide Thin Film	109
VII CONCLUSION AND FUTURE PERSPECTIVES	111
7.1 General Conclusions.....	111
7.2 Future Perspectives.....	113
APPENDIX I.....	115
BIOGRAPHY.....	117

LIST OF TABLES

Table	Page
2.1	The properties of MgO.....16
2.2	Comparison of advantage and limitation of characterization techniques for analysis the MgO thin film.....32
3.1	Estimation of MgO thin film remaining thickness using various techniques.....46
3.2	The pH values of deionized water obtained before flowing gas after flowing gas, and after the dissolution process.....60
5.1	The thickness of all sample obtained from the fitting of XRR spectra.....96

LIST OF FIGURES

Figure	Page
2.1 Magnesium oxide crystal structure.....	15
2.2 MgO thin film in the read head structure of HDDs.....	17
2.3 Deconvoluted core-level XPS spectra of (a) O <i>1s</i> and (b) Mg <i>2p</i> of the MgO thin films deposited in the different oxygen partial pressures.....	18
2.4 SEM photographs of the MgO thin film sample hydrated for 0 day and 1 day	19
2.5 Mg K-edge XANES of Mg(OH) ₂ evaluated for 5 hours at various temperatures and Mg K-edge of MgO.....	20
2.6 A schematic of a cross-sectional structure of MTJs.....	22
2.7 The magnetoresistance curve of a MTJs.....	23
2.8 Schematic illustration of electron tunneling through an amorphous Al-O barrier and a crystalline MgO barrier.....	24
2.9 Schematic diagram of the XPS process.....	25
2.10 The survey scan and narrow scan of XPS spectra.....	26
2.11 The X-ray absorption spectrum.....	27
2.12 A schematic of X-ray reflectivity measurement set up.....	28
2.13 Schematic diagram showing the specular reflectivity geometry	29
2.14 Reflectivity of the thin film thickness 10 nm and 50 nm.....	29

LIST OF FIGURES (Continued)

Figure	Page
2.15 Schematic of core component of a TEM microscope.....	31
3.1 Schematic diagram of (a) the custom-built fixture cell and (b) the dissolved region of MgO film sample after being exposed to deionized water.....	41
3.2 Schematic diagram of the experimental procedure of the investigation of influence gas atmosphere on the dissolution of MgO thin film.....	42
3.3 High-resolution O 1s spectra after 0, 2, 60, and 120 minutes of sputtering of a pristine MgO thin film.....	43
3.4 XPS depth profile of a pristine MgO thin film.....	45
3.5 Depth distribution of MgO thin film atomic concentrations after being dissolved in deionized water under different gas atmospheres.....	47
3.6 Variation of high-resolution O 1s spectra which obtained from the MgO thin film after being dissolved in deionized water under different gas atmospheres for 1 hour.....	49
3.7 High-resolution O 1s spectra of MgO thin film after being dissolved in deionized water under different gas atmospheres for 4 hours.....	52
3.8 Atomic concentration of Mg(OH) ₂ as a function of sputtering time.....	53

LIST OF FIGURES (Continued)

Figure	Page
3.9 Schematic representation of the remaining thickness of the MgO thin film and the thickness of the Mg(OH) ₂	54
3.10 SEM micrographs (magnification ×10000) of MgO thin films after being dissolved in deionized water.....	55
3.11 FIB-SEM cross-sectional micrographs at three points of the dissolved regions of six MgO thin film samples (Magnification: ×100000).....	56
3.12 The remaining thickness of MgO thin films estimated by FIB-SEM.....	57
3.13 Mg concentration of MgO thin film which dissolved in deionized water under different gas atmospheres.....	58
3.14 Schematic diagram of the dissolution mechanism model of the MgO thin film during being exposed to deionized water.....	62
4.1 Schematic diagram of the experimental procedure of the study of dissolution behavior of the MgO thin film under different temperatures.....	72
4.2 The SEM image of the MgO thin film morphology after exposed to deionized water. (Magnification: ×5000).....	73
4.3 The XPS depth profile of the 20 nm MgO thin film. The black arrow indicates the reference point of the remaining thickness.....	75

LIST OF FIGURES (Continued)

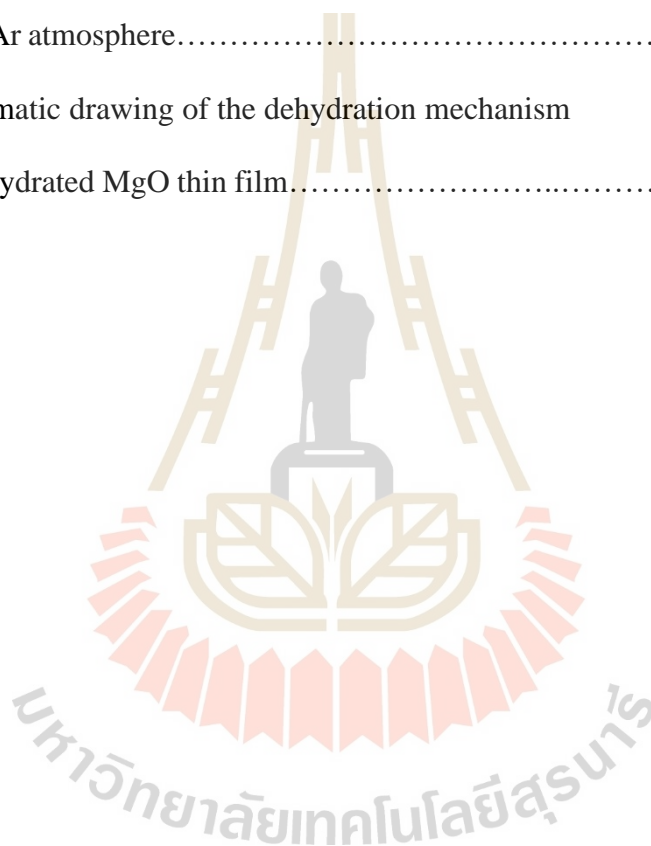
Figure	Page
4.4 A plot of atomic concentration percentage as a function of sputtering time of the MgO thin films after dissolution in deionized water.....	76
4.5 The FIB-SEM cross-sectional of the MgO thin film at different water temperatures. (Magnification: $\times 100K$).....	77
4.6 The deconvoluted O 1s spectra of (a) sample MgO-0, (b) sample MgO-25 and (c) sample MgO-75 at different selected sputtering time.....	78
4.7 A plot of the atomic concentration of $Mg(OH)_2$ of all samples.....	80
4.8 The dissolution model of the MgO thin film after being exposed to deionized water.....	81
5.1 Schematic diagram of the experimental procedure of the investigation of role of temperatures and atmospheres on the dehydration characteristic of magnesium oxide thin film.....	88
5.2 The annealing profile of the MgO thin film.....	89
5.3 The AFM morphology of (a) the pristine MgO thin film and (b) the hydrated MgO thin film (all $10 \times 10 \mu m^2$).....	92
5.4 $10 \times 10 \mu m^2$ AFM scan on the MgO thin film after being annealed at 250, 300, 350, 400°C (a) in air, (b) in N_2 atmosphere and (d) in Ar atmosphere.....	93

LIST OF FIGURES (Continued)

Figure	Page
5.5 The change of surface roughness of the pristine MgO thin film, the hydrated MgO thin film and the films after being annealed in different conditions.....	94
5.6 A comparative of the XRR spectra of the pristine MgO thin film, the hydrated MgO thin film and the film annealed in (a) air, (b) Ar atmosphere and (c) N ₂ atmosphere.....	95
5.7 Thickness of MgO thin films and Mg(OH) ₂ layer after being annealed at 250, 300, 350 and 400°C in air, N ₂ atmosphere and Ar atmosphere.....	97
5.8 High magnification cross-sectional TEM images of (a) the pristine MgO thin film (b) the hydrated MgO thin film.....	98
5.9 The cross-sectional TEM images of MgO thin films after being annealed at 350 and 400°C in air, in N ₂ atmosphere and in Ar atmosphere.....	99
5.10 The normalized Mg K-edge XANES spectra of the MgO thin films annealed in N ₂ atmosphere at different temperatures.....	100
5.11 The normalized Mg K-edge XANES spectra of the MgO thin films annealed in Ar atmosphere at different temperatures.....	101

LIST OF FIGURES (Continued)

Figure	Page
5.12 A comparative Mg K-edge XANES spectra of samples annealed at same annealing temperature in N ₂ atmosphere and in Ar atmosphere.....	102
5.13 A schematic drawing of the dehydration mechanism of the hydrated MgO thin film.....	103



SYMBOLS AND ABBREVIATIONS

λ	=	Inelastic electron mean free path
σ	=	Photoelectric cross-section of the atomic orbital of interest
θ	=	Angular efficiency factor of the instrument
A	=	Area of sample
AAS	=	Atomic absorption spectroscopy
AFM	=	Atomic force microscopy
Al	=	Aluminium
Ar ⁺	=	Argon ion
C	=	Carbon
cm ³	=	Cubic centimeters
CO ₂	=	Carbon dioxide gas
C_{MgO}	=	Concentration of Mg (mg/L)
C_x	=	Atomic concentration of one element in percentage
D	=	Density
eV	=	Electron volts
EXAFS	=	Extended X-ray absorption fine structure
FIB	=	Focus ion beam
FWHM	=	Full width at half maximum
f	=	X-ray flux
F_s	=	Sensitivity factor
Ga ⁺	=	Gallium ion

SYMBOLS AND ABBREVIATIONS (Continued)

H^+	=	Hydrogen ion
H_2O	=	Water
H_2CO_3	=	Carbonic acid
HCO_3^-	=	Bicarbonate
HDDs	=	Hard disk drives
I	=	Intensity
I_i	=	Maximum intensity of a photoelectric peak of each element in sample
I_x	=	Maximum intensity of a photoelectric peak of interested element
M	=	Mass
mA	=	Milliamperes
Mg	=	Magnesium
Mg^{2+}	=	Magnesium ion
min	=	Minutes
mm^2	=	Square millimeters
$MgCO_3$	=	Magnesium carbonate
$Mg(OH)_2$	=	Magnesium hydroxide
MgO	=	Magnesium oxide
MTJs	=	Magnetic tunneling junctions
N	=	Number of atoms per cubic centimeter
N_2	=	Nitrogen gas

SYMBOLS AND ABBREVIATIONS (Continued)

nm	=	Nanometer
O	=	Oxygen
O ₂	=	Oxygen gas
OH ⁻	=	Hydroxide
SEM	=	Scanning electron microscopy
sec	=	Second
Si	=	Silicon
TEM	=	Transmission electron microscopy
TMR	=	Tunneling magnetoresistance
V _{DI}	=	Volume of deionized water
V _s	=	Volume of spherical cap
XANES	=	X-ray absorption near-edge structure
XAS	=	X-ray absorption spectroscopy
XPS	=	X-ray photoelectron spectroscopy
XRR	=	X-ray reflectivity

CHAPTER I

INTRODUCTION

1.1 Significance of the Problem

In the current hard disk drive (HDD) technology, the magnetic tunnel junction (MTJ) structure is a core of the read head sensor of HDDs, requires a thin and a well-oriented texture tunnel barrier thin film (Cai, 2017; Feng, 2010; Hadorn, 2018; Isogami, 2008; Kurt, 2010; Parkin, 2018; Smirnov, 2017; Wisniowski, 2013; Yuasa and Djayaprawira, 2007; Zhu, 2006). This is in order to produce a low resistance-area (RA) and high tunnel magnetoresistance (TMR) which are the most important requirement for achieving high sensitivity read head sensor (Bhutta, 2009; Ikeda, 2008; Yuasa, 2004; Yuasa and Djayaprawira, 2007; Zhu, 2006). However, the fact that, the MgO thin film which is currently used as a tunnel barrier of MTJs structure, is highly sensitive to water (J. H. Lee, 2003b; Singh, 2012). The reaction between magnesium oxide (MgO) thin film and water is nowadays a critical problem occurring in the hard disk drives (HDDs) industry. During exposing to water in the manufacturing process including cleaning, cutting and lapping process, the MgO thin film could naturally absorb the molecules of water to its inner layer and transforms its chemical composition and structure to hexagonal hydroxide $Mg(OH)_2$ (Amaral, 2011; J. H. Lee, 2003a; 2003b). This transformation could lead to the volume expansion, tensile, and compressing stresses formation which results in the producing of porosity, cracking and swelling in MgO thin film (Ali and Al-Mowali, 2013; Amaral, 2011; Dobrzanski, 2020).

Moreover, these hydroxide layers can dissolve by releasing Mg^{2+} and OH^- into water (Amaral, 2010; Amaral, 2011; Hanlon, 2015; Kuenzel, 2018; Rocha, 2004) resulting in an increase of vacancies in the MgO thin film and a decrease of the MgO thin film thickness (Beruto, 1993; Tigunta, 2019). These changes in chemical composition, structure and thickness of the MgO thin film as a result of the hydration and dissolution reaction could reduce the TMR of the MTJs and operating speed of the read head of HDDs. Therefore, it is worthwhile to draw attention on the reaction mechanism between MgO thin film and water especially the dissolution process.

According to the literatures, the factors that can influence the reaction between the MgO and water are the crystallographic orientation of MgO, exposure time, pH, temperature and atmospheres (Aphane, 2009; J. H. Lee, 2003b; Silva, 2013). To obtain more insight into the dissolution reaction of MgO, it is necessary to investigate the reaction between MgO thin film and water under those parameters. To our best knowledge, a lot of studies were performed under various solutions, pH and the normal ambient conditions; however, a few works have reported the effect of temperature on the dissolution of MgO thin film. Furthermore, the influence of gas atmospheres on the degradation of MgO thin film in water has never been addressed in detail. Therefore, in this dissertation, the profound influence of the temperatures and gas atmospheres on the dissolution mechanism of MgO film is investigated. Moreover, the investigation would extend to the dehydration behavior of the MgO thin film because dehydration reaction is the mechanism of water removal (Stanish and Perlmutter, 1983). It is reported that the dehydration reaction could induce the release of water molecules from the hydrated layer resulting in the decrease of the hydroxide layer which forms over the MgO thin film surface and thereby the improvement of the film properties (Gay and

Harrison, 2005; Moon 2007). Understanding dehydration behavior could be used as a guideline to prevent dissolution of the film which leads to the degradation of the magnetic sensors. The experimental conditions of this study were designed to be comparable to assembly processes of magnetic sensors in read heads of HDDs. The profound knowledge obtained from this study can be employed as a guideline to prevent the damage of MgO thin film in the HDD manufacturing process.

1.2 Research Objectives

The main objectives of this dissertation can be summarized as follows:

1.2.1 To investigate the influence of gas atmospheres including oxygen gas (O_2), nitrogen gas (N_2) and carbon dioxide gas (CO_2) on the dissolution behavior of MgO thin films in water.

1.2.2 To determine effect of water temperatures on dissolution behavior of magnesium oxide thin films.

1.2.3 To examine microstructure/crystal structure evolution, surface morphology and thickness of magnesium oxide thin films after being annealed under various annealing conditions.

1.3 Hypotheses

To achieve the objective of this dissertation, the effect of dissolution on microstructure of MgO thin film are determined based on these hypotheses:

1.3.1 The gas could react with water and change chemistry and pH of water affecting the dissolution rate of the MgO thin film. It is possible that the CO_2 gas could

induce the decrease of water pH resulting in an increase of the dissolution rate of the MgO thin film.

1.3.2 Water temperature could relate to the kinetic energy of water. Low temperature of water may reduce the kinetic energy in water resulting in the decrease of dissolution rate in MgO thin film.

1.3.3 The microstructure/crystal structure, surface roughness and thickness of the MgO thin film after being annealed should partially recover as a result of the thermal decomposition of water molecule of magnesium hydroxide.

1.4 Scope of Thesis

The scope of this dissertation relates to the investigation of dissolution and dehydration behavior of the MgO thin film. The experimental procedures were designed to be comparable to the manufacturing processes of MgO. The experiment was set up in three different systems. In the first system, the influence of gas atmosphere on the dissolution of the MgO thin film in water was investigated. The MgO thin film was exposed to deionized water saturated by gas including nitrogen gas (N₂), oxygen gas (O₂) and carbon dioxide gas (CO₂). Then, the morphology, the chemical composition and the thickness of the film were analyzed using the scanning electron microscope (SEM), X-ray photoelectron (XPS) and atomic absorption spectroscopy (AAS). In the second system, the effect of water temperature on the dissolution of the MgO thin film was studied. The MgO thin film was exposed to water droplet at different temperatures of 0, 10, 20, 25, 50 and 75°C. Then, the films were characterized using the SEM and XPS to quantify the chemical composition, thickness and surface morphology of the film. In the final system, the impact of environment on the

dehydration characteristic of the MgO thin film was determined. The MgO thin films were exposed to humid atmosphere for 24 hours before being annealed at different annealing temperatures of 250, 300, 350 and 400°C under different atmospheres (air, N₂ atmosphere, Ar atmosphere). Then, the atomic force microscopy (AFM), x-ray reflectivity (XRR), transmission electron microscopy (TEM) and X-ray absorption spectroscopy (XAS), were used to determined topography, thickness and electronic structure of the film.

1.5 Usefulness of the Research

1.5.1 To understand the effect of gas atmospheres and temperatures on the chemical reaction between water and magnesium oxide thin film.

1.5.2 To understand the relationships between dehydration reaction of magnesium oxide thin film and its physical properties.

1.5.3 To provide a guideline to optimize the atmospheres and temperatures in assembly processes of magnetic sensors in read heads of HDDs

1.6 Outline of Thesis

The remainder of this thesis is built up in the following way:

Chapter 2 provides the theoretical background information of the MgO thin film along with its properties and its applications. This chapter also includes the literature review of the dissolution and dehydration reaction of MgO thin film, the fundamental information of the magnetic tunneling junctions (MTJs) as well as the principle of the characterization techniques used in this study.

Chapter 3 reports the dissolution behavior of the MgO thin film in water. In this chapter, the influence of different gas atmospheres including nitrogen gas (N₂), oxygen gas (O₂) and carbon dioxide gas (CO₂) on the change of the morphology, thickness and chemical composition of the film is demonstrated. In addition, a qualitative model based on the dissolution mechanism of the MgO thin film is proposed.

Chapter 4 reports the effect of water temperature on the dissolution of MgO thin film. This chapter expands the understanding on the dissolution of the MgO thin film. The result of the film dissolved at different water temperatures are discussed. Then, the dissolution model under different temperatures is proposed.

Chapter 5 shows the investigation of the dehydration reaction of MgO thin film. In this chapter, the main focus is on the influence of environmental including annealing temperature and atmosphere on the dehydration characteristic of the MgO thin film. The topography, the chemical composition as well as the thickness of the film is determined. In addition, the dehydration model of the MgO thin film is proposed.

Chapter 6 is the discussion of the major finding related to the influence of gas atmosphere on the dissolution of MgO thin film, the effect of water temperature on the dissolution of the MgO thin film and the role of atmosphere and temperature on the dehydration characteristic of MgO thin film.

The final chapter, **Chapter 7** contains the conclusion of all the findings in this thesis and suggestions for future work.

1.7 References

Ali, A. M., and Al-Mowali, A. H. (2013). Ceramic expansion by water layers on magnesium oxide: AB Initio Study. **Am. J. Mater. Sci.** 1: 50-53.

- Amaral, L. F., Oliveira, I. R., Salomao, R., Frollini, E., and Pandolfelli, V. C. (2010). Temperature and common ion effect on magnesium oxide (MgO) hydration. **Ceram. Int.** 36: 1047.
- Amaral, L. F., Oliveira, I. R., Bonadia, P., Salomao, R., and Pandolfelli, V. C. (2011). Chelants to inhibit magnesia (MgO) hydration. **Ceram. Int.** 37: 1537-1542.
- Aphane, M. E., Merwe, E. M. van der, and Strydom, C. A. (2009). Influence of hydration time on the hydration of MgO in water and in a magnesium acetate solution. **J. Therm. Anal. Calorim.** 96: 987-992.
- Beruto, D., Searcy, A. W., Botter, R., and Giordani, M. (1993). Thermodynamics and kinetics of H₂O(v) chemisorption and solubility in nanometric and single-crystal MgO particles during sintering. **J. Phys. Chem.** 97: 9201-9205.
- Bhutta, K. M., Schmalhorst, J., and Reiss, G. (2009). Study of MgO tunnel barriers with conducting atomic force microscopy. **J. Magn. Magn. Mater.** 321: 3384-3390.
- Brown, Jr., G. E., Henrich, V. E., Casey, W. H., and Clark, D. L. (1999). Metal oxide surfaces and their interactions with aqueous solutions and microbial organisms. **Chem. Rev.** 77-174.
- Cai, J., Fang, B., Wang, C., and Zeng, Z. (2017). Multilevel storage device based on domain-wall motion in a magnetic tunnel junction. **Appl. Phys. Lett.** 111: 182410.
- Chiu, F. C., Shih, W. C., and Feng, J. J. (2012). Conduction mechanism of resistive switching films in MgO memory devices. **J. Appl. Phys.** 111: 094104.
- Davarnejad, R., and Jamshidzadeh, M. (2015). CFD modeling of heat transfer performance of MgO-water nanofluid under turbulent flow. **Eng. Sci. Technol. Int J.** 18: 536-542.

- Dobrzanski, L. Bamberger, A. M., and Totten, G. E. (2020). **Magnesium and Its Alloys: Technology and Applications**. Florida: CRC Press Taylor & Francis Group.
- Farmer, J. A., Campbell, C. T., Xu, L., and Henkelman, G. (2009). Defect sites and their distributions on MgO(100) by Li and Ca adsorption calorimetry. **J. Am. Chem. Soc.** 131: 3093-3103.
- Feng, J. F., Diao, Z., Feng, G., Nowak, E. R., and Coey, J. M. D. (2010). Magnetic noise in MgO-based magnetic tunnel junction rings. **Appl. Phys. Lett.** 96: 052504.
- Gay, Ian D., and Harrison, N. M. (2005). A density functional study of water and methanol chemisorption on MgO(110). **Surf. Sci.** 591: 13-22.
- Hacquart, R., and Jupille, J. (2007). Hydrated MgO smoke crystals from cubes to octahedra. **Chem. Phys. Lett.** 439: 91-94.
- Hadorn, J. P., Sukegawa, H. I., Ohkubo, T., Mitani, S., and Hono, K. (2018). Microstructural evolution of perpendicular magnetization films with an ultra-thin Co₂FeAl/MgAl₂O₄(001) structure. **Acta Mater.** 145: 306-315.
- Hanlon, J. M., Diaz, L. B., Balducci, G., Stobbs, B. A., Bielewski, M., and Chung, P. (2015). Rapid surfactant-free synthesis of Mg(OH)₂ nanoplates and pseudomorphic dehydration to MgO. **Cryst. Eng. Comm.** 17: 5672-5679.
- Hicks, A. S. and Larese, J. Z. (2013). Inelastic neutron scattering (INS) observations of rotational tunneling within partially deuterated methane monolayers adsorbed on Mg(100) surfaces. **Chem. Phys.** 427: 71-81.
- Ikeda, S., Hayakawa, J., Ashizawa, Y., Lee, Y. M., Miura, K., and Hasegawa, H. (2008). Tunnel magnetoresistance of 604% at 300K by suppression of Ta diffusion in CoFeB/MgO/CoFeB pseudo-spin-valves annealed at high temperature. **Appl. Phys. Lett.** 93: 082508.

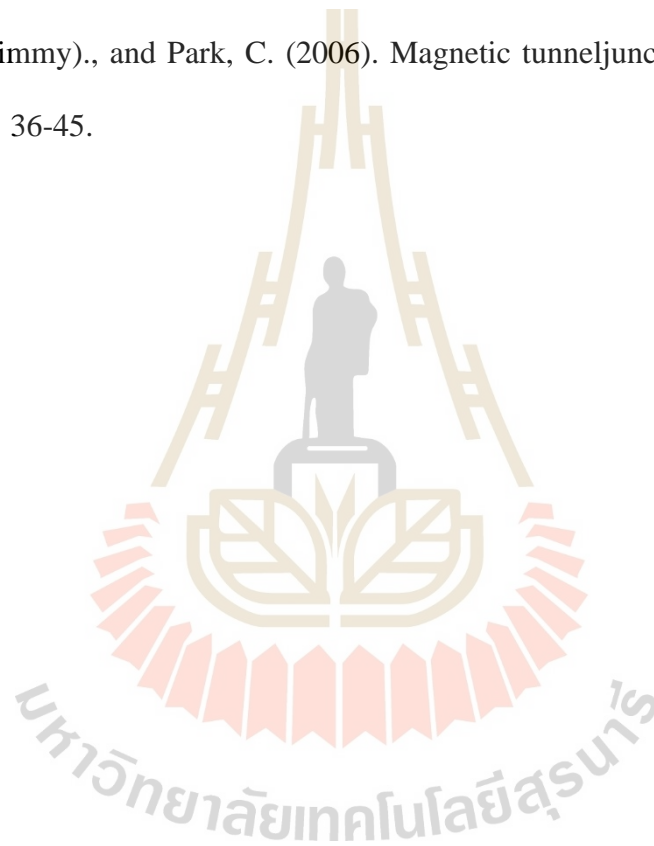
- Isogami, S., Tsunoda, M., Komagaki, K., Sunaga, K., Uehara, Y., and Sato, M. (2008). *In situ* heat treatment of ultrathin MgO layer for giant magnetoresistance ratio with low resistance area product in CoFeB/MgO/CoFeB magnetic tunnel junctions. **Appl. Phys. Lett.** 93: 192109.
- Johnson, M. A., Stefanovich, E. V., Truong, T. N., Gunster, J., and Goodman, D. W. (1999). Dissociation of water at the MgO(100)-water interfaces: Comparison of theory with experiment. **J. Phys. Chem. B.** 103: 3391-3398.
- Konig, T., Simon, G. H., Rust, H. P., Pacchioni, G., Heyde, M., and Freund, H. J. (2009). Measuring the Charge State of Point Defects on MgO/Ag(001). **J. Am. Chem. Soc.** 131: 17544-17545.
- Kuenzel, C., Zhang, F., Ferrandiz-Mas, V., Cheeseman, C. R., and Gartner, E. M. (2018). The mechanism of hydration of MgO-hydromagnesite blends. **Cem. Concr. Res.** 103: 123-129.
- Kurt, H., Oguz, K., Niizeki, T., and Coey, J. M. D. (2010). Giant tunneling magnetoresistance with electron beam evaporated MgO barrier and CoFeB electrodes. **J. Appl. Phys.** 107: 083920.
- Lei, T., Ouyang, C., Tang, W., Li, L. F., and Zhou, L. S. (2010). Preparation of MgO coatings on magnesium alloys for corrosion protection. **Surf. Coat. Tech.** 204: 3798-3803.
- Lee, I. H., Lee, T. Y., Hwang, S. M., and Chung, C. W. (2014). Etch characteristics of MgO thin films in Cl₂/Ar, CH₃OH/Ar and CH₄/Ar plasmas. **Vacuum.** 101: 394-398.
- Lee, J. H., Eun, J. H., Kim, S. G., Park, S. Y., Lee, M. J., and Kim, H. J. (2003a). Hydration behavior of MgO single crystals and thin films. **J. Mater. Res.** 18: 2895-2903.

- Lee, J. H., Eun, J. H., Park, S. Y., Kim, S. G., and Kim, H. J. (2003b). Hydration of R.F. magnetron sputtered MgO thin films for a protective layer in AC plasma display panel. **Thin Solid Films**. 435: 95-101.
- Liu, P., Kendelewicz, T., Brown, Jr., G. E., Parks, G. A. (1988). Reaction of water with MgO(100) surfaces. Part I: Synchrotron X-ray photoemission studies of low-defect surfaces. **Surf. Sci.** 412/413: 287-314.
- Maltseva, A., Shkirshiy, V., Lefevre, G., and Volovitch, P. (2019). Effect of pH on Mg(OH)₂ film evolution on corroding Mg by in situ kinetic Raman mapping (KRM). **Corr. Sci.** 153: 272-282.
- Matsumoto, R., Nishioka, S., Mizuguchi, M., Shiraishia, M., Maehara, H. and Tsunekawa, K. (2007). Dependence on annealing temperatures of tunneling spectra in high-resistance CoFeB/MgO/CoFeB magnetic tunnel junctions. **Solid. State. Commun.** 143: 574-578.
- Moon, S. H., Heo, T. W., Park, S. Y., Kim, J. H., and Kim, H. J. (2007). The Effect of the Dehydration of MgO Films on their XPS Spectra and Electrical Properties. **J. Electrochem. Soc.** 154(12): J408-J412.
- Oncak, M., Wlodarczyk, R., and Sauer, J. (2015). Water on the MgO(001) surface: Surface reconstruction and ion solvation. **J. Phys. Chem. Lett.** 6: 2310-2314.
- Parkin, S. S. P., Kaiser, C., Panchula, A., Rice, P. M., Hughes, B., and Samant, M. (2004). Giant tunnelling magnetoresistance at room temperature with MgO (100) tunnel barriers. **Nat. Mater.** 3: 862-867.
- Rocha, S. D. F., Mansur, M. B., and Ciminelli, V. S. T. (2004). Kinetics and mechanistic analysis of caustic magnesia hydration. **J. Chem. Technol. Biotechnol.** 79: 816-821.

- Sangwal, K., Sanz, F., and Gorostiza, P. (1999). Study of the surface morphology of the (100) cleavage planes of MgO single crystals by atomic force microscopy. **Surf. Sci.** 424: 139-144.
- Schreiber, D. K., Choi, Y. S., Liu, Y., Chiamonti, A. N., Seidman, D. N., and Petford-Long, A. K. (2011). Enhanced magnetoresistance in naturally oxidized MgO-based magnetic tunnel junctions with ferromagnetic CoFe/CoFeB bilayers. **Appl. Phys. Lett.** 98: 232506.
- Silva, L. F. M. da, and Sato, C. (2013). Design of adhesive joints under humid conditions. **Advance Structure Materials** 25. Berlin: Springer.
- Singh, B. B., Agrawal, V., Joshi, A. G., and Chaudhary, S. (2012). X-ray photoelectron spectroscopy and conducting atomic force microscopy investigations on dual ion beam sputtered MgO ultrathin films. **Thin Solid Films.** 520: 6734-6739.
- Smirnov, E., Sedoykina, T., Orlov, A., Portemont, C., Ducruet, C., and Alvarez-Hérault, vJ. (2017). Evaluation of a new MgO barrier based on CoFeB/MgO/CoFeB structure for advanced MRAM applications. **Microelectron Eng.** 167: 6-9.
- Song, W., Yang, L., Ma, X., and Liang, G. (2018). Effects of CaO and MgO on anticorrosive performance of aluminum dihydrogen triphosphate on mild steel. **Ind. Eng. Chem. Res.** 57: 13578-13585.
- Stanish, M. A., and Perlmutter, D. D. (1983). Kinetics and transport effects in the dehydration of crystalline potassium carbonate hydrate. **AIChE Journal.** 29(5): 806-812.

- Stearrett, R., Wang, W. G., Kou, X., Feng, J. F., Coey, J. M. D., and Xiao, J. Q. (2012). Influence of exchange bias on magnetic losses in CoFeB/MgO/CoFeB tunnel junctions. **Phys. Rev. B.** 86: 014415.
- Stefanovich, E. V., and Truong, T. N. (1997). A theoretical approach for modeling reactivity at solid-liquid interfaces. **J. Chem. Phys.** 106: 7700-7705.
- Sung, M. M., Kim, C., Kim, C. G., and Kim, Y. (2000). Epitaxial growth of MgO films on Si(111) by metal organic chemical vapor deposition. **J. Cryst. Growth.** 210: 651-654.
- Tigunta, S., Khlikhum, P., Kidkhunthod, P., Chanlek, N., Supadee, L. and Pojprapai, S. (2019). Dissolution behavior of MgO thin film-barrier magnetic tunneling junctions. **J. Mater. Sci.: Mater. Electron.** 30: 6718-6724.
- Todnem, K., Borve, K. J., and Nygren, M. (1999). Molecular adsorption of methane and methyl onto MgO(100) an embedded-cluster study. **Surf. Sci.** 421: 296-307.
- Wang, W. B., Yang, Y., Yanguas-Gil, A., Chang, N. N., Girolami, G. S., and Abelson, J. R. (2013). Highly conformal magnesium oxide thin films by low-temperature chemical vapor deposition from $\text{Mg}(\text{H}_3\text{BNMe}_2\text{BH}_3)_2$ and water. **Appl. Phys. Lett.** 102: 101605.
- Wisniowski, P., Dabek, M., Cardoso, S., and Freitas, P. P. (2013). Magnetic field sensing characteristics of MgO based tunneling magnetoresistance devices with $\text{Co}_{40}\text{Fe}_{40}\text{B}_{20}$ and $\text{Co}_{60}\text{Fe}_{20}\text{B}_{20}$ electrodes. **Sens. Actuators. A.** 202: 64-68.
- Yang, H., Yang, S. H., and Parkin, S. (2012). The role of Mg interface layer in MgO magnetic tunnel junctions with CoFe and CoFeB electrodes. **AIP Adv.** 2: 012150.

- Yuasa, S., and Djayaprawira, D. D. (2007). Giant tunnel magnetoresistance in magnetic tunnel junctions with a crystalline MgO(001) barrier. **J. Phys. D: Appl. Phys.** 40: R337-R354.
- Yuasa, S., Nagahama, T., Fukushima, A., Suzuki, Y., and Ando, K. (2004). Giant room-temperature magnetoresistance in single-crystal Fe/MgO/Fe magnetic tunnel junctions. **Nat. Mater.** 3: 868-871.
- Zhu, J.-G. (Jimmy)., and Park, C. (2006). Magnetic tunnel junctions. **Mater. Today.** 9(11): 36-45.



CHAPTER II

THEORETICAL BACKGROUND AND LITERATURE

REVIEW

This chapter introduces the background information of magnesium oxide (MgO) and magnetic tunneling junctions (MTJs) along with the thin film characterization techniques. In section 2.1 the basic information of MgO including properties, applications and the interaction with water are provided. The fundamental information of the magnetic tunneling junctions (MTJs) is described in section 2.2. In addition, basic principle of the characterization techniques used in this thesis including X-ray photoelectron spectroscopy (XPS), X-ray absorption spectroscopy (XAS), X-ray reflectivity (XRR) and transmission electron microscope (TEM) are also included in section 2.4.

2.1 Magnesium Oxide (MgO)

Magnesium oxide (MgO), also called periclase and/or magnesia, is a simple ionic mineral that is one of the most abundant minerals in the earth particularly in the lower mantle (Cohen, 2000; Oganov, 2003; Shand, 2006). MgO was discovered in 1840 by Scacchi at Monte Somma, Italy (Shand, 2006). MgO has been a subject of various experimental and theoretical studies because it possesses numerous remarkable physical, electrical, mechanical and chemical properties as shown below.

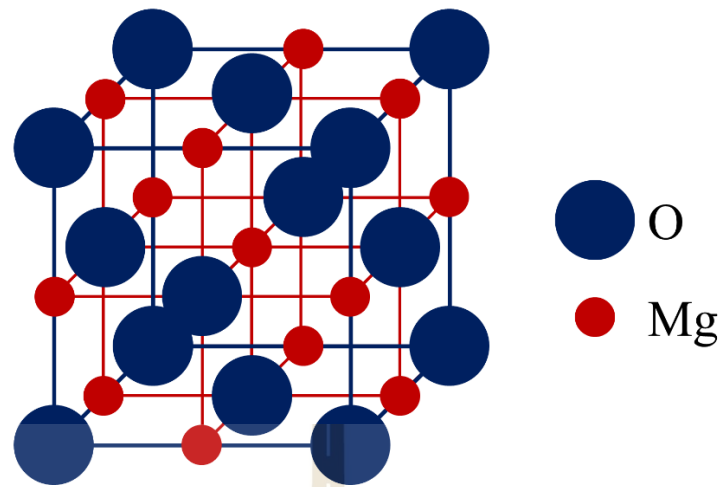


Figure 2.1 Magnesium oxide crystal structure

2.1.1 Properties of Magnesium Oxide

MgO is formed by a magnesium (Mg) atom and an oxygen (O) atom connected through an ionic bond with a single valence state (Jeevanandam, 2017; Licona, 2005). It crystallizes in a face-centered cubic (FCC) unit cell with a rock-salt (NaCl) structure, as shown in Figure 2.1, each O^{2-} anion encircled by six Mg^{2+} cations and each Mg^{2+} cation encircled by six O^{2-} anions (Licona, 2005; Shand, 2006). MgO has a lattice parameter of 4.2112 Å and energy bandgap (E_g) of 7.3 eV (Bullard, 2001; Dyachenko, 2014). The range of its density is 3.55 to 3.68 g/cm³ (i.e. depending on its form, Thin film = 3.58 g/cm³, Bulk = 3.62 g/cm³). The hardness is 5.5 on the Mohs scale. MgO normally is a colorless to grayish-white color, however, its color can be varied depending on its foreign inclusions. MgO is a transparent material with a refractive index of ~1.736 so that it is usually applied as an optical material in numerous applications. (Bullard, 2001; Kruk, 2018; Shand, 2006). It is reported that the electronegativity of MgO is 2.13. The melting point is ~2800°C and boiling point is ~3600°C (Bullard, 2001). MgO is an outstanding high-temperature electrical insulator.

It is reported that the specific resistance of pure MgO crystals at 700°C is 2.3×10^9 Ω -cm. The dielectric constant of MgO at 25°C and 1 MHz is 3.2-9.8, while its dielectric loss ($\tan \delta$) is 3×10^{-4} at 1 MHz. Moreover, it is found that MgO also have a high breakdown field of 12 Mv/cm (Habibah, 2013). To make it easy to understand the physical properties of MgO are summarized and exhibited in Table 2.1.

Table 2.1 The properties of MgO

Properties	Values
Crystal type	Cubic FCC
Lattice constant (Å)	4.212
Energy band gap (eV)	7.3
Molecule weight (40.304
Density	
- Thin film (g/cm ³)	3.585
- Bulk (g/cm ³)	3.62
Hardness (Mohs scale)	5.5
Reflective index	1.736
Melting point (°C)	2800
Boiling point (°C)	3600
Oxidation state	Mg: +2 O: -2
Ionic radius (nm)	Mg ²⁺ = 0.072 O ²⁻ = 0.140

2.1.2 Application of Magnesium Oxide Thin Film

Recently, MgO thin film was employed as a tunnel barrier in magnetic tunneling junctions (MTJs) which is an essential part of magnetic sensor, magnetic random-access memory (MRAM) (Chou, 2006; Feng, 2010; Feng, 2011; Wisniowski,

2013) and read head sensors of hard disk drives (HDDs) (see Figure 2.2) (Diao, 2010; Feng, 2009).

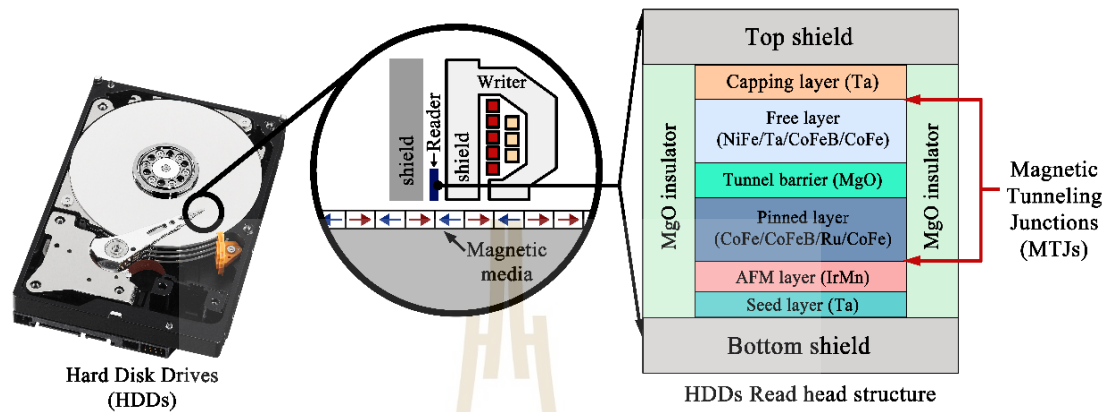


Figure 2.2 MgO thin film in the read head structure of HDDs.

MgO thin film is extensively used as the tunnel barrier in MTJs because the properties of MgO thin film including epitaxial structure, low electrical conductivity and high thermal stability are effective in enhancing the tunnel magnetoresistance (TMR) value of MTJs which is correlating with the sensitivity of the read head sensor (Bhutta, 2009; Yuasa, 2007). It is reported that using the MgO thin film as a tunnel barrier in MTJs, the largest TMR value that has been recorded is obtained (Diao, 2010; Feng, 2009; Stearrett, 2012). This will be explained in the section 2.2 magnetic tunneling junctions (MTJs).

2.1.3 The Interaction Between the MgO and Water

Although the MgO possesses several remarkable properties, as described above, the susceptible to water is still a major problem of it. Several studies reported that in a presence of water (including liquid or vapor form) the MgO can hydrate by physically and chemically absorbing water molecules to form the hydroxide $\text{Mg}(\text{OH})_2$ layer.

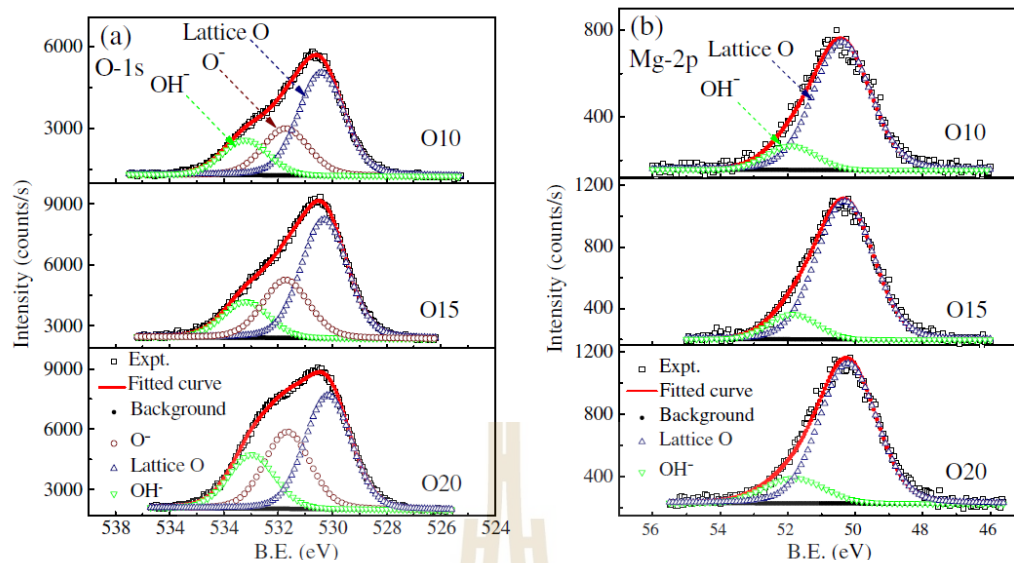


Figure 2.3 Deconvoluted core-level XPS spectra of (a) O $1s$ and (b) Mg $2p$ of the MgO thin films deposited in the different oxygen partial pressures (Singh, 2012).

Singh *et al.* (2012) found that the MgO thin film can react with the residual water vapor in the chamber during the growing of thin film and forms the Mg(OH)₂. This is confirmed by the observation of –OH peak in the deconvoluted O1s spectra of the X-ray photoelectron spectroscopy (XPS) as shown in Figure 2.3.

Lee *et al.* (2003) studied the hydration reaction of the MgO single crystal and MgO thin film. It was found that the MgO can absorb the water and create clusters over its surface (See Figure 2.4). The formation of these clusters is a result of the lattice mismatch between the lattice parameter of the cubic MgO ($a = b = c = 0.4213$ nm) and the hexagonal Mg(OH)₂ ($a = b = 0.3142$ nm, $c = 0.4766$ nm). In a comparison between the hydration of the single crystal MgO and MgO thin film, they exposed that the MgO thin film is much more hydrated than the single crystal MgO.

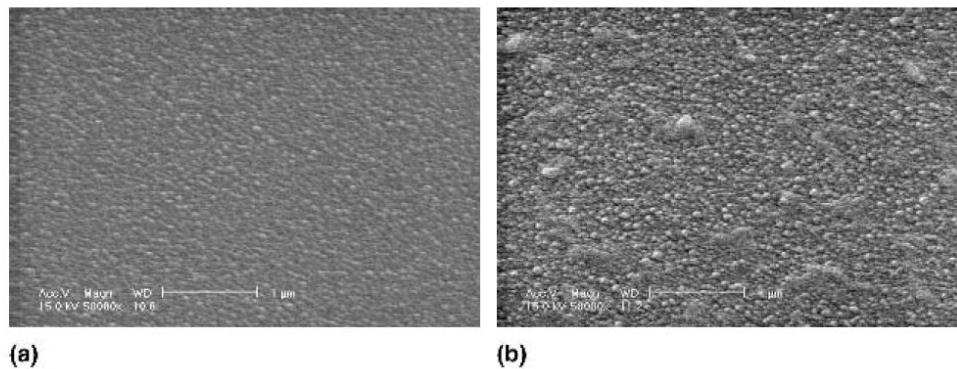


Figure 2.4 SEM photographs of the MgO thin film sample hydrated for 0 day and 1 day (Lee, 2003).

Besides the formation of clusters, many studies reported that the formation of $\text{Mg}(\text{OH})_2$ could induce the volume expansion lead to swelling, cracking and porosity/vacancies in the MgO (Ali and Al-Mowali 2013; Amaral, 2011, Dobrzanski, 2020; Lee, 2003). Nagamine *et al.* (2006) observed the deformation in the crystalline orientation of MgO thin film barrier after it absorbs water and forms $\text{Mg}(\text{OH})_2$ layer. In addition, there are studies reported that the absorption of the water molecules does not occur only over the MgO surface, but it can also infiltrate into the inner layer of the MgO (Lee, 2003; Smithson and Bakhshi, 1969). This may result in the degradation of the MgO devices. Besides the hydration reaction, several works point out that if there are significant amounts of water vapor presented and/or MgO is in contact with water, the hydrated MgO can dissolve in water by releasing Mg^{2+} and OH^- ions into water (Amaral, 2010; Amaral, 2011; Hanlon, 2015; Kuenzel, 2018; Rocha, 2004). Subsequently, it could lead to an increase in the number of vacancies in MgO (Bureto, 1993) and a decrease of MgO thin film thickness.

2.1.4 The Dehydration Reaction of MgO

It is known that the dehydration reaction is the water elimination mechanism from the molecule of materials which most often involves the thermal decomposition (Stanish and Perlmutter, 1983). Many studies reported that the dehydration reaction could reduce the hydroxide layer and induce the recovery of the properties of MgO (Gay and Harrison, 2005; Moon 2007).

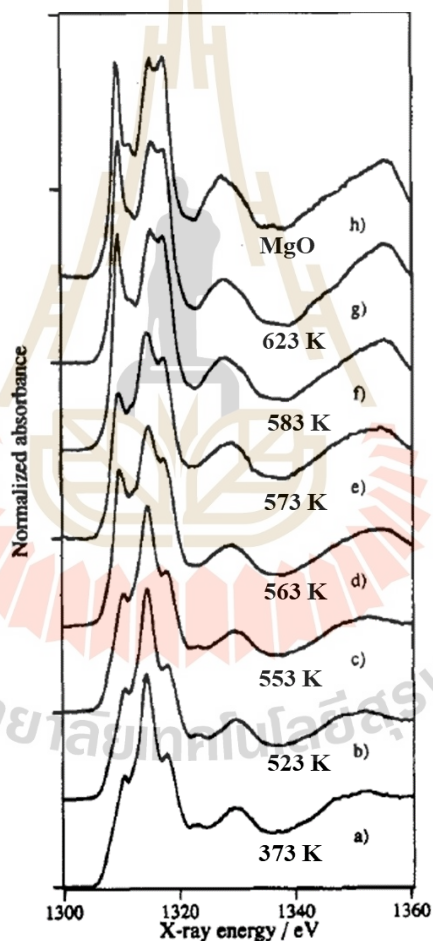


Figure 2.5 Mg K-edge XANES of Mg(OH)₂ evaluated for 5 hours at various temperatures and Mg K-edge of MgO (Yoshida, 1995).

Yoshida *et al.*(1995) investigated the dehydration of the magnesium hydroxide powder. The $\text{Mg}(\text{OH})_2$ powders were evacuated at various temperatures 373-673 K (or 99.85-399.85°C) under pressure of 1.5×10^{-3} Torr for 5 hours. Using X-ray absorption near-edge structure (XANES), they found that the Mg K-edge XANES spectra of MgO can change from $\text{Mg}(\text{OH})_2$ to MgO after the increase of the evacuated temperature. It is found that sample dehydrating at 623 K exhibited the similar XANES spectra to that of MgO, as seen in Figure 2.5.

Khamkongkao *et al.* (2017) also investigated the dehydration reaction of the $\text{Mg}(\text{OH})_2$ powder. After calcination at 450°C for 5 hours in air, $\text{Mg}(\text{OH})_2$ does not completely convert to MgO, but it consists of 45.5% of $\text{Mg}(\text{OH})_2$ and 54.4% of MgO contents. They further suggested that this unsuitable calcination condition could lead to the formation of Mg vacancies and O vacancies in MgO and/or $\text{Mg}(\text{OH})_2$ structure resulting in the inhibition of the improvement of the specific magnetization of MgO.

2.2 Magnetic Tunneling Junctions (MTJs)

Magnetic Tunneling Junctions (MTJs) are the structure that makes from a multilayer of a thin film, the thickness of each layer is only a few nanometers. The basic structure of MTJs consists of two ferromagnetic (FM) electrodes separated by a very thin insulating oxide layer (also called a tunnel barrier) as shown in Figure 2.6 (Harnchana, 2011, Yuasa and Djayaprawira, 2007). One of the ferromagnetic (FM) electrodes is denoted as a pinned layer because the magnetization direction of this layer is pinned to a particular direction while the magnetization direction of another ferromagnetic layer denoted as the free layer can be altered by the external magnetic field (Harnchana, 2011, Sengupta, 2017; Yuasa and Djayaprawira, 2007).

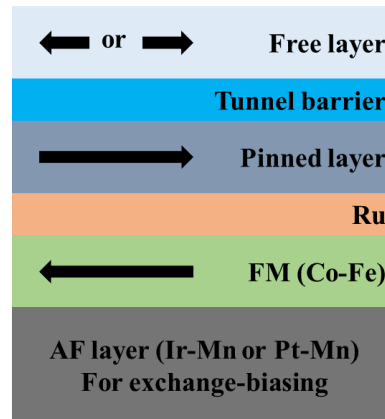


Figure 2.6 A schematic of a cross-sectional structure of MTJs (Yuasa and Djayaprawira, 2007).

The magnetization direction of these two ferromagnetic electrodes are related to a level of the MTJs resistance. In case of low resistance in a parallel orientation (R_P), the magnetization of the two ferromagnetic layers are in the same orientation. On the other hand, in case of high resistance in the anti-parallel orientation (R_{AP}), the magnetization direction of the two ferromagnetic layers are in the opposite direction (Maciel, 2020; Sengupta, 2017). By applying the current through the MTJs from the pinned layer to the free layer and vice versa, the MTJs state is changed from the parallel to the antiparallel state (see Figure 2.7).

The change in the resistance with the relative orientation of two ferromagnetic electrodes is generally described in the term tunneling magnetoresistance (TMR) ratio or magnetoresistance (MR) ratio for short, which is defined as (Harnchana, 2011; Sengupta, 2017; Yuasa and Djayaprawira, 2007):

$$TMR = \frac{R_{AP} - R_P}{R_P} \quad (2.1)$$

If there is a large change between the resistance of the two configurations, the TMR ratio will be large.

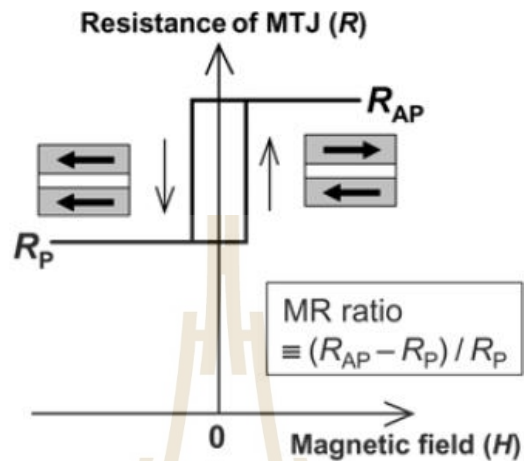


Figure 2.7 The magnetoresistance curve of a MTJs (Yuasa and Djayaprawira, 2007).

2.2.1 Tunnel Barrier of MTJs

Besides ferromagnetic layers, the tunnel barrier is one of the factors that play an important role in the TMR value. In the previous MTJ technology, the barrier is made of the Al-O barrier and the TMR value is limited to about 70% because Al-O tunnel barrier is amorphous. The tunneling probabilities of the electrons through the Al-O is limited as exhibited in Figure 2.8. Recently, when the MgO(001) is used as a tunnel barrier instead of Al-O barrier, it is found that TMR value of MTJs can enhance to be 600% at room temperature. This is the highest TMR value that has been obtained. The enhance of the TMR value could be a result of the epitaxial structure of the MgO(001) barrier.

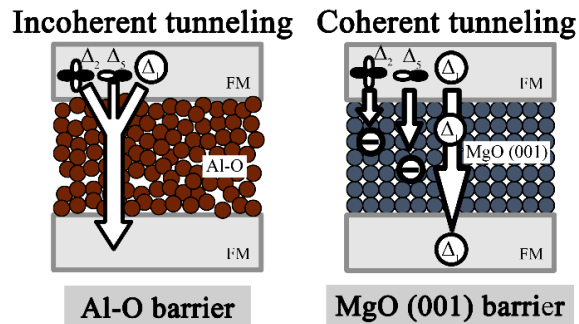


Figure 2.8 Schematic illustration of electron tunneling through an amorphous Al-O barrier and a crystalline MgO barrier.

2.3 Thin Film Characterization

2.3.1 X-Ray Photoelectron Spectroscopy (XPS)

X-ray photoelectron spectroscopy (XPS), otherwise known as electron spectroscopy for chemical analysis (ESCA), is surface analysis technique giving information of the surface chemistry, chemical state and chemical composition of the uppermost atomic layers (1-10 nm) (Heide, 2012; Leinen, 1999). In combination with low energy ion bombardment, used for depth profiling, this technique can be used for a compositional and chemical analysis in depth.

2.3.1.1 The Basic Principle of XPS

X-ray photoelectrons are produced by the ejection of core electrons, which are bombarded by incident X-ray photons, from 1-10 nm underneath the surface of sample (See Figure 2.9). The kinetic energies of the emitted photoelectron are then measured to determine their binding energies and consequently, the chemical state information can be obtained. The photoelectron energy relationship is given by (Watts and Wolstenholme, 2003):

$$E_B = h\nu - E_K - W_F \quad (2.2)$$

where E_B is the energy by which the photoelectron bonds with parent atom, $h\nu$ is the energy of the incident photon, E_K is kinetic energy of the photoelectron and W_F is the spectrometer work function.

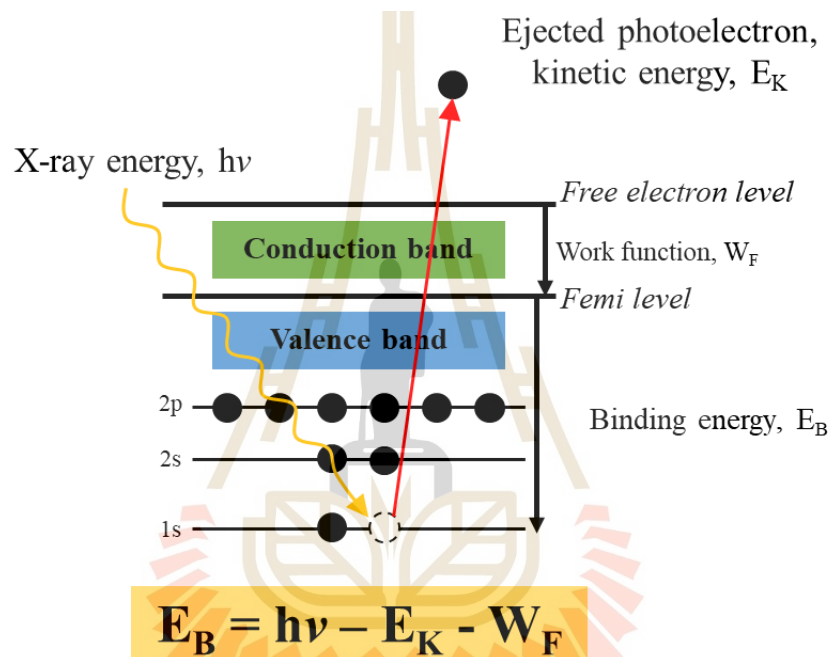


Figure 2.9 Schematic diagram of the XPS process.

As a result of each electron has specific binding energy in the specific atom. Therefore, the kinetic energy of the electrons kicked out is able to indicate the atoms contained in the material (Heide, 2012; Leinen, 1999). The number of emitted photoelectrons is plotted as a function of binding energy as illustrated in Figure 2.10.

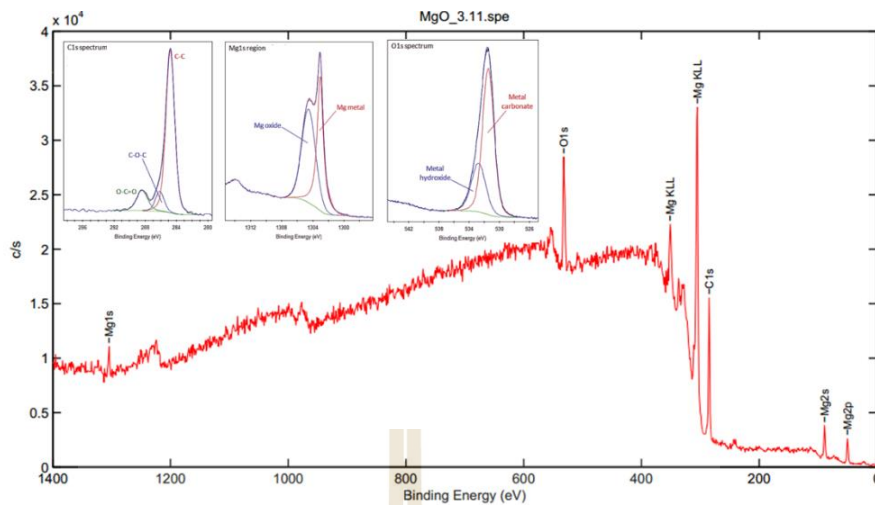


Figure 2.10 The survey scan and narrow scan of XPS spectra.

2.3.2 X-Ray Absorption Spectroscopy (XAS)

X-ray absorption spectroscopy (XAS) is a characterization technique that widely used for determining the local geometric and electronic structure of material. The XAS spectra compose of two regions: (1) X-ray absorption near edge structure (XANES) with the energy ranged from 0 to 50 eV and (2) extended X-ray absorption fine structure (EXAFS) with the energy ranged from 50 eV to 1000 eV (Harnchana, 2011, Tian, 2014). The X-ray absorption spectrum is shown in Figure 2.11.

2.3.2.1 The Basic Principle of XAS

X-ray absorption spectroscopy (XAS) can be operated by using a synchrotron radiation as X-ray source. The photons from the X-ray interact with the core electron. If absorbed energy is equal to the binding energy of an electron, the electron will be excited to an unoccupied state and leave a core hole behind. The atom is in excited state and not stable, thus an electron in a higher energy level then releases a photon in order to fill itself to the core hole. Therefore, the X-ray absorption

corresponds to the binding energy of the core electron that transitions into an unoccupied state and reflects the electronic unoccupied state of the specimen. The absorption edge name is from the principle quantum number of the excited core electron for example, K, L and M edges correspond to the excited $1s$, $2s$ or $2p$ and $3s$ or $3p$ or $3d$, respectively.

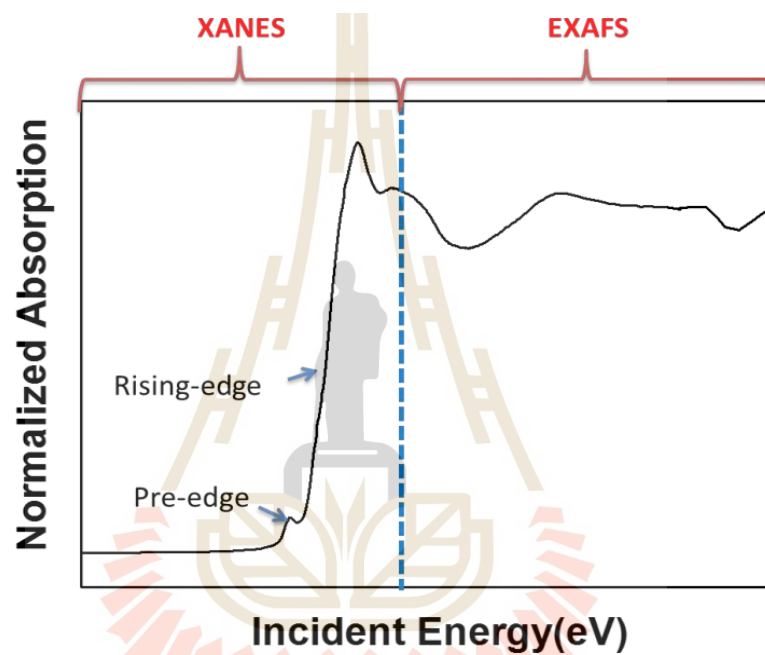


Figure 2.11 The X-ray absorption spectrum (Tian, 2014).

2.3.3 X-Ray Reflectivity (XRR)

The XRR is a non-destructive analysis technique that has been extensively used for investigating of thickness, density and roughness of the surface and the interface of a single layer or multiple-layer thin films which have a thickness between approximately 1 nm to $1\mu\text{m}$ (Bowen, 2006; Fujii, 2013; Gibaud, 2000; Gibaud, 2013; Matyi, 2008; Yasaka, 2010). XRR can be performed by using the same

diffractometer as X-ray diffraction (XRD), however, principle is different. A schematic of X-ray reflectivity measurement set up is illustrates in Figure 2.12.

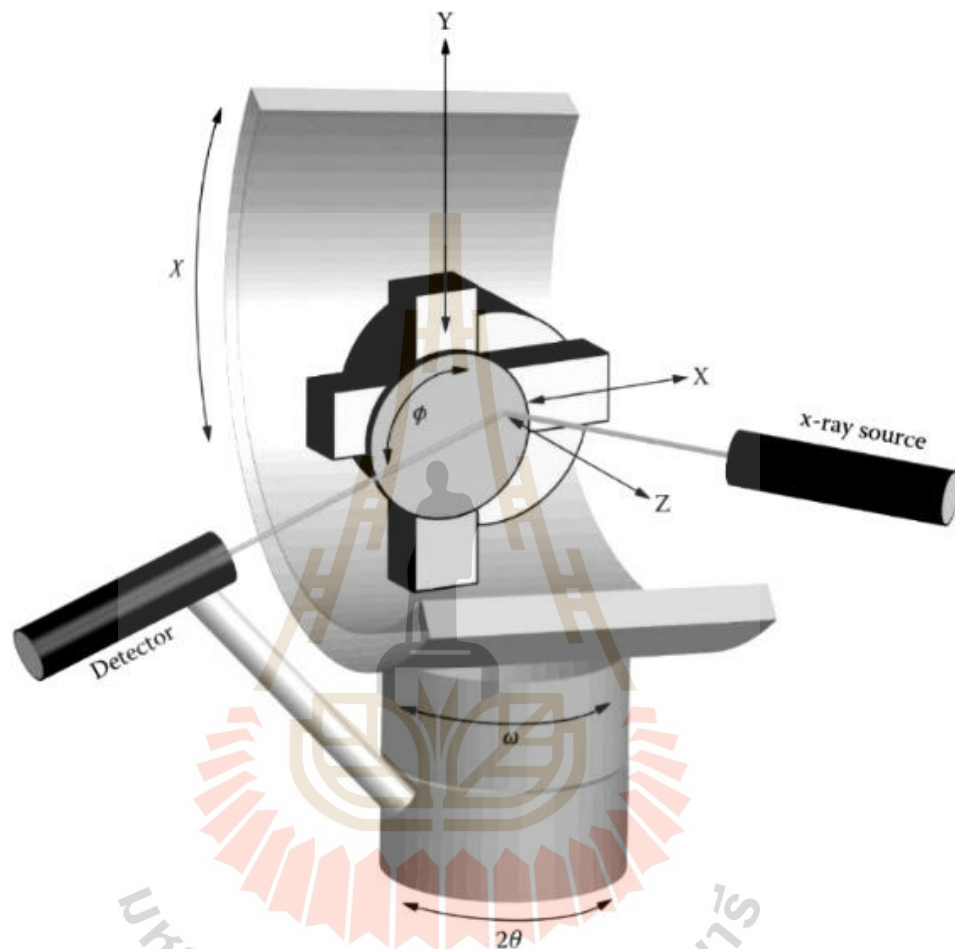


Figure 2.12 A schematic of X-ray reflectivity measurement set up (Bowen, 2006).

2.3.3.1 The Basic Principle of XRR

XRR is the measurement of the X-ray intensity which scattered or reflected from the sample surface or interface in the specular direction (reflected angle (α_f) equal to incident angle (α_i)) as a function of scattering angles (see Figure 2.13).

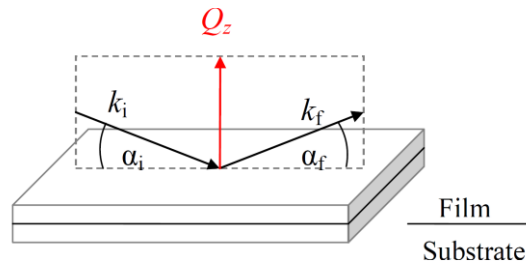


Figure 2.13 Schematic diagram showing the specular reflectivity geometry (Harnchana, 2011).

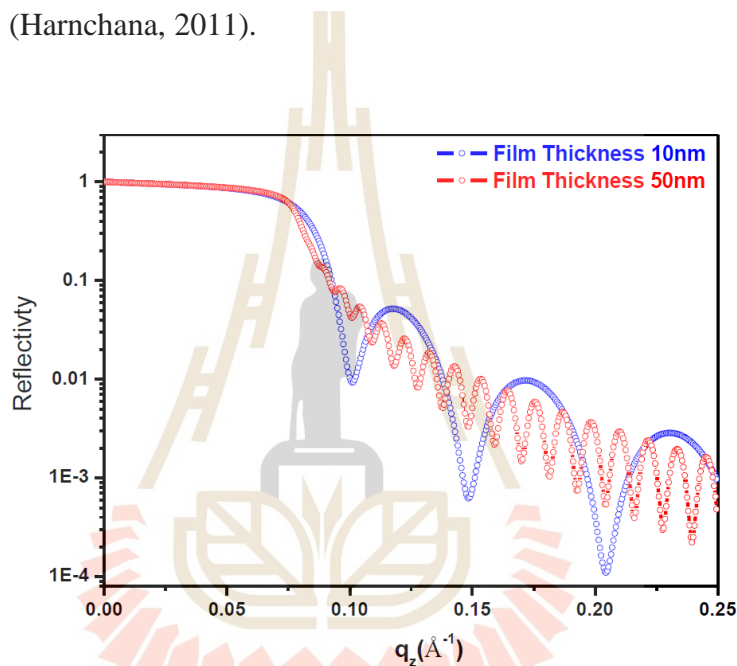


Figure 2.14 Reflectivity of the thin film thickness 10 nm and 50 nm (Potdar, 2014; Yasaka, 2010).

When the incident X-rays bombard on a flat surface (reflective index less than 1) at the low incident angle of 1-2°, the total reflected X-rays occur, if the incident angle is smaller than a certain critical angle. In this region, the X-rays do not penetrate into the sample surface or penetrate in a few nanometers. When the incident angle is increased to higher than 1-2°, the X-rays start to penetrate and reflect from the interfaces. The reflected X-rays from the different interfaces give rise to

interference fringes as shown in Figure 2.14. This XRR spectra can be utilized to estimate the thickness, density and roughness of the film surface and interface (Lin, 2016; Potdar, 2014; Yasaka, 2010).

2.3.4 Transmission Electron Microscopy (TEM)

Transmission electron microscopy (TEM) was used in this thesis as a complementary technique to XRR to provide the primary information of the change in thickness and the structural evolution of the MgO thin film. TEM is well-established as a very high-resolution imaging/characterization technique that uses to analyzed almost type of materials. TEM is useful in providing the information of structural, chemical and crystallographic at the atomic level (Dayal, 2011; Reimer, 1989).

2.3.4.1 The Basic Principle of TEM

TEM operation involves two essential main components: (1) an electron source and (2) set of electromagnetic lenses (see Figure 2.15). The electro source generated electron beam is focused by condenser lenses to produce a parallel beam at the specimen for TEM and convergent beam for scanning transmission electron microscope (STEM). The image is then formed post specimen by an objective lens in TEM and by serial acquisition of the transmitted beam (scanning the beam) in STEM (Hubschen, 2016). The sample suitable for the TEM analysis is the sample with thickness less than 100 nm. The TEM sample preparation will be explained again in Chapter 5.

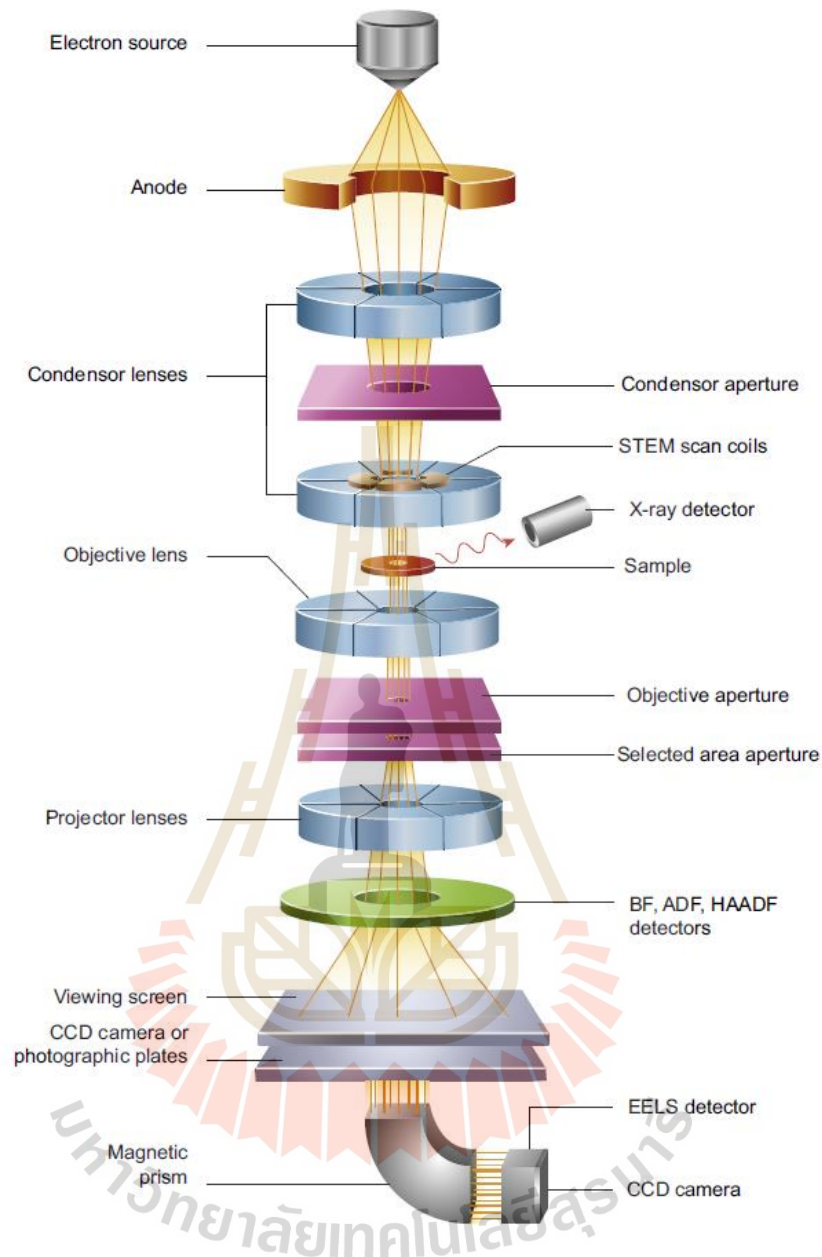


Figure 2.15 Schematic of core component of a TEM microscope (Hubschen, 2016)

2.3.5 A Comparison of Usefulness and Limitation of Each Characterization Technique

For the better understanding of the features of each technique, in this section, the advantages and limitations of these techniques are summarized in Table 2.2.

Table 2.2 Comparison of advantage and limitation of characterization techniques for analysis the MgO thin film.

Technique	Output	Advantages	Limitations
XPS	Chemical composition. Chemical bonding. Depth profiling. Sputtering yield Thickness	Surface sensitive technique. Suitable for thin film.	Peak overlap for some elements. Cannot detect hydrogen. Take long time data interpretation (in case of depth profiling).
XAS	Chemical state Electronic structure	Non-destructive technique. Local structure technique. Can be carried out on any type of material. High resolution (angstrom) .	Can use only synchrotron source. Require high expertise for data analysis.
XRR	Thickness Roughness Density	Non-destructive technique. Can determine the multilayer thin film. Can be performed in total time ranges as short as 10 s.	Requires relatively large sample areas. Require model for fitting.
TEM	Thickness Crystallographic structure Interface Chemical composition	High resolution technique. Can determine the multilayer thin film	Cannot analyzed thick sample (>100um). Require extensive sample preparation. High cost Destructive technique. Time-consuming process. Require expertise for TEM operation.

2.4 References

Ali, A. M., and Al-Mowali, A. H.(2013). Ceramic expansion by water layers on magnesium oxide: AB InitioStudy. **Am. J. Mater. Sci.** 1: 50-53.

- Amaral, L. F., Oliveira, I. R., Salomao, R., Frollini, E., and Pandolfelli, V. C. (2010). Temperature and common ion effect on magnesium oxide (MgO) hydration. **Ceram. Int.** 36: 1047.
- Amaral, L. F., Oliveira, I. R., Bonadia, P., Salomao, R., and Pandolfelli, V. C. (2011). Chelants to inhibit magnesia (MgO) hydration. **Ceram. Int.** 37: 1537-1542.
- Aswal, D. K., Muthe, K. P., Tawda, S., Chodhury, S., Bagkar, N., and Singh, A. (2002). XPS and AFM investigations of annealing induced surface modifications of MgO single crystals. **J. Cryst. Growth.** 236: 661-666.
- Bhutta, K. M., Schmalhorst, J., and Reiss, G. (2009). Study of MgO tunnel barriers with conducting atomic force microscopy. **J. Magn. Magn. Mater.** 321: 3384-3390.
- Bowen, D. K., and Tanner, B. K. (2006). X-Ray Metrology in Semiconductor Manufacturing. London: Taylor and Francis.
- Beruto, D., Searcy, A. W., Botter, R., and Giordani, M. (1993). Thermodynamics and kinetics of H₂O(v) chemisorption and solubility in nanometric and single-crystal MgO particles during sintering. **J. Phys. Chem.** 97: 9201-9205.
- Chou, C. Y., Yao, Y. D., Kuo, P. C., Cheng, K. W., and Yu, C. (2006). Microstructure and morphology of MgO thin film with different magnetic underlayers. **J. Magn. Magn. Mater.** 304: e103-e105.
- Cohen, R. E. (2000). MgO-The Simplest Oxide. In Aoki, H., and Hemley, Y. S. R. J. (eds.). **Physics Meets Mineralogy.** (pp. 95-123). Cambridge: Cambridge University Press.
- Daillant J., and Gibaud, A. (2009). **X-ray and Neutron Reflectivity: Principles and Applications.** Berlin: Springer.

- Dayal, P. (2011). **Mechanical Behaviour of Nanolayered Aluminium/Palladium Thin Films**. Ph.D. Dissertation, The University of New South Wales.
- Diao, Z., Feng, J. F., Kurt, H., Feng, G., and Coey, J. M. D. (2010). Reduced low frequency noise in electron beam evaporated MgO magnetic tunnel junctions. **Appl. Phys. Lett.** 96: 202506.
- Dobrzanski, L. A., Bamberger, M., Totten, G. E. (2020). **Magnesium and Its Alloys: Technology and Applications**. Florida: CRC Press Taylor & Francis Group.
- Farmer, J. A., Campbell, C. T., Xu, L., and Henkelman, G. (2009). Defect sites and their distributions on MgO(100) by Li and Ca adsorption calorimetry. **J. Am. Chem. Soc.** 131: 3093-3103.
- Feng, G., Dijken, S. V., and Coey, J. M. D. (2009). MgO-based double barrier magnetic tunnel junctions with thin free layers. **J. Appl. Phys.** 105: 07C926.
- Feng, J. F., Diao, Z., Feng, G., Nowak, E. R., and Coey, J. M. D. (2010). Magnetic noise in MgO-based magnetic tunnel junction rings. **Appl. Phys. Lett.** 96: 052504.
- Feng, J. F., Diao, Z., and Coey, J. M. D. (2011). Annealing effect on low frequency noise in MgO-based magnetic tunnel junctions. **J. Phys. Conf. Ser.** 303: 012098.
- Fujii, Y. (2013). Estimation of Surface and Interface Roughness Using X-ray Reflectivity and TEM Observation. **Advance in Analytical Chemistry.** 3(2): 9-14.
- Gay, Ian D., and Harrison, N. M. (2005). A density functional study of water and methanol chemisorption on MgO(110). **Surf. Sci.** 591: 13-22.
- Gibaud, A., and Hazra, S. (2000). X-ray reflectivity and diffuse scattering. **Current Science.** 78(12): 1467-1477.

- Gibaud, A., Chebil, M. S., and Beuvier, T. (2013). Chapter 7 X-ray Reflectivity. In Bracco, G., and Holst, B. (eds.). **Surface Science Techniques, Springer Series in Surface Science 51**. Berlin: Springer.
- Habibah, Z., Yusof, K. A., Ismail, L. N., Baker, R. A., and Rusop, M. (2013). Sol-Gel Derived Nano-Magnesium Oxide: Influence of Drying Temperature to the Dielectric Layer Properties. **IOP Conf. Series: Materials Science and Engineering**. 46: 012006.
- Hanlon, J. M., Diaz, L. B., Balducci, G., Stobbs, B. A., Bielewski, M., and Chung, P. (2015). Rapid surfactant-free synthesis of Mg(OH)₂ nanoplates and pseudomorphic dehydration to MgO. **Cryst. Eng. Comm.** 17: 5672-5679.
- Harnchana, V. (2011). **Transmission Electron Microscopy Characterisation for development of CoFeB/MgO based Magnetic Tunnel Junctions**. Ph.D. Dissertation, The University of Leeds.
- Heide, P. V. D. (2012). **X-ray Photoelectron Spectroscopy: An introduction to principles and practices**. New Jersey: John Wiley & Sons.
- Hicks, A. S., and Larese, J. Z. (2013). Inelastic neutron scattering (INS) observations of rotational tunneling within partially deuterated methane monolayers adsorbed on Mg(100) surfaces. **Chem. Phys.** 427: 71-81.
- Hubschen, G., Altpeter, I., Tschuncky, R., and Herrmann, H.-G. (2016). **Materials Characterization Using Nondestructive Evaluation (NDE) Methods**. Berlin: Woodhead.
- Khamkongkao, A., Klysubun, W., Boonchuduang, T., Sailuam, W., Sriwattanac, P., and Phetrattanarangsia, T. (2018). X-ray Absorption Spectroscopy Investigation

- of Relationship Between Mg Vacancy and Magnetic Properties of MgO powder. **J. Magn. Mater.** 460: 327-333.
- Kruk, A. (2018). Fabrication of MgO high transparent ceramics by arc plasma synthesis. **Opt. Mater.** 84: 360-366.
- Kuenzel, C., Zhang, F., Ferrandiz-Mas, V., Cheeseman, C. R., and Gartner, E. M. (2018). The mechanism of hydration of MgO-hydromagnesite blends. **Cem. Concr. Res.** 103: 123-129.
- Lee, J. H., and Eun, J. H. (2003). Hydration behavior of MgO single crystals and thin films. **J. Mater. Res.** 18(12): 2895-2903.
- Leinen, D., Sirera, R., Rodriguez-Castellon, E., and Calzada, M. L. (1999). XPS depth profile analysis of sol-gel calcium-modified lead titanate thin films. **Thin Solid Films.** 354: 66-72.
- Lin, Q. (2016). **Development of high-performance lead-free piezoelectric thin films and nanostructures for microelectronic devices.** Ph.D. Dissertation, The University of New South Wales.
- Maciel, N., Marques, E., Naviner, L., Zhou, Y., and Cai, H. (2020). Magnetic Tunnel Junction Applications. **Sensors.** 20: 121.
- Matyi, R. J., Depero, L. E., Bontempi, E., Colombi, P., Gibaud, A., and Jergel, M. (2008). The international VAMAS project on X-ray reflectivity measurements for evaluation of thin films and multilayers – Preliminary results from the second round-robin. **Thin Solid Films.** 516: 7962-7966.
- Moon, S. H., Heo, T. W., Park, S. Y., Kim, J. H., and Kim, H. J. (2007). The Effect of the Dehydration of MgO Films on their XPS Spectra and Electrical Properties. **J. Electrochem. Soc.** 154(12): J408-J412.

- Nagamine, Y., H. Maehara, K. Tsunekawa, D. D. Djayaprawira, N. Watanabe, Ultralow resistance-area product of $0.4 \Omega(\mu\text{m})^2$ and high magnetoresistance above 50% in CoFeB/MgO/CoFeB magnetic tunnel junctions, **Appl. Phys. Lett.** 89 (2006) 162507.
- Potdar, S. (2014). **Preparation and Study of Soft X-ray Multilayers.** Ph.D. Dissertation, Devi Ahilya Vishwavidyalaya.
- Rocha, S. D. F., Mansur, M. B., and Ciminelli, V. S. T. (2004). Kinetics and mechanistic analysis of caustic magnesia hydration. **J. Chem. Technol. Biotechnol.** 79: 816-821.
- Reimer, L. (1989). **Transmission electron microscopy: Physics of image formation and microanalysis.** Heidelberg: Springer.
- Samada, N. S., Mustajab, M. K. A. A., and Yacob, A. R. (2010). Activation temperature effect on the basic strength of prepared aerogel MgO (AP-MgO). **IJBAS.** 10(2): 54-57.
- Sengupta, A., Liyanagedera, C. M., Jung, B., and Roy, K. (2017). Magnetic Tunnel Junction as an On-Chip Temperature Sensor. **Sci. Rep.** 7: 11764.
- Singh, B. B., Agrawal, V. A., Joshi, G., and Chaudhary, S. (2012). X-ray photoelectron spectroscopy and conducting atomic force microscopy investigations on dual ion beam sputtered MgO ultrathin films. **Thin Solid Films.** 520: 6734-6739.
- Smithson, G. L., and Bakhshi, N. N. (1969). The kinetics and mechanism of the hydration of magnesium oxide in a batch reactor. **Can. J. Chem. Eng.** 47: 508-513.
- Stanish, M. A., and Perlmutter, D. D. (1983). Kinetics and transport effects in the dehydration of crystalline potassium carbonate hydrate. **AIChE Journal.** 29(5): 806-812.

- Stearrett, R., Wang, W. G., Kou, X., Feng, J. F., Coey, J. M. D., and Xiao, J. Q. (2012). Influence of exchange bias on magnetic losses in CoFeB/MgO/CoFeB tunnel junctions. **Phys. Rev. B.** 86: 014415.
- Sung, M. M., Kim, C., Kim, C. G., and Kim, Y. (2000). Epitaxial growth of MgO films on Si(111) by metal organic chemical vapor deposition. **J. Cryst. Growth.** 210: 651-654.
- Sutcu, M., Akkurt, S., and Okur, S. (2009). Influence of crystallographic orientation on hydration of MgO single crystal. **Ceram. Int.** 35: 2571-2576.
- Tian, R. (2014). The Development of High-Performance Calcium Cobaltates for Thermoelectric Power Regeneration. Ph.D. Dissertation, The University of New South Wales.
- Watts, J. F., and Wolstenholme, J. (2003). **An Introduction to Surface Analysis by XPS and AES.** England: John Wiley & Sons.
- Wisniowski, P., Dabek, M., Cardoso, S., and Freitas, P. P. (2013). Magnetic field sensing characteristics of MgO based tunneling magnetoresistance devices with $\text{Co}_{40}\text{Fe}_{40}\text{B}_{20}$ and $\text{Co}_{60}\text{Fe}_{20}\text{B}_{20}$ electrodes. **Sens. Actuators A.** 202: 64-68.
- Yasaka, M. (2010). X-ray thin-film measurement techniques. **The Rigaku Journal.** 26(2).
- Yoshida, T., Tanaka, T., Yoshida, H., Funabiki, T., and Yoshida, S. (1995). Study of Dehydration of Magnesium Hydroxide. **J. Phys. Chem.** 99: 10890-10896.
- Yuasa, S., and Djayaprawira, D. D. (2007). Giant tunnel magnetoresistance in magnetic tunnel junctions with a crystalline MgO(001) barrier. **J. Phys. D: Appl. Phys.** 40: R337-R354.

CHAPTER III

INFLUENCE OF GAS ATMOSPHERE ON THE DISSOLUTION BEHAVIOR OF MAGNESIUM OXIDE THIN FILM

3.1 Introduction

As mentioned in chapter 1, the dissolution reaction of MgO thin film can be influenced by many factors. In this chapter, we focus on the effect of the gas atmosphere on the dissolution mechanism of the MgO thin film. It is known that nitrogen gas (N₂), oxygen gas (O₂) and carbon dioxide gas (CO₂) are the most abundant gases present in the atmosphere and water (Boyd, 2015; Frederick, 2008). Therefore, in this chapter, the influence of gas atmospheres including N₂, O₂ and CO₂ on the dissolution of the MgO thin film is investigated.

Many studies reported that after the film was exposed to deionized water, it quickly absorbs molecules of water and produces the hydroxide layers over its surface. This could result in the change of chemical compositions of the film (Ali, 2013; Amaral, 2010; Dobrzanski, 2020; Nagamine, 2006; Santamaria, 2007; Singh, 2012). Furthermore, they further point out that those hydrated MgO thin films can dissolve by releasing the Mg²⁺ ions and OH⁻ ions into water leading to the decrease of the film thickness (Amaral, 2010; Amaral, 2011; Kosenko, 2008; Kuenzel, 2018; Hanlon, 2015). To understand the dissolution behavior of the MgO thin film, it is necessary to compare the composition as well as the thickness of the film before and after being exposed to deionized water.

In this experiment, X-ray photoelectron spectroscopy (XPS) is used to quantify the chemical composition and thickness of the film. Scanning electron microscope (SEM) is used to analyze the film surface morphology. The dissolution profile of the MgO thin film is quantified by using a combination of focus ion beam and scanning electron microscope (FIB-SEM) cross-sectional as well as *in situ* XPS depth profiling. In addition, the concentration of Mg²⁺ ions in the deionized water obtained from the atomic absorption spectroscopy (AAS) results were converted to calculate the MgO thin film thickness. Furthermore, the relationship between the chemical composition, microstructural and thickness, a qualitative model is finally proposed to explain the dissolution mechanism of the MgO thin film.

This chapter is organized as follows: section 3.2 describes the experimental procedure used in this study; section 3.3 demonstrates the results which obtained from various analysis techniques including XPS (section 3.3.1), SEM (section 3.3.2), FIB-SEM cross-sectional (section 3.3.3), AAS (section 3.3.4), and pH measurement (section 3.3.5). The model of dissolution mechanism in water of the MgO thin film is proposed in section 3.3.6. Finally, section 3.4 is the conclusion of this chapter.

3.2 Experimental procedure

3.2.1 Sample Preparation

MgO (001) thin films with 50 nm of thickness deposited on a Si substrate were supplied by Western Digital Technology (Thailand) Co., Ltd. The sample was cut into 1.5 × 1.5 cm² square shapes using a diamond scribe. The photoresist layer, designed to protect the film surface, was removed using acetone. Then, the completely removed photoresist MgO thin films were mounted on a custom-built fixture cell, as shown in

Figure 3.1(a). A Viton O-ring was used to control the dissolved area such that only the top of film surface was exposed to deionized water (DI water).

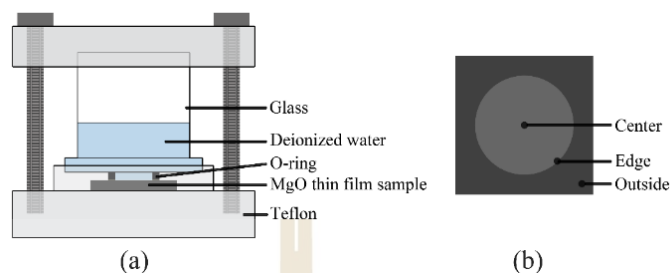


Figure 3.1 Schematic diagram of (a) the custom-built fixture cell and (b) the dissolved region of MgO film sample after being exposed to deionized water.

In the meantime, three different gases; nitrogen (N_2), oxygen (O_2), and carbon dioxide (CO_2), were flowed into DI water, which was then cover on the MgO films. The gas flow rate was controlled by using mass flow controllers (MFC). The pH of the DI water was recorded at three different stages: 1) before being saturated with gas; 2) being saturated with gas; and 3) finally, after the dissolution process of the MgO films. The MgO films were exposed to DI water which saturated by different gases for either 1 hour or 4 hours. This study therefore comprises six conditions of MgO thin films, which we denote as 1h- N_2 , 4h- N_2 , 1h- O_2 , 4h- O_2 , 1h- CO_2 and 4h- CO_2 . The experimental procedures of this study are exhibited in a schematic diagram in Figure 3.2.

3.2.2 Characterizations

XPS measurements were performed by using a PHI 500 Versaprobe-II located at Beamline 5.3, Synchrotron Light Research Institute (SLRI). An Al $K\alpha$ monochromatic X-ray source (1486.6 eV) in PHI 500 was applied for acquiring XPS spectra. An electron neutralizer was used to compensate the charging effects in case of

the insulator surface. For depth profile study, the MgO thin film samples were etched by 1 kV *in situ* argon ions (Ar^+) with a beam current of 20 mA and $2 \times 2 \text{ mm}^2$ of the beam raster scan. High-resolution spectra of all elements were recorded using 22.4 eV of pass energy and 0.1 eV of a step size. Then, for data analysis, the functional composition of each core level was curve-fitted using the CasaXPS software.

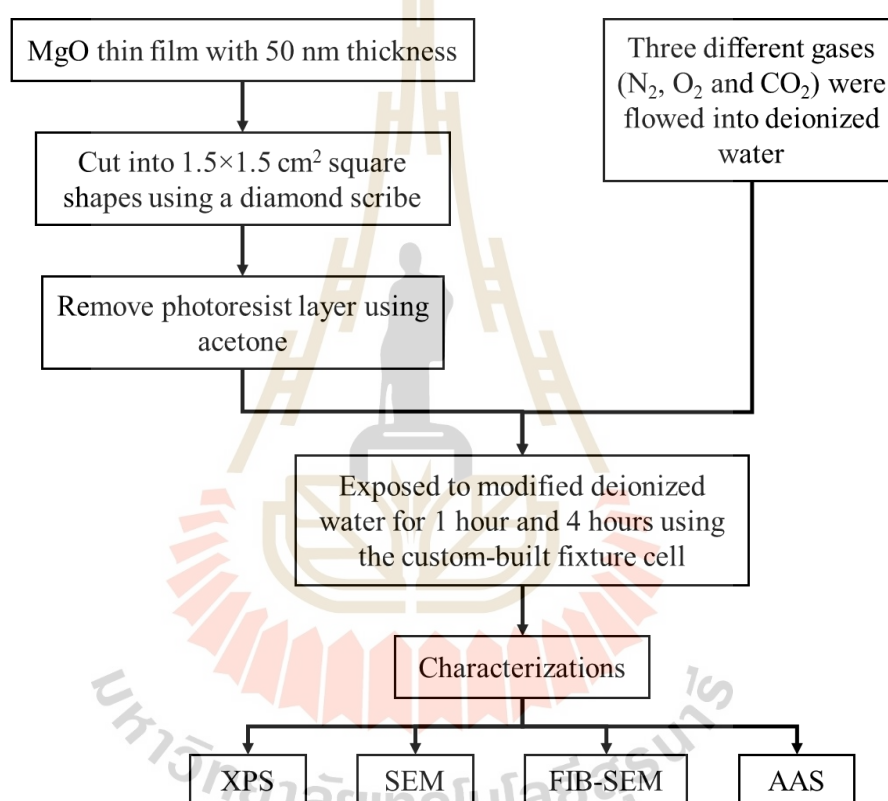


Figure 3.2 Schematic diagram of the experimental procedure of the investigation of influence gas atmosphere on the dissolution of MgO thin film.

An in-built Focused Ion Beam and Field-Emission Scanning Electron Microscope (FIB-SEM) was used to determine the surface morphology and the MgO thin film thickness. Three different points of the dissolution regions on the film surface,

as demonstrated in Figure 3.1(b), were cut cross section by Carl Zeiss AURIGA® CrossBeam® Workstation using a focused Ga⁺ ion beam. Cross-sectional images were recorded at a 36° take-off angle using high-resolution SEM. To quantify the concentration of Mg ions which dissolved in deionized water, samples of the deionized water after the dissolution processes were retained and analyzed using atomic absorption spectroscopy (AAS: Perkin Elmer, PinAAcle900).

3.3 Results and Discussion

3.3.1 XPS Results

3.3.1.1 Thickness of the MgO Thin Film

The integration of XPS and ions sputtering/etching was used to characterize the depth profile of the MgO thin films. The XPS spectra of the pristine MgO thin film before and after ions etching at 2, 60 and 120 minutes are presented in Figure 3.3. These results reveal that at the beginning, the film is covered by a hydroxide layer and carbon which is likely natural contamination (Parra, 2010).

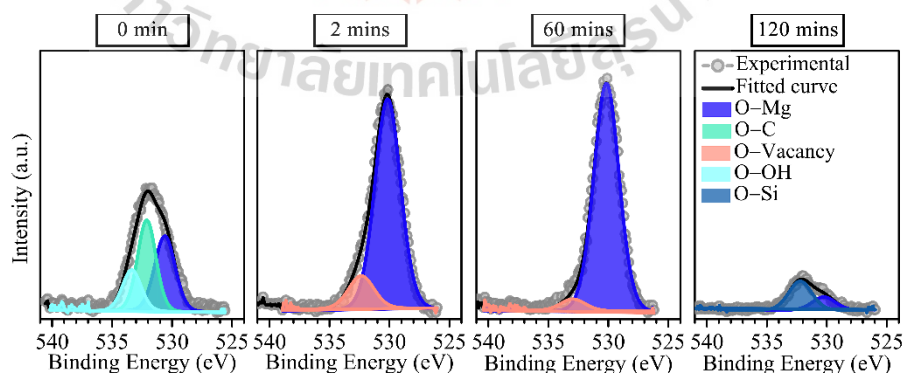


Figure 3.3 High-resolution O *1s* spectra after 0, 2, 60, and 120 minutes of sputtering of a pristine MgO thin film.

This contamination was removed by Ar⁺ ions sputtering within 1 to 2 minutes. From Figure 3.3, if it is assumed that the sample is homogeneous, then the quantity of photoelectrons of an element depends on the atomic concentration of that element in the sample (Barrio, 2012; Heide, 2012). The maximum intensity and the relative sensitivity factor of a peak were used to quantify the relative atomic concentrations of the several constituents of the thin film surface (Barrio, 2012; Heide, 2012). The intensity (*I*) of a photoelectric peak of a specified element can be expressed as

$$I = nF_s \quad (3.1)$$

$$F_s = nf\sigma\theta y\lambda AT \quad (3.2)$$

where *n* is the number of atoms per cm³ of the element in the sample and *F_s* is sensitivity factor which is obtained from OPERATOR'S PHI MultiPak™ Software Manual (2012). *F_s* depends on the X-ray flux *f* (photons/cm²·sec), the photoelectric cross-section *σ* (cm²) of the atomic orbital of interest, the angular efficiency factor *θ* of the instrumental arrangement based on the angle between the photon path and detected electron, the efficiency in the photoelectric process *y* of formation of photoelectrons of the normal photoelectron energy, the inelastic electron mean free path *λ*, the area of the sample *A* from which photoelectrons are detected, and the detection efficiency *T* of electrons emitted from the sample.

If the observed elements are detected on the film surface, the concentration of the interested element can be calculated using (Heide, 2012; Parra, 2010; Ulvac-PHI, 2012):

$$C_x = \frac{n_x}{\sum n_i} = \frac{I_x/F_s}{\sum I_i/F_i} \quad (3.3)$$

where C_x is the atomic concentration of one element in percentage. I_x is the maximum intensity of a photoelectric peak of interested element. I_i is the maximum intensity of a photoelectric peak of each element in sample. F_i is the sensitivity factor of each element in the sample.

By employing Equation (3.3), a plot of the atomic concentration of elements as a function of sputtering time of the pristine MgO thin film is presented in Figure 3.4. The result reveals that the film consists of the C $1s$, Mg $2p$ and O $1s$ at the same concentration before the Ar^+ ions etching begins (at 0 min).

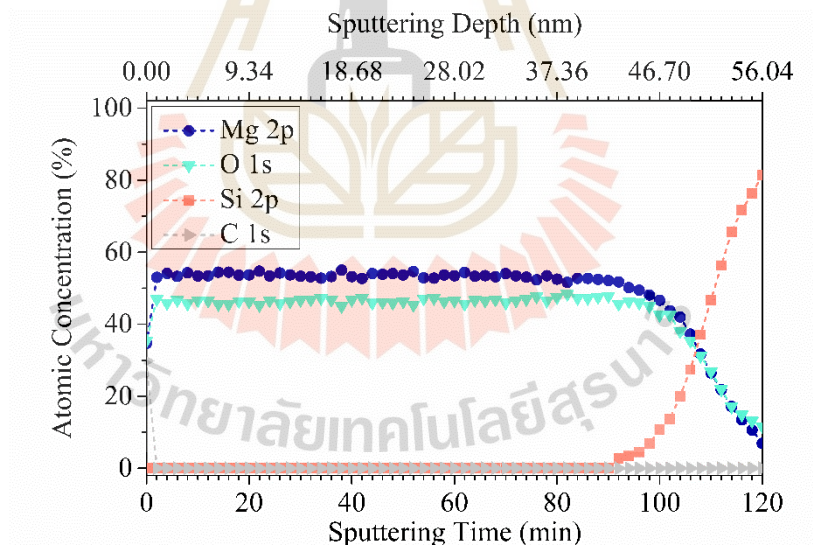


Figure 3.4 XPS depth profile of a pristine MgO thin film.

After the film is bombarded by Ar^+ ions, the C $1s$ signal decreases to approximately zero whilst the Mg $2p$ and O $1s$ concentrations abruptly increase to 50% and then remain stable. After 92 minutes of sputtering, the Mg $2p$ and

O $1s$ concentrations slowly decrease to zero while the Si $2p$ signal, from the silicon substrate, monotonically increases. This expected result is due to the interfacial layer of the MgO/Si and the Si substrate.

Theoretically, the change of the atomic concentration according to the sputtering time is associated with the stoichiometry and the thickness of the films (Kuenzel, 2018). To convert the sputtering times into film thickness, the known thickness standard of the MgO thin film is sputtered (Parra, 2012), and the sputtering rate is then calculated using

$$\text{Sputtering rate} = \frac{\text{Thickness}}{\text{Sputtering time (minute)}} \quad (3.4)$$

In this study, a pristine MgO thin film with 50 nm thickness was used as the standard and sputtering rate of the film is indicated by the point that the Mg $2p$ line intersects with the Si $2p$ line (at 107 minutes). Thus, the sputtering rate of MgO is approximately 0.467 nm/min.

Table 3.1 Estimation of MgO thin film remaining thickness using various techniques.

Conditions	Thickness (nm)		
	XPS	FIB	AAS
1h-N ₂	40.6	30	43.7
1h-O ₂	39.2	23	40.7
1h-CO ₂	0	2	22.5
4h-N ₂	2.8	13	17.5
4h-O ₂	0	3	13.5
4h-CO ₂	0	0	0

Using Equation (3.4), the remaining thickness of each MgO thin film sample is shown in Table 3.1. A plot of the atomic concentration as a function of sputtering time/depth obtained at the center point of the dissolved regions (see Figure 3.1(b)) of the six MgO thin films is presented in Figure 3.5.

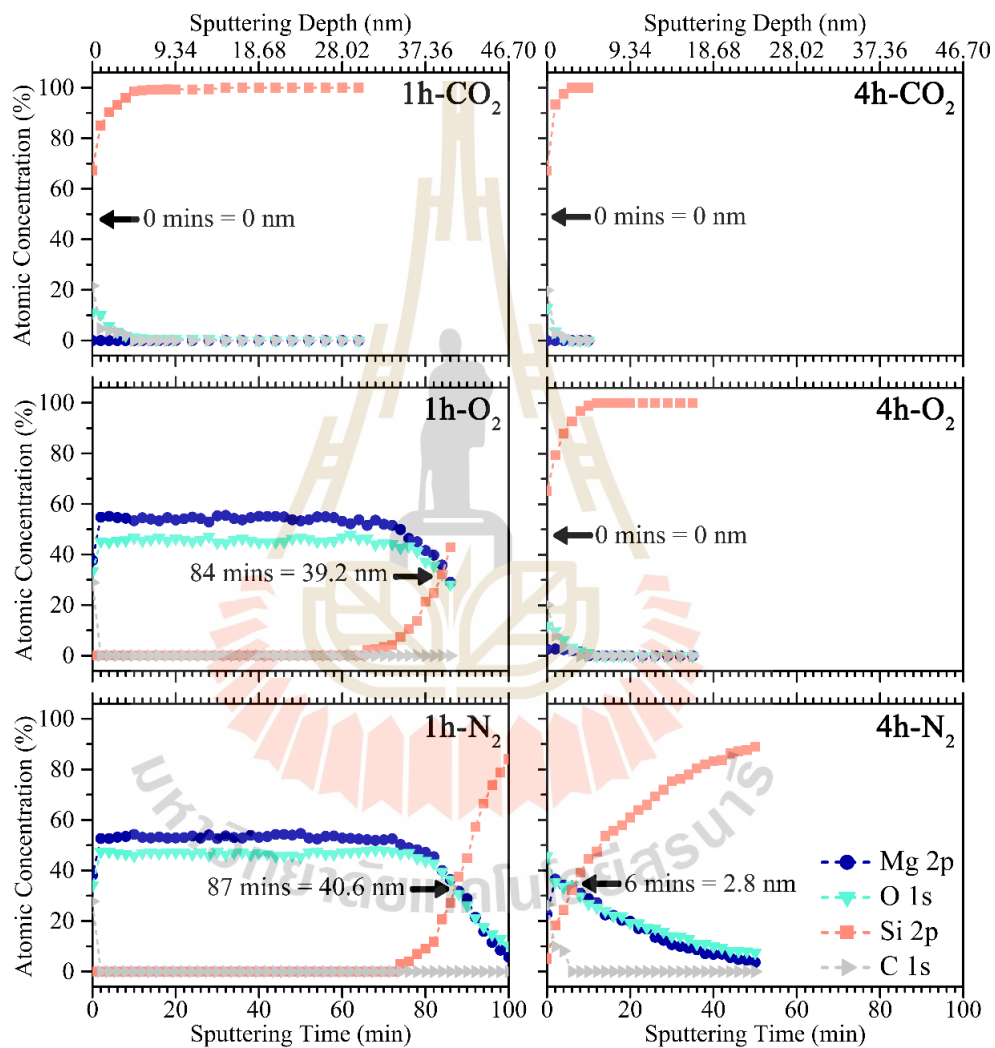


Figure 3.5 Depth distribution of MgO thin film atomic concentrations after being dissolved in deionized water under different gas atmospheres. The remaining thickness of the films is indicated by the black arrow.

These results demonstrate that the trend of the depth profile of 1h-N₂ and 1h-O₂ is similar to the pristine sample while those of 4h-N₂, 4h-O₂, 1h-CO₂ and 4h-CO₂ are relatively divergent. These differences are attributed to the different remaining thickness of the MgO thin film. It is obvious that the film thickness dramatically decreases in CO₂-saturated DI water and it slightly decreases under N₂-saturated DI water at the same immersion time. It is found that 1h-N₂ shows the highest remaining MgO film thickness fraction while the lowest remaining thickness belongs to 1h-CO₂, 4h-O₂ and 4h-CO₂.

The decrease in film thickness is a result of the dissolution of the MgO thin film in DI water. After the film is covered with gas-saturated DI water, it reacts with water molecules and then dissolves in DI water. It is found that the film reacts strongly with CO₂-saturated DI water, while it only slightly reacts with O₂-saturated DI water and N₂-saturated DI water. This could be attributed to the pH value of DI water after being saturated by different gases. Moreover, the result shows that the CO₂ significantly dissolves in DI water and reduces the pH of the water while the O₂ and N₂ dissolve in a small amount in DI water (Gevantman, 2013); this will be discussed later in section 3.4 (effect of deionized water pH).

3.3.1.2 Formation of Mg(OH)₂

To determine the changing of the electronic structure of MgO thin films after being covered with DI water, the high-resolution spectra of all element were deconvoluted and considered. Overall spectra were calibrated by using Ar 2*p* spectra at binding energy of 243 eV (Bukhtiyarov, 2006; Denisenko, 2010; Oswald, 2018) to eliminate any positive charge-induced binding energy shift. The secondary electron background of all spectra was subtracted by a Shirley function. A linear

combination of 70% Gaussian and 30% Lorentzian peak shape was used to extract the chemical bonding of elements from the respective surface core level (Parra, 2012). All subpeak of the O $1s$ spectra were used Full-width-at-a-half-maximum in a range of 1.5 to 2 eV (Febvrier, 2017; Fotea, 2006). The characteristics were computed to obtain the best fit of the experiment curve following a least squares minimization method. A significant change of shape and intensity of O $1s$ spectra at selected sputtering times of the six samples are compared in Figure 3.6 and Figure 3.7.

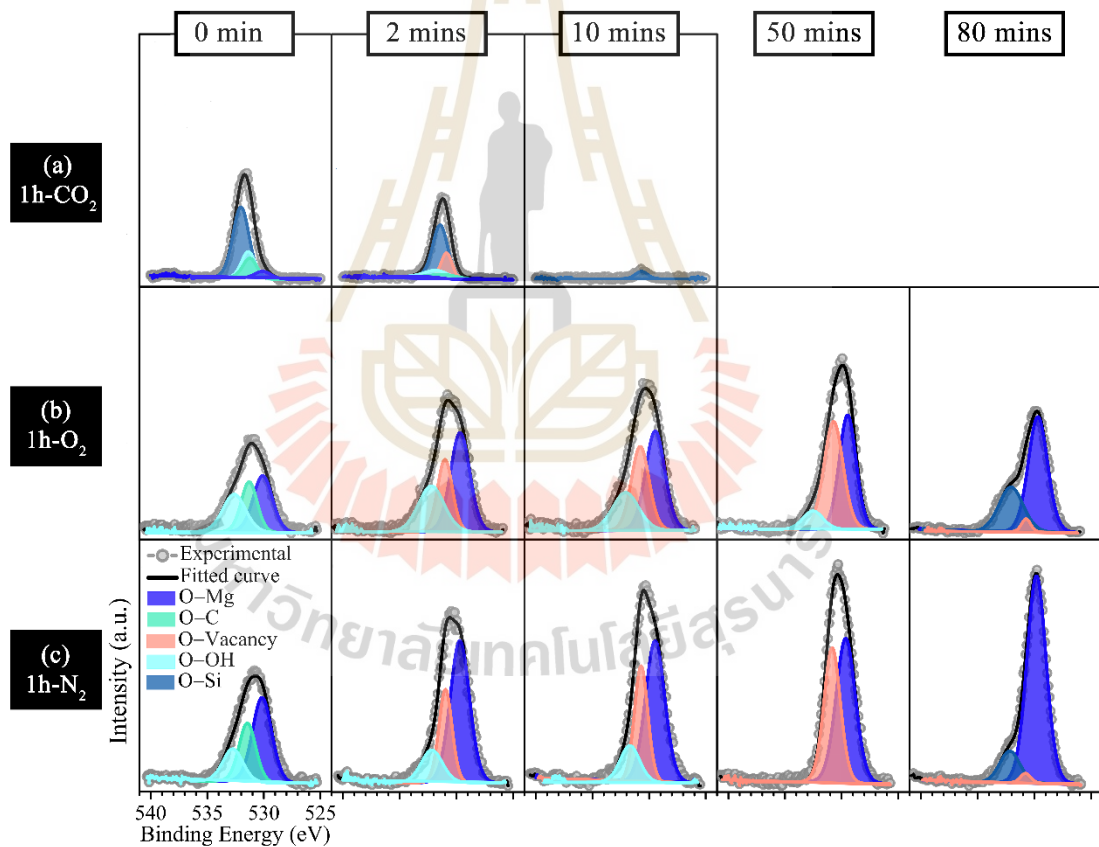


Figure 3.6 Variation of high-resolution O $1s$ spectra which obtained from the MgO thin film after being dissolved in deionized water under different gas atmospheres for 1 hour.

Figure 3.6 presents representative high-resolution O *1s* spectra of the samples immersed for 1 hour before and after 2, 10, 50 and 80 minutes of *in situ* Ar⁺ ions sputtering. Before *in situ* Ar⁺ ions bombardment begins (at 0 min), the high-resolution O *1s* spectra can be deconvoluted into three subpeaks at 530.1, 531.4 and 532.7 eV for 1h-N₂ and 530.0, 531.2 and 532.6 eV for 1h-O₂. On the other hand, the O *1s* spectra of 1h-CO₂ can be deconvoluted into four subpeaks at 530.1, 531.2, 532.3 and 533.0 eV. The observed subpeak at binding energy of 533.0 eV of 1h-CO₂ is identified as the bonding of O–Si in the SiO₂ lattice (binding energy at 532.8 ± 0.2 eV) (Lu, 2010). This indicates that the film was wholly dissolved and the silicon from the substrate was detected from the beginning (see Figure 3.5).

In addition, other subpeaks observed at 530.1 ± 0.2 eV is identified as O–Mg in the lattice of MgO (Dillip, 2016; Rocha, 2004; Zhu, 2015) and subpeak at 532.5 ± 0.2 eV is indicated as O–OH in Mg(OH)₂ (Dillip, 2016; Yin, 2014). This implies that the film absorbs the molecules of water and its chemical composition transforms into Mg(OH)₂ (Kuenzel, 2018; Yao, 2000). Besides the O–OH and O–Mg subpeaks, observed subpeak at 531.3 ± 0.2 eV are attributed to the bonding of O–C in MgCO₃ from carbon contamination (Dillip, 2016; Rocha, 2004; Parra, 2010; Yin, 2014). After 2 minutes of *in situ* Ar⁺ ion sputtering, the O–C subpeaks are completely eliminated from 1h-N₂ and 1h-O₂. It results in the increasing of the O *1s* spectra intensity and shifting of peak position 0.1 – 0.2 eV toward a lower binding energy. In the meantime, another subpeak at a binding energy of 530.7 ± 0.2 eV is observed in every condition. It is identified as the oxygen-deficient regions within the MgO lattice. These vacancies could be a result of the removal of the oxygen atoms from the MgO lattice during the bombardment of *in situ* Ar⁺ ions (Ridier, 2016; Zhu, 2015). After 10

minutes of sputtering, the intensity of O $1s$ spectra of 1h-CO₂ considerably decreases to nearly zero while those of 1h-N₂ and 1h-O₂ remain as it is. It can be seen that the bonding of O–OH is still detected in 1h-N₂ and 1h-O₂. This evidence points out that the water molecules do not only absorb on the film surface, but they also infiltrate into the deeper layer of the MgO thin film. These interactions can induce the transformation of the film chemical composition from MgO into Mg(OH)₂. Interestingly, after 50 minutes of sputtering, the O–OH subpeak disappears from 1h-N₂ whilst it is still detected in 1h-O₂. This indicates that the thickness of the Mg(OH)₂ in 1h-N₂ is thinner than that of 1h-O₂. This could be because the MgO thin film can absorb the DI water which is saturated by the different gas atmosphere. After 80 minutes of sputtering time, the O–Si subpeak shows up in both of the MgO samples, indicating that the MgO/Si interlayer is reached.

Next, the immersion time was increased to 4 hours, and the change of chemical composition and dissolution behavior was determined again. Figure 3.7 presents the deconvolution of the high-resolution O $1s$ spectra of the samples before (0 min) and after 2, 10 and 50 minutes of sputtering. The results show that before the Ar⁺ ions etching begins, the O $1s$ spectra of 4h-N₂ can be extracted into three subpeaks at 529.9, 531.2 and 532.2 eV. Unlike the previous samples, the O $1s$ spectra of 4h-O₂ and 4h-CO₂ can be deconvoluted into four subpeaks at 530.0, 531.4, 532.4 and 532.8 eV for 4h-O₂ and at 530.1, 531.4, 532.3 and 532.9 eV for 4h-CO₂. This is because the signal from the silicon substrate is detected in 4h-O₂ and 4h-CO₂. The coexistence of the O–Mg, the O–OH and the O–Si subpeaks in 4h-O₂ and 4h-CO₂ indicates that the hydroxide layer forms at the MgO/Si interlayer region. Furthermore, it could exist in the magnesium silicate phase. After 2 minutes of sputtering, the O $1s$ spectra of all sample drops. The O–Si subpeak is observed in all samples. At 10 minutes of sputtering,

the O $1s$ spectra of 4h-O₂ and 4h-CO₂ drastically reduce to zero. It reflects that no oxide/hydroxide film is observed on the silicon substrate. However, the O $1s$ spectra of 4h-N₂ still remains until 50 minutes of sputtering. It can be observed that the bonding of O–OH is not detected at 10 minutes. This can be assumed that the O–OH subpeak is eliminated from 4h-N₂ after 4-8 minutes of sputtering.

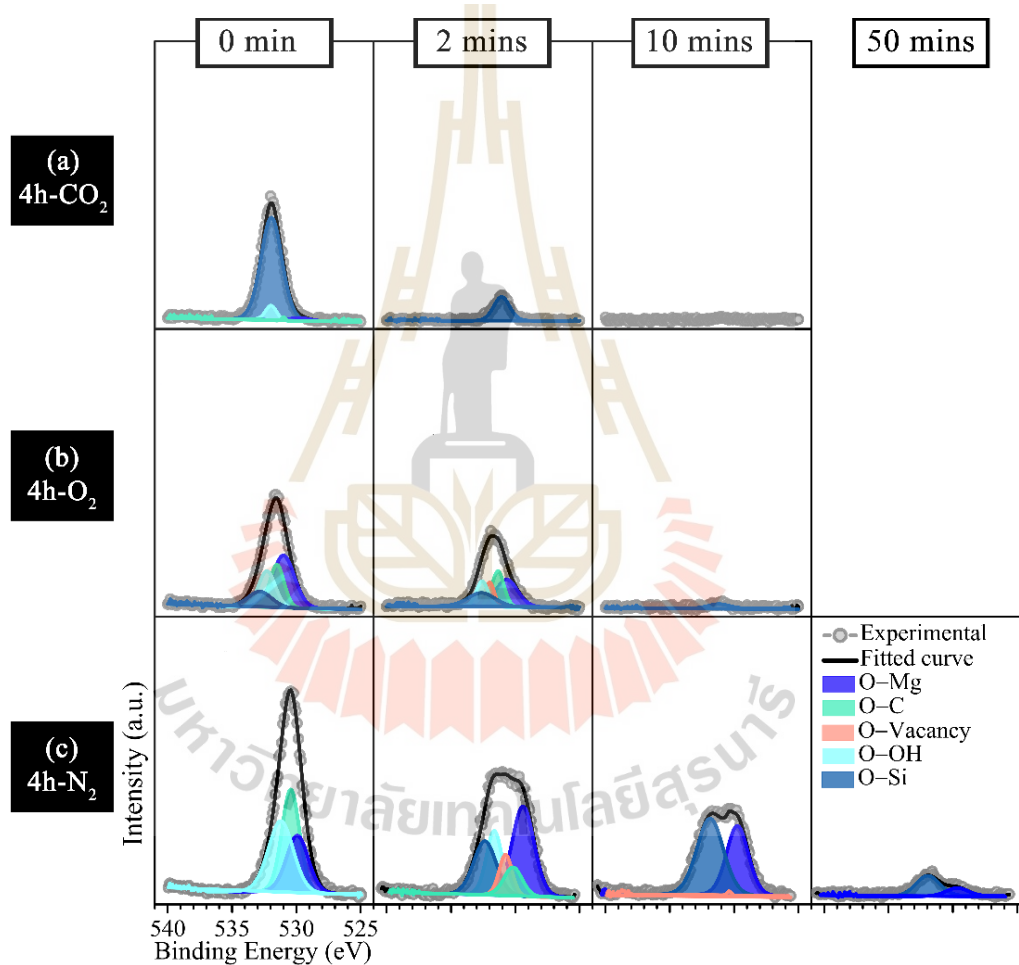


Figure 3.7 High-resolution O $1s$ spectra of MgO thin film after being dissolved in deionized water under different gas atmospheres for 4 hours.

To quantify the thickness of the $\text{Mg}(\text{OH})_2$ layer, the integrated peak intensity of O–OH subpeak of high-resolution of O $1s$ spectra, as displayed in Figure 3.6 and Figure 3.7, are converted to the $\text{Mg}(\text{OH})_2$ atomic concentration and then plotted as a function of sputtering time in Figure 3.8. The result shows that all samples transformation of MgO thin film into the hydroxide layer. Thus, the thickness of the $\text{Mg}(\text{OH})_2$ layer is possibly varied according to the remaining thickness of the MgO thin film (see Figure 3.5). However, the $\text{Mg}(\text{OH})_2$ is still observed in 1h- CO_2 , 4h- O_2 and 4h- CO_2 although the MgO thin film does not exist in these sample.

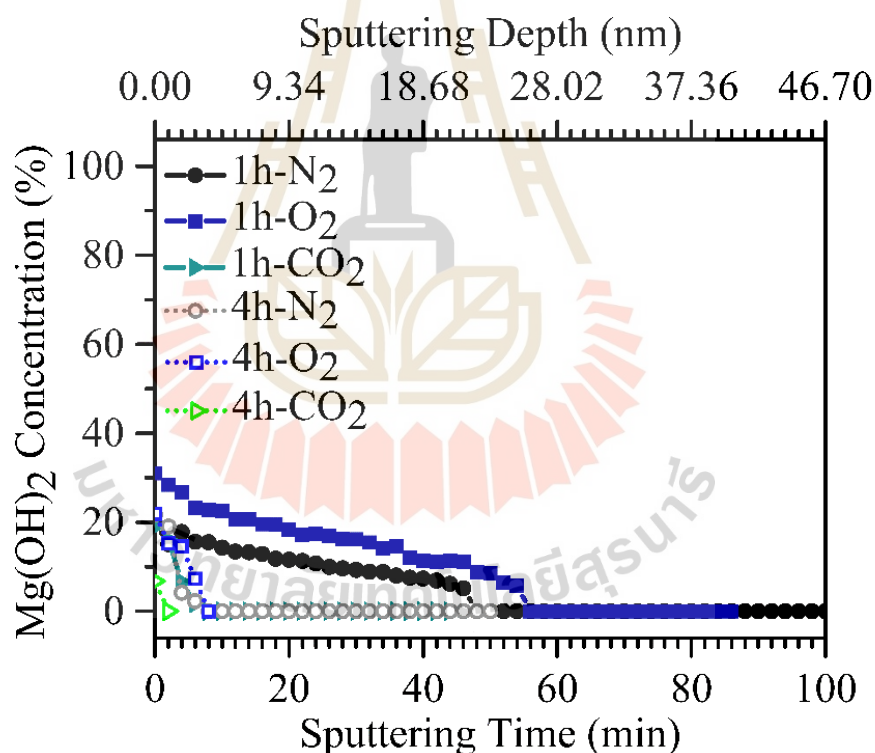


Figure 3.8 Atomic concentration of $\text{Mg}(\text{OH})_2$ as a function of sputtering time.

This is because the hydroxide layer form at the MgO/Si interlayer region of these sample. Furthermore, we found that 1h- O_2 produces the

thicker $\text{Mg}(\text{OH})_2$ layer compared to 1h- N_2 . It is because the N_2 -saturated DI water could absorb on the film surface slower than those of O_2 -saturated DI water. The profile of $\text{Mg}(\text{OH})_2$ layer and MgO film after being covered with gas-saturated DI water is presented in Figure 3.9.

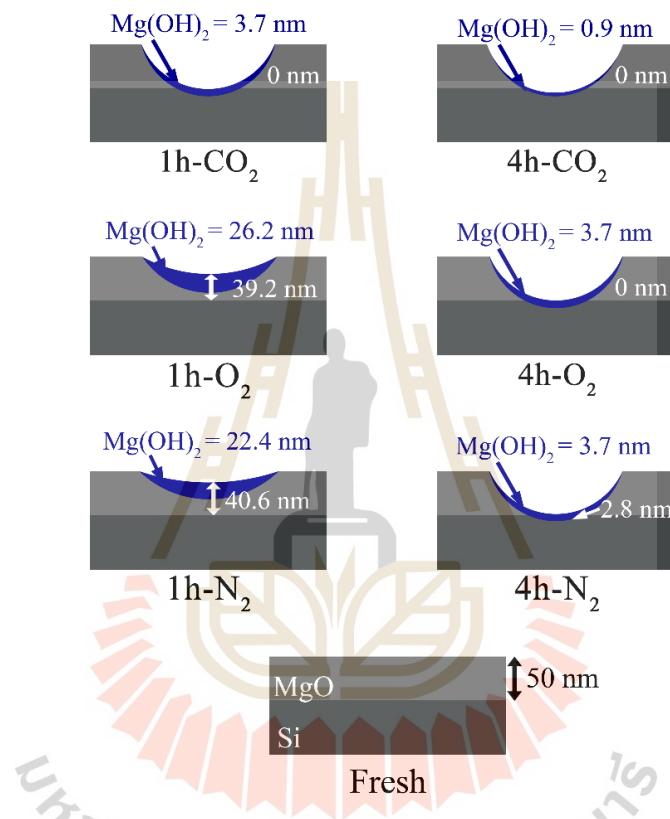


Figure 3.9 Schematic representation of the remaining thickness of the MgO thin film and the thickness of the $\text{Mg}(\text{OH})_2$.

3.3.2 SEM Results

The surface microstructures at the edge of the dissolved region (see Figure 3.1) of the MgO thin films after being covered with gas-saturated DI water were examined by using SEM; the results are shown in Figure 2.10. The micrographs exhibit that after being covered with gas-saturated DI water, new coral-like clusters are formed

over the film surface. Interestingly, it is further found that the development of the clusters strongly depends on the gas and immersion time. The degree of development of the clusters on the surface of 1h-O₂ is greater than those of 1h-N₂ and 1h-CO₂. Furthermore, the number of clusters also dramatically increase with an increase of immersion time in the case of 4h-O₂ and 4h-N₂. On the other hand, there are no new clusters over 4h-CO₂ surface. This is because the dissolution rate of the MgO thin film being covered with CO₂-saturated DI water is greater than those of the other gases. According to the XPS results, as shown in Figure 3.6 and 3.7, the bonding of O–OH is detected after the deconvolution of O 1s spectra. It may indicate that the new clusters developed over the sample surfaces could be Mg(OH)₂ layer that formed during the dissolution process.



Figure 3.10 SEM micrographs (magnification $\times 10000$) of MgO thin films after being dissolved in deionized water.

3.3.3 FIB-SEM Cross-Sectional Result

Figure 3.11 presents the FIB-SEM cross-sectional image at three points of the dissolved region of each sample. The different contrast in the images refers to the dissolved region of each sample. The different contrast in the images refers to the different morphology of film and substrate. The darker area corresponds to the substrate region while the brighter area refers to the film region. The remaining thickness of the MgO thin films is evaluated from the cross-sectional images at the three points of the dissolved regions (see Figure 3.1(b)) and illustrated in Figure 3.12.

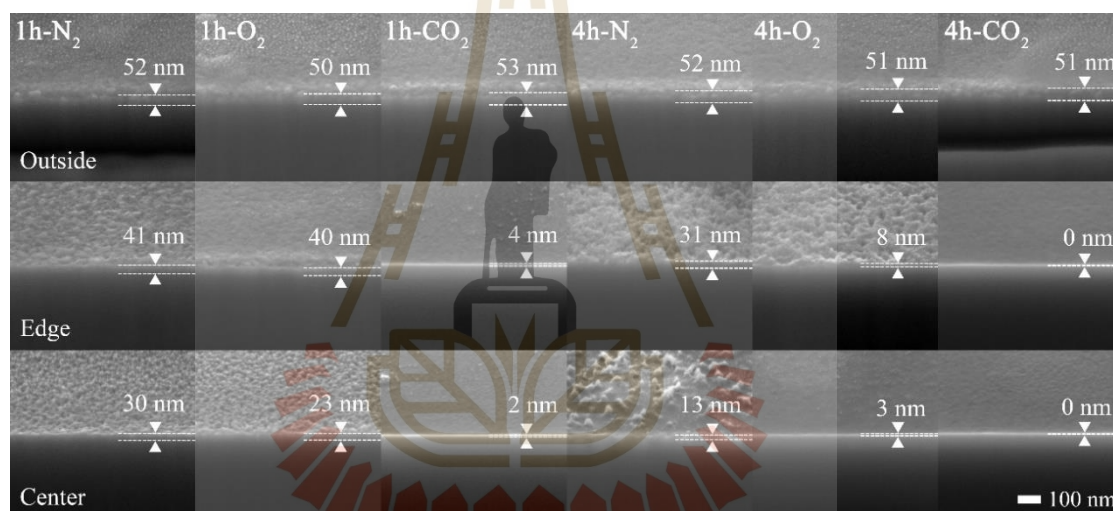


Figure 3.11 FIB-SEM cross-sectional micrographs at three points of the dissolved regions of six MgO thin film samples (Magnification: $\times 100000$).

The thickness of the films at the outside of the dissolved regions remains at ~ 50 nm, corresponding to the thickness of the pristine sample, as expected since this region of the film is not exposed to water. On the other hand, the film thickness at the other points decreases. We found that the thickness of the MgO thin films at the edge of the dissolved regions remains thicker than those at the center of the dissolved regions.

It possibly relates to the capillary action of water which makes the film at the center point absorbs the molecule of water greater than the other points resulting in the higher dissolution rate at that point. The results show that 1h-N₂ possess the thickest remaining film while the thinnest remaining film belongs to 4h-CO₂. The remaining thickness of the films at the center of the dissolved region are summarized in Table 3.1.

From FIB-SEM cross-sectional results, we presume the cross-sectional profile of the film after being dissolved as similar to a spherical cap shape and display as an inset in Figure 3.12. This dissolution profile is used as the model to convert the Mg concentration obtained from the AAS results into the thickness of the film, described next.

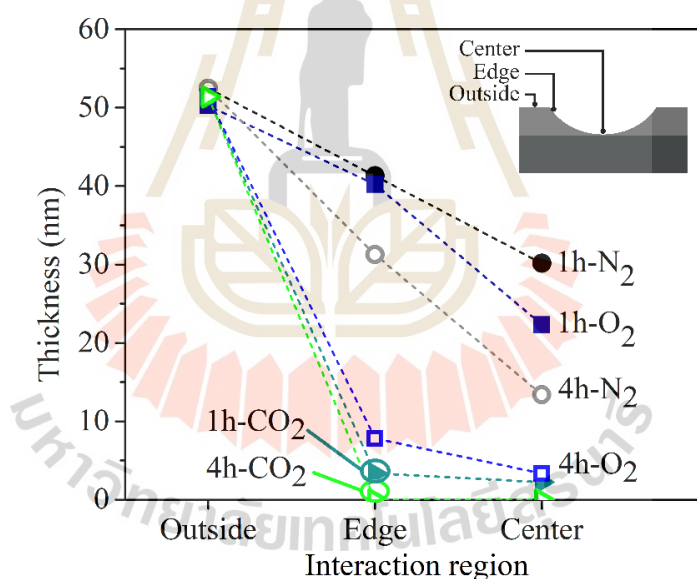


Figure 3.12 The remaining thickness of MgO thin films estimated by FIB-SEM.

3.3.4 Atomic Absorption Spectroscopy (AAS)

Figure 3.13 shows the concentration of Mg ions in the DI water, obtained from the different dissolution processes. The results demonstrate that at the same immersion time, the Mg concentration is highest in the dissolution under CO₂ and

lowest in the dissolution under N₂. This could relate to the reduction of the film thickness as observed in XPS and FIB-SEM cross-sectional results. The concentration of Mg can be calculated by using the following equation

$$C_{MgO} = M/V_{DI} \quad (3.5)$$

where C_{MgO} is the Mg concentration (mg/L) M is the mass (mg) of the MgO thin film, which is dissolved in the volume, V_{DI} of deionized water (L).

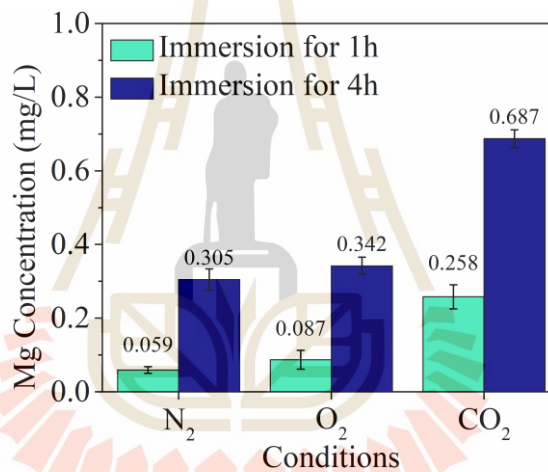


Figure 3.13 Mg concentration of MgO thin film which dissolved in deionized water under different gas atmospheres.

The dissolution profile of the MgO thin films is assumed to be a spherical cap shape as displayed in Figure 3.12. The volume of a spherical cap V_s (nm³) can be expressed by the formula (Polyanin, 2007)

$$V_s = \frac{\pi h}{6} (3a^2 + h^2), \quad (3.6)$$

where a is a radius of the cap circle or the dissolved region (nm). The mass of MgO thin film (in mg) can be given as $M = DV_s$ while D is the density of the MgO (3580×10^{-21} mg/nm³). Hence, the height of the spherical cap or the thickness of the dissolved film (nm), h can be calculated by combining Equations. (3.5) and (3.6) and expressed as

$$\pi Dh^3 + 3a^2\pi Dh - 6C_{MgO}V_{DI} = 0. \quad (3.7)$$

Therefore, if the thickness of pristine MgO thin film, $T_{standard}$ is 50 nm, the remaining thickness of the films (T_{Remain}) can be estimated by

$$T_{Remain} = T_{standard} - h \quad (3.8)$$

The remaining thickness of the MgO thin film estimated from AAS results using the Equation (3.8) are displayed in Table 3.1. The trend of the change of remaining thickness obtained from AAS is in agreement with that from the FIB-SEM cross-sectional and XPS.

3.3.5 Effect of Deionized Water pH

Table 3.2 presents a plot of the pH values of DI water obtained from three different intervals: 1) before being saturated with gas, 2) after being saturated with gas and 3) finally, after the dissolution process of the MgO films. The pH of DI water before flowing gas is 5.95. After being saturated with gas, the pH of the DI water changed. Interestingly, the pH values slightly decrease in case of the N₂ and the O₂. Unlike the previous cases, pH of the CO₂-saturated DI water dramatically decreases to 2.68. These changes could be attributed to the reaction between DI water and each gas. The International Union of Pure and Applied Chemistry (IUPAC) reported that the

solubility of CO₂ is 6.15×10⁻⁴ where as O₂ and N₂ are 2.293×10⁻⁵ and 1.183×10⁻⁵, respectively (Gevantman, 2003). This confirms that the CO₂ dissolves in water higher than N₂ and O₂.

Table 3.2 The pH values of deionized water obtained before flowing gas after flowing gas, and after the dissolution process.

		Conditions								
	Before flowing gas	After flowing gas			After the dissolution process					
		N ₂	O ₂	CO ₂	1h-N ₂	1h-O ₂	1h-CO ₂	4h-N ₂	4h-O ₂	4h-CO ₂
pH	5.95	5.69	5.66	2.68	5.96	5.98	4.2	6.12	6.17	4.46

Generally, the pH of water is determined by the balance of the H⁺ and OH⁻ ions dissolved in water, the higher number of H⁺ ions, the lower pH value (Boyd, 2011; Saker, 2007; Starr, 2011). It is possible that the gas interacts with the H₂O molecule and then induces the deprotonation of the hydrogen atoms from the water molecule causing the reduction of pH value of DI water. This is the reason why we observed the decreasing of pH in case of CO₂. The chemical interaction between CO₂ and water is shown as Equation (3.9) (Dobrzanski, 2020; Knoche, 1980; Taheri, 2014)



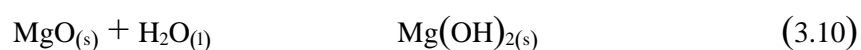
It is clearly seen that the CO₂ interacts with deionized water and produces carbonic acid/bicarbonic acid. This is why the dissolution rate of the MgO thin film under CO₂ is greater than that of O₂ and N₂, respectively.

After that, the DI water from the dissolution process was collected. It is found that the pH of DI water tends to increase in every condition while the most significant change of pH is observed in 4h-CO₂. Bharadwaj *et al.* (2013) suggested that the higher H⁺ ion concentration in low pH of DI water can lead to a higher dissolution rate of the MgO. In addition, Simpson *et al.* (2002) reported that when MgO is exposed to acid, the acidic media adsorbs on the MgO surface leading to surface reconstruction through production of the Mg(OH)₂ layer. Then, Mg²⁺ ions and OH⁻ ions are liberated from the Mg(OH)₂ film and dissolve into the acid solution. These OH⁻ ions dissolved in DI water could result in the increasing of DI water pH as we observed in the DI water obtained from the dissolution process.

3.3.6 MgO Dissolution Mechanism

To gain the more understanding of the dissolution behavior of the MgO thin film, the possible reaction mechanism of MgO thin film during being exposed to DI water are concluded from the overall results obtained from several techniques and exhibited as a schematic drawing in Figure 3.14.

After the MgO thin film is covered with DI water, the film rapidly absorbs the molecules of water on their surface and transforms their chemical composition into Mg(OH)₂ as described by (Dobrzanski, 2020; Hanlon, 2015)



It is further found that the water molecules continuously infiltrate into the deeper layer of the film resulting in the transformation of the film chemical composition in the deep into Mg(OH)₂ as observed in XPS depth profile results (Figure 3.5 and 3.6).

The $\text{Mg}(\text{OH})_2$ layer formed on the film surface starts dissolving in DI water by releasing the OH^- ions into the water. Then, the MgOH^+ layer is reconstructed over the film surface (Equation (3.11)) (Amaral, 2010; Amaral, 2011; Hanlon, 2015), which is clearly observed in the SEM images (Figure 3.10).

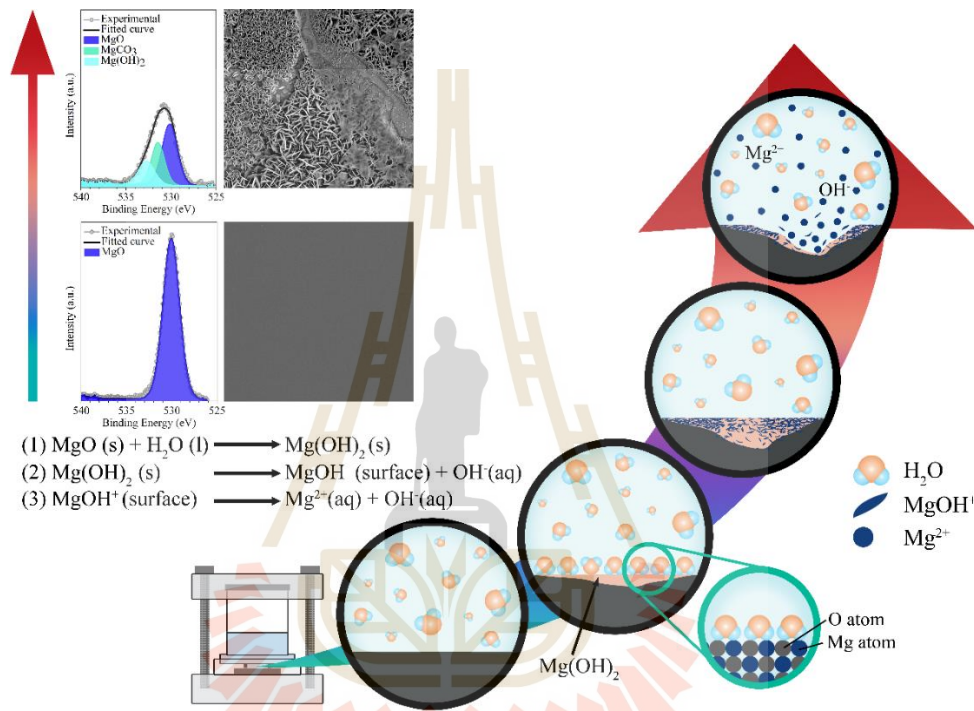
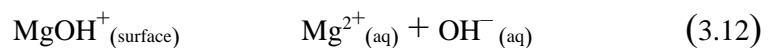
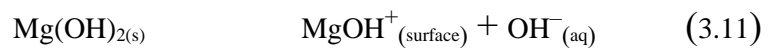


Figure 3.14 Schematic diagram of the dissolution mechanism model of the MgO thin film during being exposed to deionized water.

The hydroxide layer continuously releases Mg^{2+} and OH^- into the deionized water, as displayed in Equation (3.12) (Amaral, 2010; Amaral, 2011; Hanlon, 2015), resulting in a decrease of the film thickness.



3.4 Chapter Summary

In this chapter, a profound dissolution mechanism of MgO thin film in DI water under the influence of gas atmospheres (N_2 , O_2 and CO_2) is presented. The results demonstrate that the MgO thin films react with the DI water by the absorption of the water molecules into their surface. Then, water molecules infiltrate into the deeper layer of the film causing the transforming of film chemical composition into $Mg(OH)_2$, as observed in XPS depth profile results. It is found that the $Mg(OH)_2$ layer is thickest in 1h- O_2 . Furthermore, AAS results reveal that the film dissolves by releasing Mg^{2+} and OH^- ions into the DI water. These dissolutions modify the film surface morphology and cause a decrease in the film thickness. It was observed that the film thickness dramatically decreases in case of the dissolution under CO_2 while it only slightly decreases under O_2 and N_2 . This is because the different gas atmospheres affect the DI water pH differently. It is found that the CO_2 can react with the molecules of water and produces carbonic acid/bicarbonic acid resulting in the reduction of the pH value of DI water, while on the other hand, N_2 has no reaction with the DI water. These results provide detailed understanding of the influence of various gas atmospheres on the degradation of MgO thin films, and therefore offer important guidelines for quality control and improvement of MTJs sensor manufacturing processes.

3.5 References

Ali, A. M., and Al-Mowali, A. H. (2013). Ceramic expansion by water layers on magnesium oxide: AB Initio Study, **Am. J. Mater. Sci.** 1: 50-53.

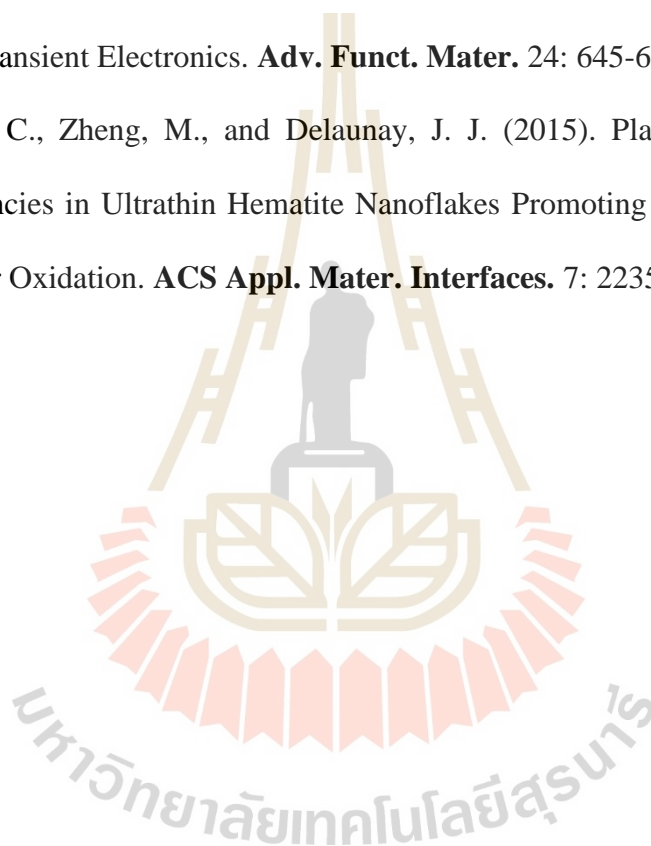
- Amaral, L. F., Oliveira, I. R., Salomao, R., Frollini, E., and Pandolfelli, V. C. (2010). Temperature and common ion effect on magnesium oxide (MgO) hydration. **Ceram. Int.** 36: 1047.
- Amaral, L. F., Oliveira, I. R., Bonadia, P., Salomao, R., and Pandolfelli, V. C. (2011). Chelants to inhibit magnesia (MgO) hydration. **Ceram. Int.** 37: 1537-1542.
- Barrio, L. C., and Vargas, G. (2012). **Handbook of instrumental techniques from CCIiTUB: Photoelectron spectroscopy for surface analysis: X-ray and UV excitation.** (n.p.).
- Bharadwaj, H. K., Lee, J. Y., Li, X., Liu, Z., and Keener, T. C. (2013). Dissolution kinetics of magnesium hydroxide for CO₂ separation from coal-fired power plants. **J. Hazard Mater.** 250-251: 292-297.
- Boyd, C. E., Tucker, C. S., Vitiyatun, R. (2011). Interpretation of pH, acidity, and alkalinity in aquaculture and fisheries. **N. Am. J. Aquac.** 73: 403-408.
- Boyd, C. E. (2015). **Water Quality: An Introduction** (2nd ed.). Switzerland: Springer International.
- Bukhtiyarov, V. I., Nizovskii, A. I., Bluhm, H., Hävecker, M., Kleimenov, E., and Knop-Gericke, A. (2006). Combined in-situ XPS and PTRMS Study of Ethylene Epoxidation over Silver. **J. Catal.** 238: 260-269.
- Denisenko, A., Romanyuk, A., Pietzka, C., Scharpf, J., and Kohn, E. (2010). Surface damages in diamond by Ar/O₂ plasma and their effect on the electrical and electrochemical characteristics of boron-doped layers. **J. Appl. Phys.** 108: 074901.
- Dillip, G. R., Banerjee, A. N., Anitha, V. C., Raju, B. D. P., Joo, S. W., and Min, B. K. (2016). Oxygen Vacancy-Induced Structural, Optical, and Enhanced

- Supercapacitive Performance of Zinc Oxide Anchored Graphitic Carbon Nanofiber Hybrid Electrodes. **ACS Appl. Mater. Interfaces** 8 (7): 5025-5039.
- Dobrzanski, L. Bamberger, A. M., and Totten, G. E. (2020). **Magnesium and Its Alloys: Technology and Applications**. Florida: CRC Press Taylor & Francis Group.
- Febvrier, A. L., Jensen, J., and Eklund, P. (2017). Wet-cleaning of MgO(001): Modification of surface chemistry and effects on thin film growth investigated by x-ray photoelectron spectroscopy and time-of-flight secondary ion mass spectroscopy. **J. Vac. Sci. Technol. A**. 35(2): 021407.
- Fedorockova, A., and Raschman, P. (2008). Effects of pH and acid anions on the dissolution kinetics of MgO. **Chem. Eng. J.** 143: 265-272.
- Fotea, C., Callaway, J., and Alexander, M. R. (2006). Characterisation of the surface chemistry of magnesium exposed to the ambient atmosphere. **Surf. Interface Anal.** 38: 1363-1371.
- Frederick, J. E. (2008). **Principles of atmospheric science**. Boston: Jones and Barlett.
- Gevantman, L. H. (2003). **Solubility of Selected Gases in Water**. Amsterdam: Elsevier Science B.V.
- Hacquart, R., and Jupille, J. (2007). Hydrated MgO smoke crystals from cubes to octahedral. **Chem. Phys. Lett.** 439: 91-94.
- Hanlon, J. M., Diaz, L. B., Balducci, G., Stobbs, B. A., Bielewski, M., and Chung, P. (2015). Rapid surfactant-free synthesis of Mg(OH)₂ nanoplates and pseudomorphic dehydration to MgO. **Cryst. Eng. Comm.** 17: 5672-5679.
- Heide, P. V. D. (2012). **X-Ray Photoelectron Spectroscopy: An Introduction to Principles and Practices**. New Jersey John Wiley & Sons.

- Knoche, W. (1980). Chemical Reactions of CO₂ in Water. In Bauer, C., Gros, G., and Bartels, H. (eds.). **Biophysics and Physiology of Carbon Dioxide, Proceedings in Life Sciences**. (pp. 3-11). Berlin: Springer.
- Kosenko, N. F., Vinogradova, L. A., and Smirnova, M. A. (2008). Effect of Mechanical Processing on the Dissolution Rate of MgO. **Inorg. Mater.** 44: 842-845.
- Kuenzel, C., Zhang, F., Ferrandiz-Mas, V., Cheeseman, C. R., and Gartner, E. M. (2018). The mechanism of hydration of MgO-hydromagnesite blends. **Cem. Concr. Res.** 103: 123-129.
- Laporte, S., Finocchi, F., Paulatto, L., Blanchard, M., Balan, E., and Guyota, F. (2015). Strong electric fields at a prototypical oxide/water interface probed by ab initio molecular dynamics: MgO(001). **Phys. Chem. Chem. Phys.** 17: 20382-20390.
- Lu, H. L., Ding, S. J., and Zhang, D. W. (2010). Investigation of Thermal Stability of Atomic-Layer-Deposited MgO Thin Films on Si (100) Using X-Ray Photoelectron Spectroscopy. **Electrochem. Solid State Lett.** 13: G25-G28.
- Nagamine, Y., H. Maehara, K. Tsunekawa, D. D. Djayaprawira, N. Watanabe, Ultralow resistance-area product of 0.4 Ω(μm)² and high magnetoresistance above 50% in CoFeB/MgO/CoFeB magnetic tunnel junctions, **Appl. Phys. Lett.** 89 (2006) 162507.
- Newberg, J. T., Starr, D. E., Yamamoto, S., Kaya, S., Kendelewicz, T., and Mysak, E. R. (2011). Formation of hydroxyl and water layers on MgO films studied with ambient pressure XPS. **Surf. Sci.** 605: 89-94.
- Oswald, S., Thoss, F., Zier, M., Hoffmann, M., Jaumann, T., and Herklotz, M. (2018). Binding energy referencing for XPS in alkali metal-based battery materials research (II): Application to complex composite electrodes. **Batteries.** 4: 36.

- Parra, E. R., Arango, P. J. A., and Palacio, V. J. B. (2010). XPS structure analysis of TiN/TiC bilayers produced by pulsed vacuum arc discharge. **Dyna-Colombia** 77: 64-74.
- Polyanin, A. D., and Manzhurov, A. V. (2007). **Handbook of Mathematics for Engineers and Scientists**. Norway: Taylor & Francis Group.
- Ridier, K., Aureau, D., Bérini, B., Dumont, Y., Keller, N., and Vigneron, J. (2016). Enhanced Depth Profiling of Perovskite Oxide: Low Defect Levels Induced in SrTiO₃ by Argon Cluster Sputtering. **J. Phys. Chem. C**. 120: 21358-21363.
- Rocha, S. D. F., Mansur, M. B., and Ciminelli, V. S. T. (2004). Kinetics and mechanistic analysis of caustic magnesia hydration. **J. Chem. Technol. Biotechnol.** 79: 816-821.
- Santamaria, M., Di Quarto, F., Zanna, S., and Marcus, P. (2007). Initial surface film on magnesium metal: A characterization by X-ray photoelectron spectroscopy (XPS) and photocurrent spectroscopy (PCS). **Electrochim. Acta**. 53: 1314-1324.
- Sarker, S. D., and Nahar, L. (2007). **Chemistry for pharmacy students: general, organic and natural product chemistry**. England: John Wiley & Sons.
- Simpson, D. J., Bredow, T., Smart, R. St. C., and Gerson, A. R. (2002). Mechanisms of acidic dissolution at the MgO (100) surface. **Surf. Sci.** 516: 134-146.
- Singh, B. B., Agrawal, V. A., Joshi, G., and Chaudhary, S. (2012). X-ray photoelectron spectroscopy and conducting atomic force microscopy investigations on dual ion beam sputtered MgO ultrathin films. **Thin Solid Films**. 520: 6734-6739.
- Starr, C., Evers, C. A., and Starr, L. (2011). **Biology: Concepts and Applications, eight ed., Brooks/Cole**. California: Cengage Learning.

- Taheri, M., Danaie, M., and Kish, J. R. (2014). TEM examination of the film formed on corroding Mg prior to breakdown. **J. Electrochem. Soc.** 161: C89-C94.
- Ulvac-PHI. (2012). OPERATOR'S PHI MultiPak (version 9) [software manual] Japan.
- Yao, H. B., Li, Y., and Wee, A. T. S. (2000). An XPS investigation of the oxidation/corrosion of melt-spun Mg. **Appl. Surf. Sci.** 158: 112-119.
- Yin, L., Cheng, H., Mao, S., Haasch, R., Liu, Y., and Xie, X. (2014). Dissolvable Metals for Transient Electronics. **Adv. Funct. Mater.** 24: 645-658.
- Zhu, C., Li, C., Zheng, M., and Delaunay, J. J. (2015). Plasma-Induced Oxygen Vacancies in Ultrathin Hematite Nanoflakes Promoting Photoelectrochemical Water Oxidation. **ACS Appl. Mater. Interfaces.** 7: 22355-22363.



CHAPTER IV

EFFECT OF WATER TEMPERATURE ON THE DISSOLUTION BEHAVIOR OF MAGNESIUM OXIDE THIN FILM

4.1 Introduction

In previous chapter, the influence of the gas atmosphere on the dissolution in water of the MgO thin film was investigated. It is found that the gas atmosphere could play a crucial role in the dissolution behavior of the MgO thin film. Besides the effect of gas atmosphere, the temperature of the water also has influence on the dissolution behavior. To broaden our knowledge of the dissolution of MgO thin film, in this chapter, the effect of temperature on dissolution behavior of the MgO thin film is investigated.

Temperature of water is one of the most significant environmental factors that strongly influences the water chemistry and thus it plays a central role in many processes including biological activity, corrosion, hydration, dissolution and other chemical reactions (Wanders, 2019; Wedemeyer, 2007;). Many studies reported that an increase of water temperature could increase rate of chemical reactions. Zhang, Li, and Wang (2019) studied the effect of temperature on the water wettability of the MgO substrate. They found that an increase of temperature could lead to the increase of kinetic energy. This results in an increase of wettability of the MgO substrate. In addition, Fedorockova and Raschman (2008) investigated the dissolution of MgO in acid under temperatures varies from 25°C to 60°C. They observed that the dissolution

of the MgO increases with an increase of temperature. Although many researchers reported the influence of the temperature on the dissolution of MgO, to the best of our knowledge, the detail of dissolution of MgO thin film under various temperatures is still unclear. In order to obtain an understanding of the dissolution behavior in the wide range of temperatures, therefore, in this study, the MgO thin film is exposed to water at different temperatures including 0, 10, 20, 25, 50 and 75°C. Then, the characterization techniques, including scanning electron microscope (SEM), and X-ray photoelectron spectroscopy (XPS), are used to quantify the morphology, thickness and the depth profiling of the film.

This chapter is organized as follows: Section 4.2 describes the experimental procedure used in this study. Section 4.3 demonstrates the result of the surface morphology, the remaining thickness of the film, the depth profiling of the film and the influence of different water temperatures on dissolution mechanism of the films as well as the discussion. In final, section 4.4 shows the conclusion of this chapter.

4.2 Experimental Procedure

4.2.1 Sample Preparation

The dissolution behavior of the MgO thin film was investigated under different temperatures as exhibited in Figure 4.1. The commercial epitaxial MgO (001) thin films (obtained from Western Digital (Fremont), LLC, Fremont, CA, US) with 20 nm thickness on the Si substrate from the same production lot were cut into 1×1 cm² square shape using a diamond scribe. A 1 ml of droplets of the deionized water with six different temperatures (0, 10, 20, 25, 50, and 75°C) was dropped on the top of the film surfaces for 5 minutes. After that, the droplet of deionized water was removed from

the film surfaces by N₂ blower. The samples are denoted as MgO-0, MgO-10, MgO-20, MgO-25, MgO-50, and MgO-75 representing water temperatures.

4.2.2 Characterizations

4.2.2.1 X-ray Photoelectron Spectroscopy (XPS)

In this experiment, the remaining thickness of the film after dissolution is approximately a few nanometers; therefore, XPS depth profile measurement method is applied to determine the remaining thickness because of its high surface-sensitive analytical capability which is suitable for extra thin films. The integration of XPS (the PHI 500 Versaprobe-II) and *in situ* Ar⁺ ion bombardment was used to examine the remaining thickness and the depth distribution of the chemical composition of the films. X-ray source of this instrument is a monochromatic Al-K_α which provides photon with 1486.6 eV. The *in situ* Ar⁺ ion bombardment with 1 keV energy and a beam size of 2 × 2 mm² were proceeded using an ion gun in the analysis chamber. All spectra (Mg 2*p*, O 1*s*, C 1*s*, Si 2*p*) were collected using the same pass energy of 23.5 eV except the O 1*s* spectra of MgO-25, MgO-50 and MgO-75 which were collected at 11.75 eV of pass energy. Corrections of the energy shift due to the steady-state charging effect of the samples were carried out by reference to the Ar 2*p* spectra at 243 eV (Bukhtiyarov, 2006; Denisenko, 2010; Oswald, 2018). The atomic concentrations were calculated from the C 1*s*, O 1*s*, Mg 2*p* and Si 2*p* photoelectron peak intensity using Shirley background subtraction and sensitivity factors provided by the OPERATOR'S PHI MultiPak™ Software Manual (2012).

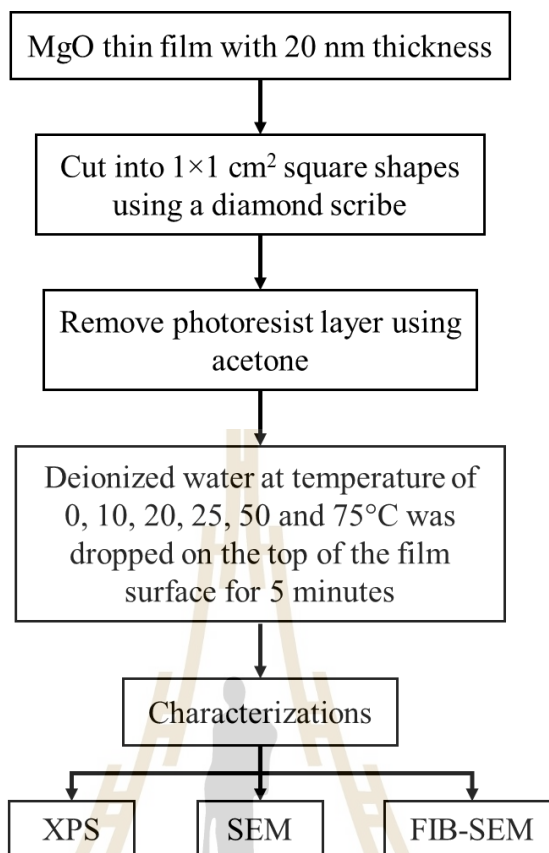


Figure 4.1 Schematic diagram of the experimental procedure of the study of dissolution behavior of the MgO thin film under different temperatures.

4.2.2.2 Scanning Electron Microscope (SEM)

The scanning electron microscope (SEM) was used to evaluate the change in surface morphology and thickness of the MgO thin film samples. All SEM measurements were done using Scanning electron microscope equipped with Focused ion beam (FIB-SEM: Carl Zeiss AURIGA® CrossBeam® Workstation). To prevent static electric charge and beam damage during the irradiation of electron, all samples were sputter-coated with 1 nm thickness of gold using Leica/EM ACE601. For

the thickness measurement, the cross-section of the film was prepared by using Ga⁺ (ion) milling. Then, the cross-section was photographed at a take-off angle of 52° using SEM.

4.3 Results and Discussion

4.3.1 Surface Morphology

The microstructure of the MgO thin film surfaces after being exposed to different water temperatures are carried out by scanning electron microscope (SEM) as shown in Figure 4.2 which illustrates the change of morphology of the dissolved areas and vicinities.

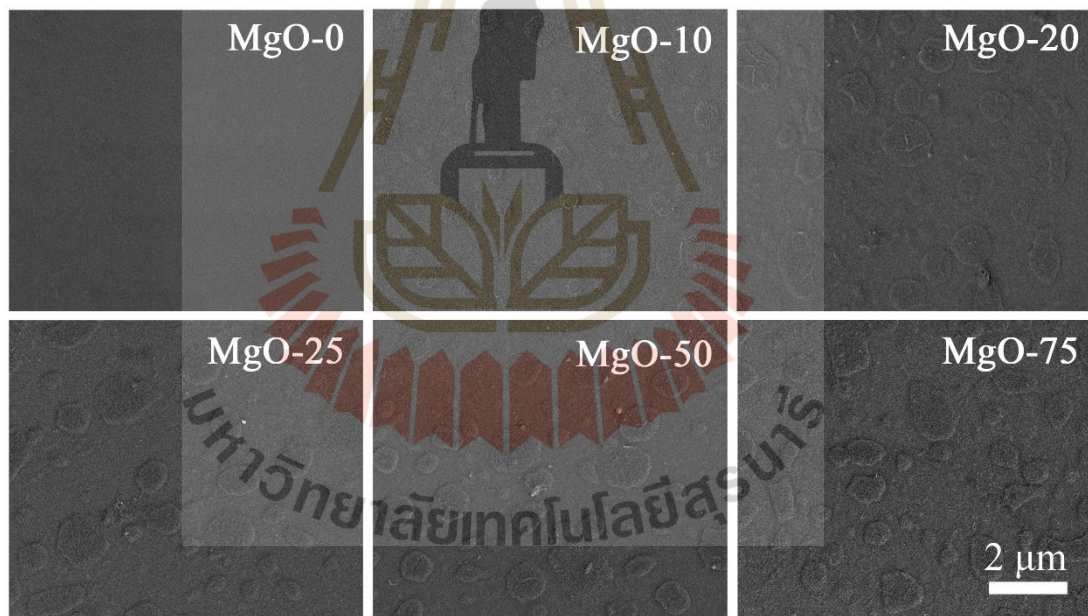


Figure 4.2 The SEM image of the MgO thin film morphology after exposed to deionized water. (Magnification: $\times 5000$)

It is found that the clusters of new layers form over the surfaces in every condition. Significantly, the number of clusters of new layers take place and increase

with increasing water temperature. These new layers could be caused by the chemical reaction between the deionized water and MgO film. Moreover, the reaction could also be accelerated by the temperature of the water. Influence of water temperature on dissolution behavior is indicated by the remaining thickness of the film after being exposed by the water.

4.3.2 Remaining Thickness of the Films

A plot of the atomic concentration percentage of elements as a function of sputtering time of the fresh MgO thin film and the films after dissolution are exhibited in Figure 4.3 and Figure 4.4, respectively. As mentioned above, the O *1s* spectra of the MgO-25, MgO-50 and MgO-75 were collected using 11.75 eV of pass energy. Using lower pass energy is result in the lower O *1s* atomic concentration. However, it does not affect the variation of the film depth profile. From Figure 4.3, the depth profile of the pristine sample shows that the C *1s* signal due to the natural contamination is detected on the top of the film surfaces. After the first sputtering cycle of *in situ* Ar⁺ ion, the carbon contamination is removed and the concentration of the Mg *2p* and O *1s* are continuously constant at 50% of the atomic concentration. Then, after being sputtered deeper into the film, the Mg *2p* and O *1s* concentrations start decreasing meanwhile the signal of Si *2p* increases. The intersection point between the Mg *2p* and Si *2p* lines may indicate the interface region between MgO thin film and Si substrate after sputtering through the film. The variation of atomic concentration as a function of the sputtering time elucidates the changes of the film chemical composition along the depth. Moreover, it can be used to investigate the thickness of the film.

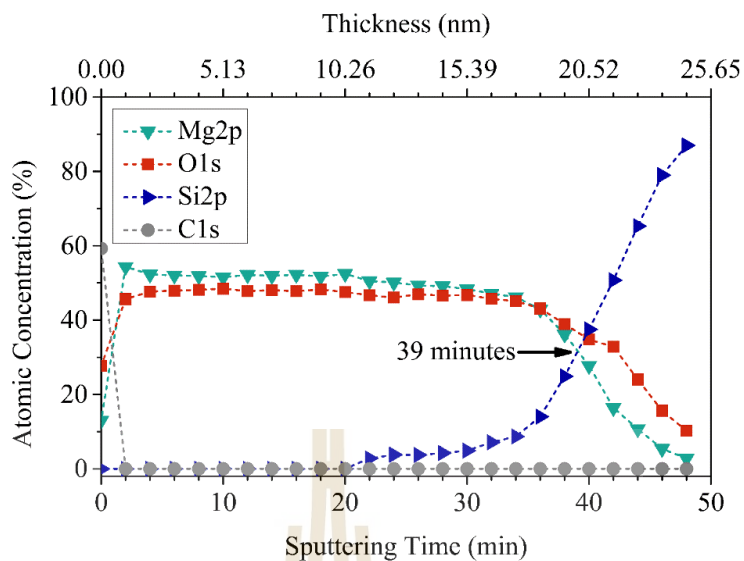


Figure 4.3 The XPS depth profile of the 20 nm MgO thin film. The black arrow indicates the reference point of the remaining thickness.

By employing the depth profile measurement shown in Figure 4.3, the intersection of the Si $2p$ line and the Mg $2p$ line is used as the reference point (at 39 min, indicated by the black arrows) to determine the remaining thickness of the films by comparing with the sputtering rate of the fresh MgO thin film, which is approximately 0.513 nm/min (i.e. sputtering rate = thickness of the film/sputtering time). When considering all dissolution conditions as shown in Figure 4.4, the XPS results reveal the effect of temperature on the reduction of the film thickness. The thickness decreases with the increase of water temperature. This is because the dissolution rate of the MgO thin films strongly depends on the water temperature. These results are in agreement with the previous work reported by Bharadwaj *et al.* (2013), who demonstrated that the dissolution rate dramatically increased with increasing temperature. Furthermore, M. Komiyama *et al.* (1997), also pointed out that the MgO

can be hardly dissolved in a cold water. These could be the reasons why the remaining thickness of the MgO-0 sample is thicker than that of the MgO-75 sample.

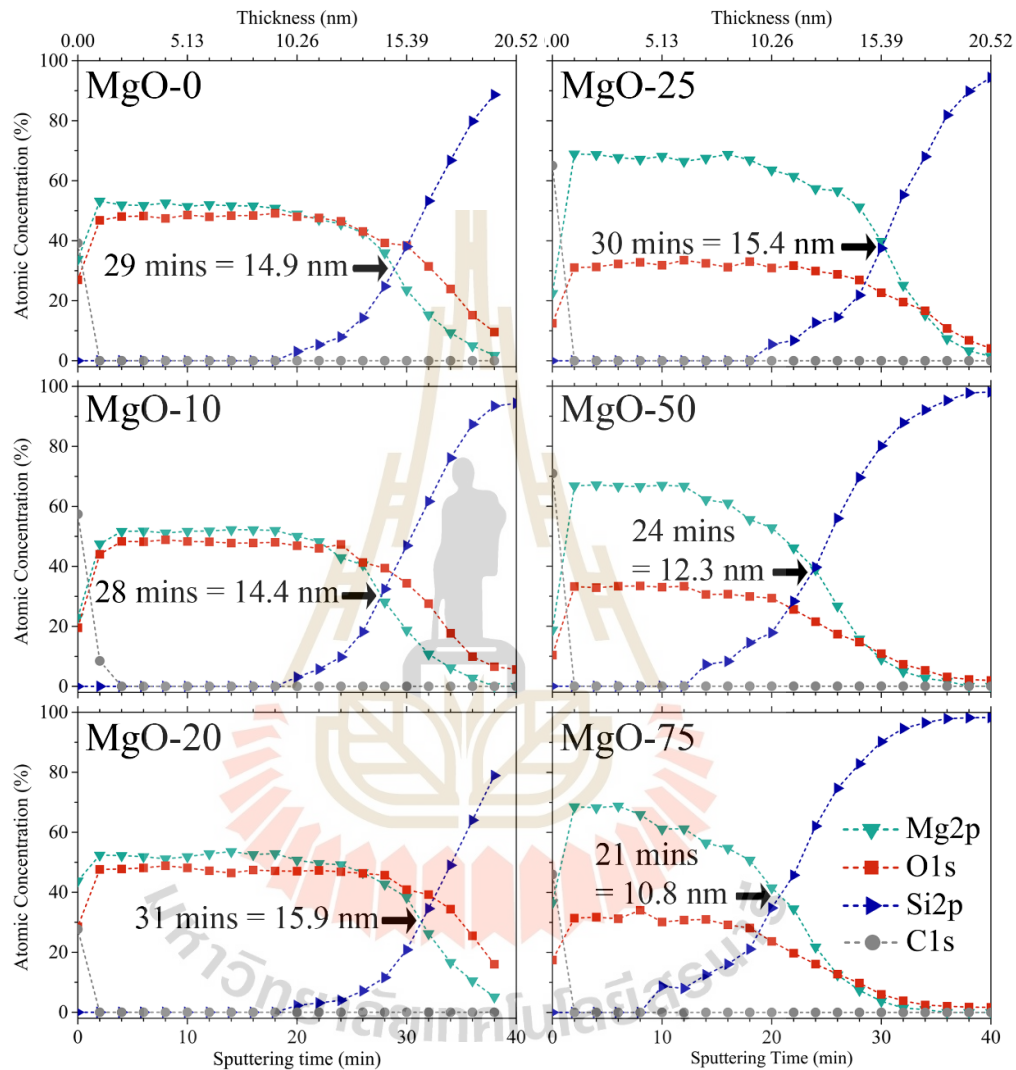


Figure 4.4 A plot of atomic concentration percentage as a function of sputtering time of the MgO thin films after dissolution in deionized water.

To verify the remaining thickness of the MgO thin film after being exposed to deionized water, the cross-section of the film was investigated by using FIB-SEM. The FIB-SEM cross-sectional images are illustrated in Figure 4.5. The different

contrast in the images is referred to the different morphologies of the film and substrate. The darker area represents the substrate region while the brighter area is the film region. The results show that the film thickness decreases with the increase of the water temperature exposed. This is in a line with the XPS depth profile results, as discussed above.

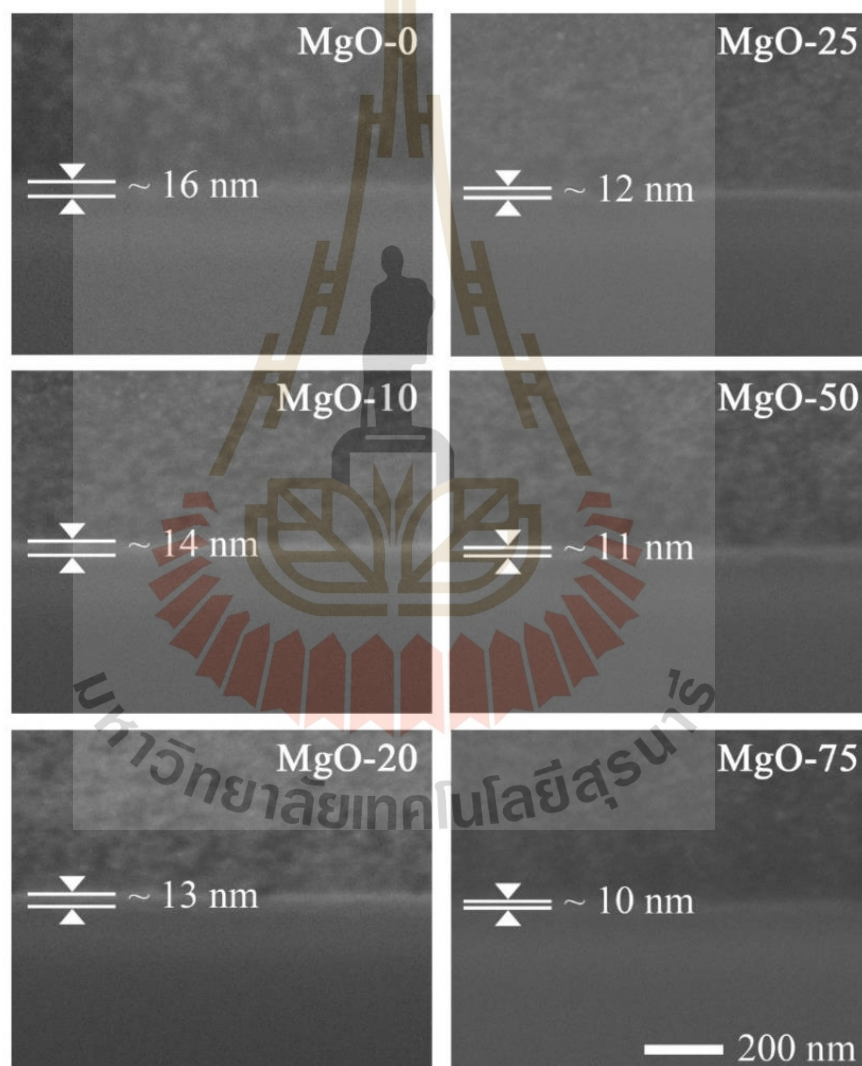


Figure 4.5 The FIB-SEM cross-sectional of the MgO thin film at different water temperatures. (Magnification: $\times 100K$)

4.3.3 Depth Profiling of the Films

To identify the chemical state of elements on the films after dissolution, the XPS spectra of all elements are recorded and deconvoluted with a combination of Gaussian (70%) and Lorentzian (30%) fits. The deconvoluted high-resolution O1s core level spectrum of the representative sample (MgO-0, MgO-25 and MgO-75) at the selected sputtering time (0, 2, 10, 20 and 30 min of sputtering time) are demonstrated in Figure 4.6.

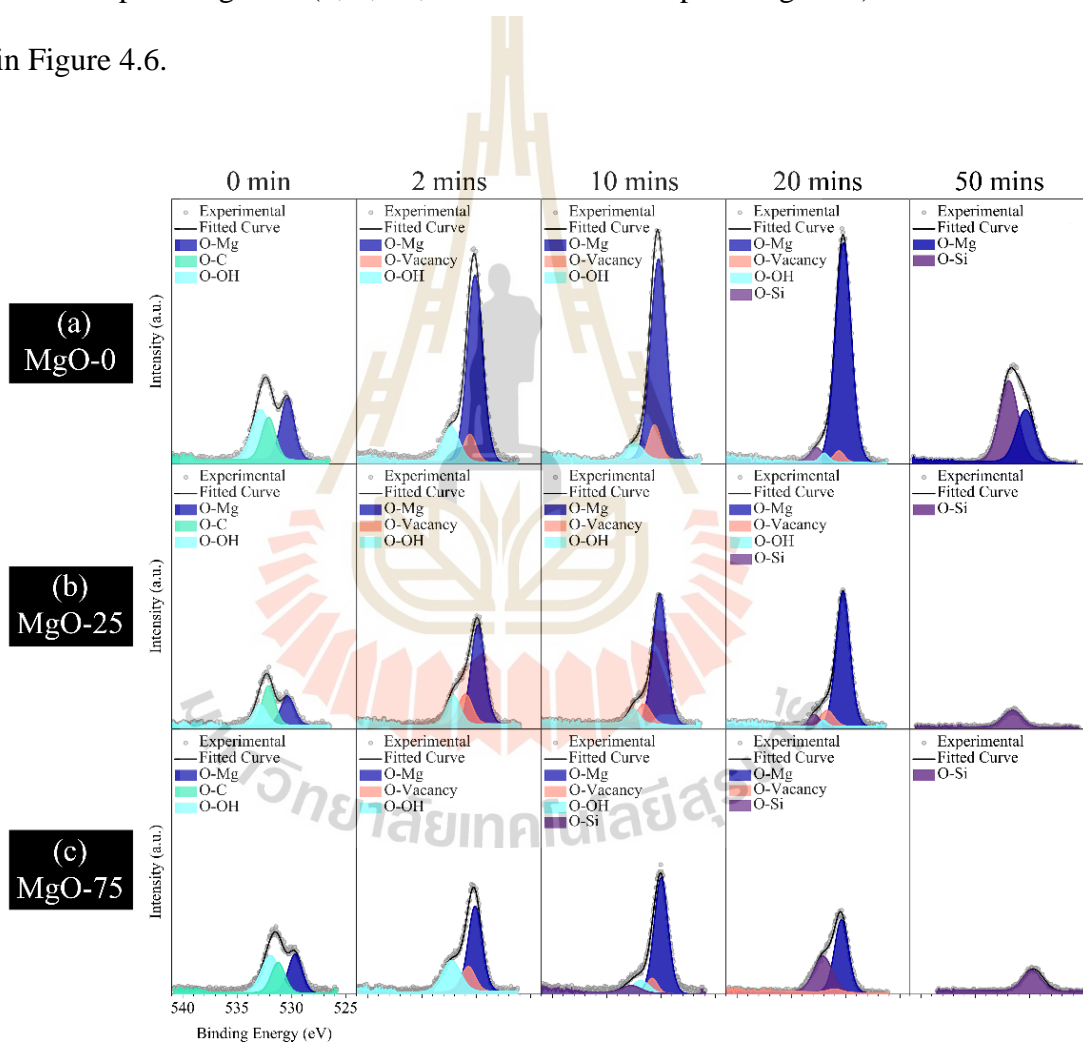


Figure 4.6 The deconvoluted O 1s spectra of (a) MgO-0 (b) MgO-25 and (c) MgO-75 at different selected sputtering time.

The intensity of O 1s spectra of MgO-25 and MgO-75 are lower than those of MgO-0 because the lower pass energy was used. Before the bombardment of Ar⁺ ion, the O1s spectra are deconvoluted into three subpeaks at the binding energy of 530.3, 532.1, 532.8 eV which correspond to the binding energy of O–Mg, O–C and O–OH, respectively (Dillip, 2016; Rocha, 2004; Yin, 2014; Zhu, 2015). The presence of the OH group represented by O–OH peak in the deconvoluted O 1s spectra, as shown in Figure 4.6. This confirms that the film reacts with the deionized water and creates the Mg(OH)₂ layer over their surface. This result corresponds to the formation of the new layer over the film surface observed by the SEM, as shown in Figure 4.2.

After 2 min of sputtering, the peak position shifts 0.1–0.2 eV to the lower binding energy while the O–C subpeak is eliminated and the intensity of the O–Mg subpeak dramatically increases. At the same time, O-vacancy identified as the oxygen deficiency takes place at 530.6 eV (Ridier, 2016; Zhu, 2015) of the binding energy and decreases with the sputtering time. The oxygen deficiency could be caused by the *in situ* Ar⁺ ion sputtering that removes the oxygen atom from the lattice MgO. Then, after sputtering to the further depth, the O–Si subpeak appears at the binding energy of 533 eV (Lu, 2010) meanwhile the intensity of another subpeak start decreasing.

To quantify the amount of the Mg(OH)₂ which forms over the film surface, the maximum intensity of O–OH subpeak of all sample is converted to the percent of atomic concentration and established in Figure 4.7. The results suggest that the O–OH concentrations continuously decrease with increasing sputtering time. This implies that the Mg(OH)₂ permeates into the deeper layer of the film. Significantly, the amount of Mg(OH)₂ in the films increases with the water temperature.

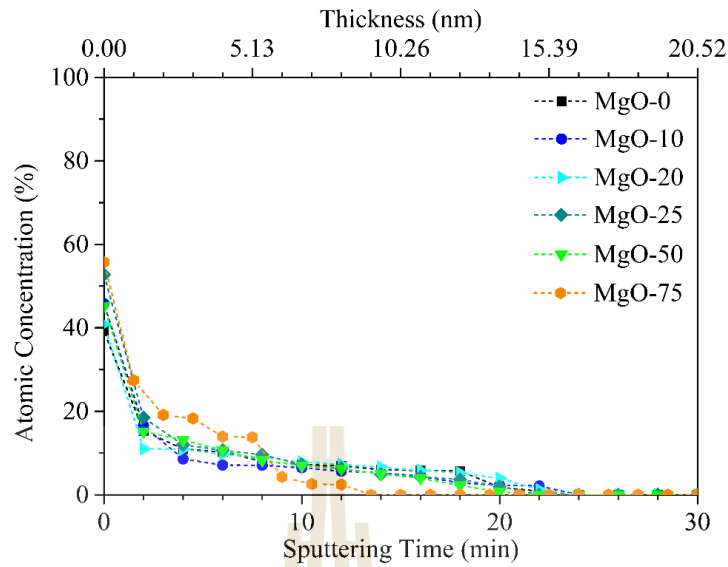


Figure 4.7 A plot of the atomic concentration of Mg(OH)₂ of all samples.

4.3.4 Dissolution Mechanism of the MgO Thin Films

To understand the effect of the temperature on the dissolution behavior of the film, a schematic drawing of the dissolution mechanism of the MgO thin film is illustrated in Figure 4.8. After the films are exposed to the deionized water, the water molecules are rapidly absorbed on the film surface and infiltrate into the deeper layer of the film. Then, the chemical composition of the film which reacted with water is transforming into the Mg(OH)₂ (as confirmed by the XPS results). This can be expressed as the Equation (4.1) (Dobrzanski, 2020; Hanlon, 2015):



Subsequently, the hydroxide layer is partially releasing OH⁻ ions into the deionized water and creating MgOH⁺ on the film surface expressed as the Equation

(4.2) (Amaral, 2010, Amaral, 2011; Hanlon, 2015). This is evidenced by a change of the film morphology as manifested in the SEM micrographs (Figure 4.2).

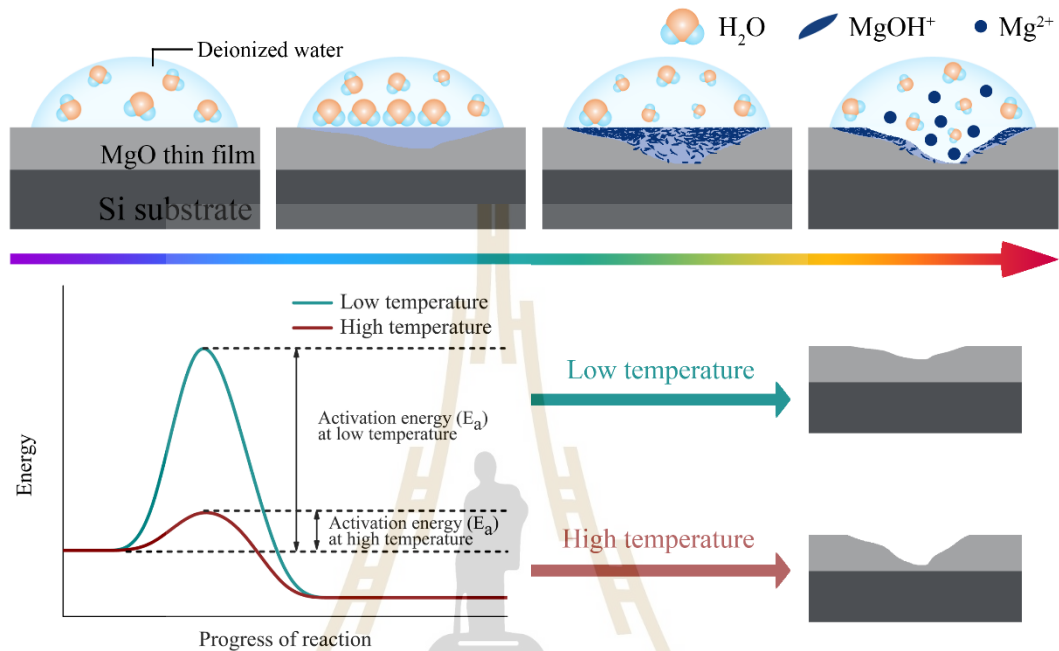
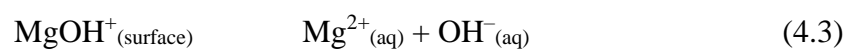
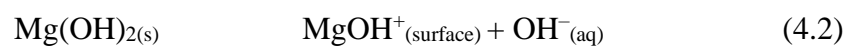


Figure 4.8 The dissolution model of the MgO thin film after being exposed to deionized water.

The Mg^{2+} and OH^- are continuously released from the film surface. Consequently, the morphology, thickness, and chemical composition are finally changed. At the higher temperature, the required activation energy is less than that of the lower temperature as illustrated in Figure 4.8(top diagram).



Moreover, the increase of water temperature enhances the kinetic energy of the molecules of water (Zhang, 2019). Therefore, the probability of water molecules interacts with the MgO film is greater in high temperature water. This results in the greater number of Mg(OH)₂ and thinner remaining thickness of MgO film when the film is exposed to the high temperature water.

4.4 Chapter Summary

This study demonstrates effect of water temperature on the degradation behavior of the MgO (001) thin film and the formation of the Mg(OH)₂ on their surface. Qualitative analysis is done by SEM. The micrographs from SEM show the development of new layers on the film surfaces after being exposed to the water. Meanwhile, XPS depth profile results are in agreement with FIB-SEM cross-section results which point out that the MgO thin films are dissolved in deionized water while the dissolution of the films strongly depends on the water temperature. Furthermore, the quantitative analysis is conducted by XPS which indicates the bonding between metallic Mg and hydroxide -OH in the deconvoluted O 1s spectra. The XPS spectra reflect the amount of the Mg(OH)₂ concentration on the film surface. This result elucidates that after being exposed to the deionized water, the films absorb deionized water and form Mg(OH)₂. This effect is more pronounced in case of the higher temperature. In addition, the information obtained from this investigation provides the basic understanding of surface science as well as valuable knowledge for the further development and modification which could be a guideline for the industrial processing especially the spintronic device manufacturing.

4.5 References

- Amaral, L. F., Oliveira, I. R., Salomao, R., Frollini, E., and Pandolfelli, V. C. (2010). Temperature and common ion effect on magnesium oxide (MgO) hydration. **Ceram. Int.** 36: 1047.
- Amaral, L. F., Oliveira, I. R., Bonadia, P., Salomao, R., and Pandolfelli, V. C. (2011). Chelants to inhibit magnesia (MgO) hydration. **Ceram. Int.** 37: 1537-1542.
- Bharadwaj, H. K., Lee, J. Y., Li, X., Liu, Z., and Keener, T. C. (2013). Dissolution kinetics of magnesium hydroxide for CO₂ separation from coal-fired power plants. **J. Hazard. Mater.** 250-251: 292-297.
- Bukhtiyarov, V. I., Nizovskii, A. I., Bluhm, H., Hävecker, M., Kleimenov, E., and Knop-Gericke, A. (2006). Combined in-situ XPS and PTRMS Study of Ethylene Epoxidation over Silver. **J. Catal.** 238: 260-269.
- Denisenko, A., Romanyuk, A., Pietzka, C., Scharpf, J., and Kohn, E. (2010). Surface damages in diamond by Ar/O₂ plasma and their effect on the electrical and electrochemical characteristics of boron-doped layers. **J. Appl. Phys.** 108: 074901.
- Dillip, G. R., Banerjee, A. N., Anitha, V. C., Raju, B. D. P., Joo, S. W., and Min, B. K. (2016). Oxygen Vacancy-Induced Structural, Optical, and Enhanced Supercapacitive Performance of Zinc Oxide Anchored Graphitic Carbon Nanofiber Hybrid Electrodes. **ACS Appl. Mater. Interfaces** 8 (7): 5025-5039.
- Dobrzanski, L., Bamberger, A. M., and Totten, G. E. (2020). **Magnesium and Its Alloys: Technology and Applications**. Florida: CRC Press Taylor & Francis Group.
- Fedorockova, A., and Raschman, P. (2008). Effects of pH acid anions on the dissolution kinetics of MgO. **Chem. Eng. J.** 143: 265-272.

- Hanlon, J. M., Diaz, L. B., Balducci, G., Stobbs, B. A., Bielewski, M., and Chung, P. (2015). Rapid surfactant-free synthesis of Mg(OH)₂ nanoplates and pseudomorphic dehydration to MgO. **Cryst. Eng. Comm.** 17: 5672-5679.
- Ji, L., and Yu, H. (2018). Carbon dioxide sequestration by direct mineralization of fly ash. In Pacheco-Torgal, F., Shi, C., and Sanchez, A. P. (ed.). **Carbon Dioxide Sequestration in Cementitious Construction Materials** (pp. 13-37). United Kingdom: Woodhead Publishing.
- Komiyama, M., and Gu, M. (1997). Atomic force microscopy images of MgO(100) and TiO₂(110) under water and aqueous aromatic molecule solutions. **Appl. Surf. Sci.** 120: 125-128.
- Lu, H. L., Ding, S. J., and Zhang, D. W. (2010). Investigation of Thermal Stability of Atomic-Layer-Deposited MgO Thin Films on Si (100) Using X-Ray Photoelectron Spectroscopy. **Electrochem. Solid State Lett.** 13: G25-G28.
- Oswald, S., Thoss, F., Zier, M., Hoffmann, M., Jaumann, T., and Herklotz, M. (2018). Binding energy referencing for XPS in alkali metal-based battery materials research (II): Application to complex composite electrodes. **Batteries.** 4: 36.
- Ridier, K., Aureau, D., Bérini, B., Dumont, Y., Keller, N., and Vigneron, J. (2016). Enhanced Depth Profiling of Perovskite Oxide: Low Defect Levels Induced in SrTiO₃ by Argon Cluster Sputtering. **J. Phys. Chem. C.** 120: 21358-21363.
- Rocha, S. D. F., Mansur, M. B., and Ciminelli, V. S. T. (2004). Kinetics and mechanistic analysis of caustic magnesia hydration. **J. Chem. Technol. Biotechnol.** 79: 816-821.
- Ulvac-PHI. (2012). OPERATOR'S PHI MultiPak (version 9) [software manual] Japan.

- Wanders, N., Vliet, M. T. H. van., Wada, Y., Bierkens, M. F. P., and Beek, L. P. H. (Rens) van. (2019). High-Resolution Global Water Temperature Modeling. *Water Resour. Res.* 55(4): 2760-2778.
- Wedemeyer, Gary A. (2007). Chapter 12 - Transportation and Handling. In Pennell, W., and Barton, B. A. (ed.). **Developments in Aquaculture and Fisheries Science** (pp. 727-758). Netherland: Elsevier Science B.V.
- Yin, L., Cheng, H., Mao, S., Haasch, R., Liu, Y., and Xie, X. (2014). Dissolvable Metals for Transient Electronics. **Adv. Funct. Mater.** 24: 645-658.
- Zhang, C., Li, X., and Wang, J. (2019). Predicting the Effects of Temperature on the Water Wettability of the Mg/MgO Surface through Atomistic Simulations. **J. Phys. Chem. C.** 123(31): 18914-18923.
- Zhu, C., Li, C., Zheng, M., and Delaunay, J. J. (2015). Plasma-Induced Oxygen Vacancies in Ultrathin Hematite Nanoflakes Promoting Photoelectrochemical Water Oxidation. **ACS Appl. Mater. Interfaces.** 7: 22355-22363.

CHAPTER V

ROLE OF TEMPERATURES AND ATMOSPHERES ON THE DEHYDRATION CHARACTERISTIC OF MAGNESIUM OXIDE THIN FILM

5.1 Introduction

In Chapter 3 and 4, we reported dissolution reaction of the film. Such a reaction could degrade electrical and mechanical properties. On the other hand, in this chapter, we investigated the dehydration reaction of the MgO film. The dehydration reaction is the mechanism of water removal from the molecules of materials. It most often involves the thermal decomposition (Stanish and Perlmutter, 1983). Many studies suggested that dehydration reaction could induce the decrease of the hydroxide layer which formed over the hydrated MgO thin film resulting in the improvement of the film properties (Gay and Harrison, 2005; Moon 2007). Theoretically, $\text{Mg}(\text{OH})_2$ dehydrates and transforms to MgO after it was calcined at temperature 350°C as described in Equation (5.1) (Kurosawa, 2019; L'vov, 1998).



In practice, the temperature which is suitable for dehydration of the hydrated MgO thin film depends on several factors including forms of MgO, purity and amount of $\text{Mg}(\text{OH})_2$ as well as the environment during the annealing process (Hill, 2004; Oka,

1988; Yim, 2018,). Therefore, understanding the impact of these factors on the dehydration behavior of the MgO thin film is important. In this chapter, the role of annealing temperatures and annealing atmosphere on the dehydration behavior of the MgO thin film is studied. The MgO thin film is exposed to humid environment for 24 hours. Then, the hydrated-MgO thin films were annealed at 250, 300, 350 and 400°C in different annealing atmosphere including air, nitrogen gas (N₂) and argon gas (Ar). The atomic force microscope (AFM) was used to study the surface topography of the film. The thickness of the MgO thin film was quantified by using x-ray reflectivity (XRR) and transmission electron microscope (TEM). In addition, the electronic structure of the MgO thin film was determined by the x-ray absorption spectroscopy (XAS).

This chapter is organized as follows: section 5.2. describes the experimental procedure used to determine the role of environment on the dehydration of MgO thin film. Section 5.3 discusses the results obtained from various analysis techniques including atomic force microscopy (AFM), X-ray reflectometry (XRR), transmission electron microscope (TEM) and X-ray absorption spectroscopy (XAS). Finally, section 5.4 presents conclusion of this chapter.

5.2 Experimental Procedure

5.2.1 Sample Preparation

Figure 5.1 displays the schematic of the experimental procedure of this study. The commercial MgO (001) thin film with 20 nm of thickness on Si substrate was cut into piece of 1×1 cm² square shape using diamond scribe. Acetone was used to remove the photoresist layer covered over the MgO thin film surface. Then, the cleaned surface MgO thin films were exposed to humid environment for 24 hours in a humid

chamber, where the relative humidity (%RH) was controlled at ~80% RH. Hereafter, the MgO thin film exposed to humid environment was referred as “hydrated MgO thin film”.

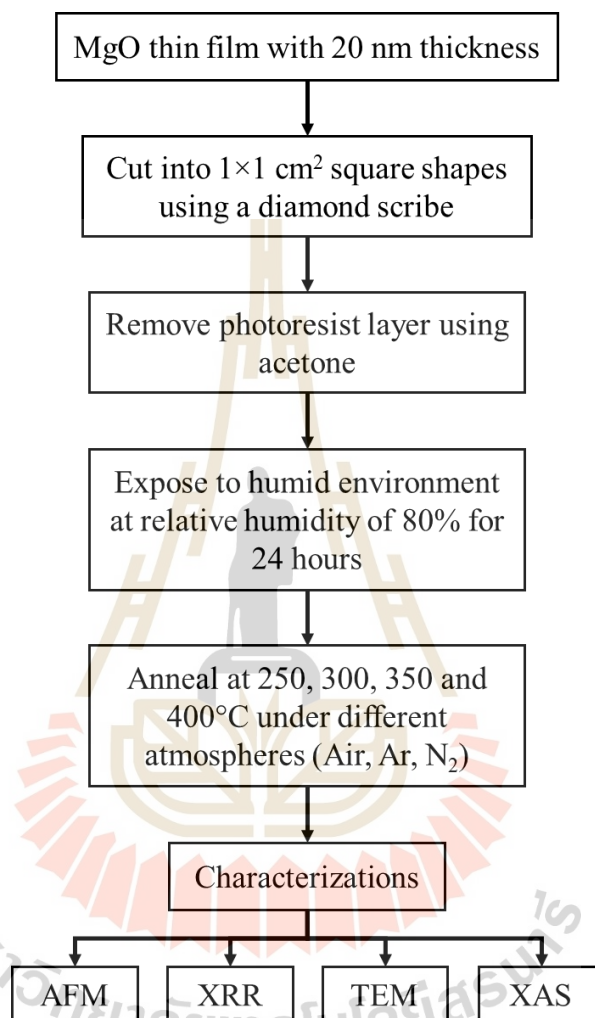


Figure 5.1 Schematic diagram of the experimental procedure of the investigation of role of temperatures and atmospheres on the dehydration characteristic of magnesium oxide thin film.

To investigate the dehydration characteristic of the MgO thin film, the hydrated MgO thin films were annealed at 250, 300, 350 and 400°C for 120 minutes in

air, nitrogen atmosphere (N_2) and argon atmosphere (Ar) using a horizontal tube furnace. The heating and cooling rate used in this study are $5^\circ\text{C}/\text{min}$ following the annealing profile illustrated in Figure 5.2. In case of the annealing in the gas atmosphere, before annealing, the high purity gas (99.9% pure of either nitrogen gas or argon gas) was flowed into the furnace with a flow rate of 600 standard cubic centimeters per minute (sccm) for 30 minutes in order to expel air and other contaminants from the furnace. Then, to maintain the atmosphere within the furnace during the annealing process, the gas was flowed through the tube furnace with the flowing rate of 100 sccm. After the annealing process completed, the dehydrated samples were removed from the furnace. Subsequently, the chemical compositions, thickness and surface roughness of all samples are analyzed.

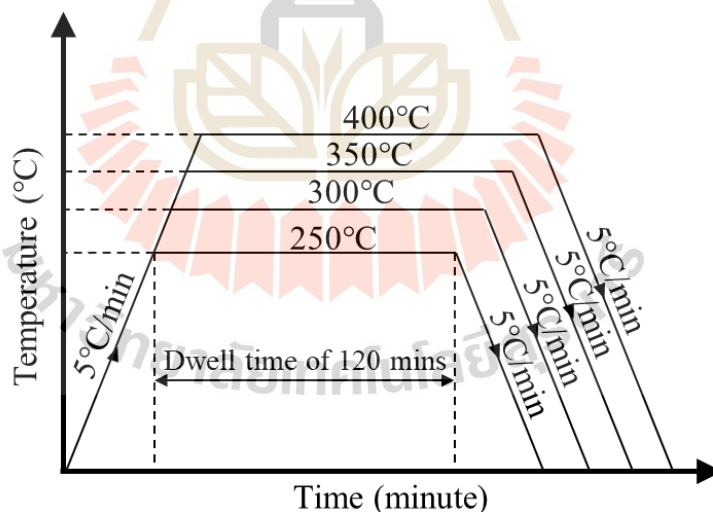


Figure 5.2 The annealing profile of the MgO thin film.

5.2.2 Characterizations

5.2.2.1 Atomic Force Microscopy (AFM)

Atomic force microscopy (AFM) was used to examine the features on the surface of all MgO thin film samples. The MgO thin films were mounted on the metal plate using the super glue. The measurement was performed using the Nanoscope IIIA Multimode SPM, Veeco Instruments operating under the contact mode.

5.2.2.2 X-Ray Reflectivity (XRR)

In order to access the change in thickness of the MgO thin film, the X-ray reflectivity (XRR) was used. The measurements were performed by using MRD (PANalytical) Xpert Materials Research diffractometer. The system voltage of 45 kV with a current of 40 mA was used for this operation. The reflected X-ray intensity was recorded as a function of the X-ray incident angle, θ ranging from 0.1° to 8° .

5.2.2.3 Transmission Electron Microscope (TEM)

Then, the transmission electron microscopy (TEM: Philips CM200) was also used to measure the thickness of the MgO thin film. To prepare the samples for the TEM, the MgO thin films were coated by the platinum strip and were milled to thin specimens (< 100 nm of thickness) by focus Gallium ion beam of the field emission scanning electron microscope (FIB-FESEM: The FEI xT Nova NanoLab 200). Then, the thin specimens were lifted-out by the ex-situ lift-out and were placed on copper (Cu) grids for subsequent TEM analysis.

5.2.2.4 X-ray Absorption Spectroscopy (XAS)

X-ray absorption spectroscopy (XAS) is a powerful analysis technique that gives information on the structure of the materials at the local level. In the XAS, X-ray absorption near edge structure (XANES) is one of the techniques that

can identify the local atomic coordination and electronic structures of the materials. In this study, the XANES measurements were carried out at the BL8: XAS beamline at Synchrotron Light Research Institute (SLRI). The synchrotron white X-ray is generated from a bending magnet with 1.2 GeV of an electron energy and 110-70 mA of an electron beam current. For this measurement, Beryl (1010) crystal was used as a double monochromator. The size of monochromatic X-ray beam on sample was $15 \text{ mm} \times 1 \text{ mm}$. The XANES spectra of the Mg K-edge (1303 eV) were recorded with energy steps of 0.2 eV and a dwell time of 3 sec at room temperature under the fluorescent yield mode by using a 4-element silicon drift detector (4SDD). In order to solve an energy shift, the Mg metal foil were used as a reference for energy calibration with a precision of $\pm 0.2 \text{ eV}$. The pre-edge and post edge background of the XAS spectra was subtracted. All XANES spectra were normalized with height of the edge jump by using ATHENA software package.

5.3 Results and Discussion

5.3.1 Topography of the Film

The AFM images depicting the topography of the pristine MgO thin film and the hydrated MgO thin film are exhibited in Figure 5.3. Results reveal that before the film was exposed to the humid environment, it possesses a smooth surface while the surface roughness is of 0.151 nm. After the hydrated film is kept in the humid box for 24 hours, it is found that the film forms the clusters over its surface resulting in an increase of the surface roughness to 33.97 nm.

Interestingly, these clusters are very similar to the clusters we observed in the SEM image in the Chapter 4. This result is in agreement with work reported by

Lee and Eun (2003); they observed the same clusters during the investigation of the hydration reaction of MgO thin film. They suggested that the hydration induced the formation of hydroxide $\text{Mg}(\text{OH})_2$ and these clusters are the results of the lattice mismatch between the oxide and hydroxide. Therefore, it could be speculated that the clusters over film surface are the $\text{Mg}(\text{OH})_2$, a result of the hydration of the MgO thin film.

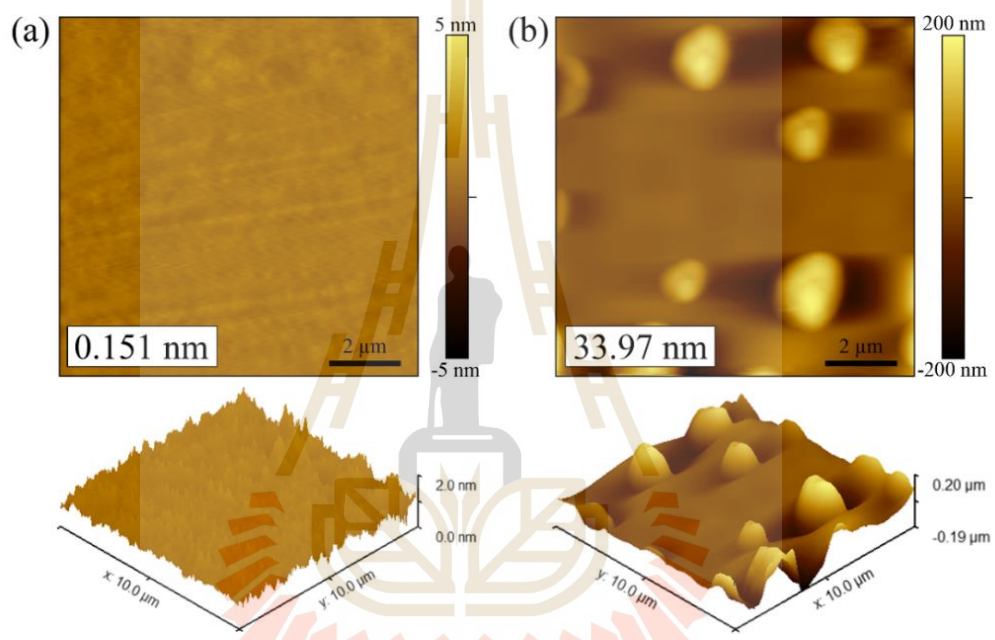


Figure 5.3 The AFM morphology of (a) the pristine MgO thin film and (b) the hydrated MgO thin film (all $10 \times 10 \mu\text{m}^2$).

To investigate the dehydration behavior of the MgO thin film, the films were annealed at 250, 300, 350 and 400°C in air, Ar and N_2 . The topography of the annealed MgO thin films is compared in Figure 5.4 while the change of the MgO thin film surface roughness of all samples is plotted in the graph and shown in Figure 5.5. The results indicate that temperature and atmosphere during the annealing process strongly affect the dehydration behavior of the MgO thin film. It is found that an

increase in the annealing temperature leads to a decrease in the number of clusters and surface roughness in the MgO thin film. At the annealing temperature of 350°C in the Ar atmosphere, it is clearly seen that the clusters almost completely disappear and the surface roughness drops to 0.577 nm while those in the N₂ atmosphere and in the air, the clusters are still detected. Then, after increase annealing temperature to 400°C, the clusters are still predominant in sample annealed in air, while those annealed in Ar atmosphere are completely removed. This reflects that the annealing in Ar atmosphere better improves the morphology of the film than the annealing in N₂ and in air, respectively.

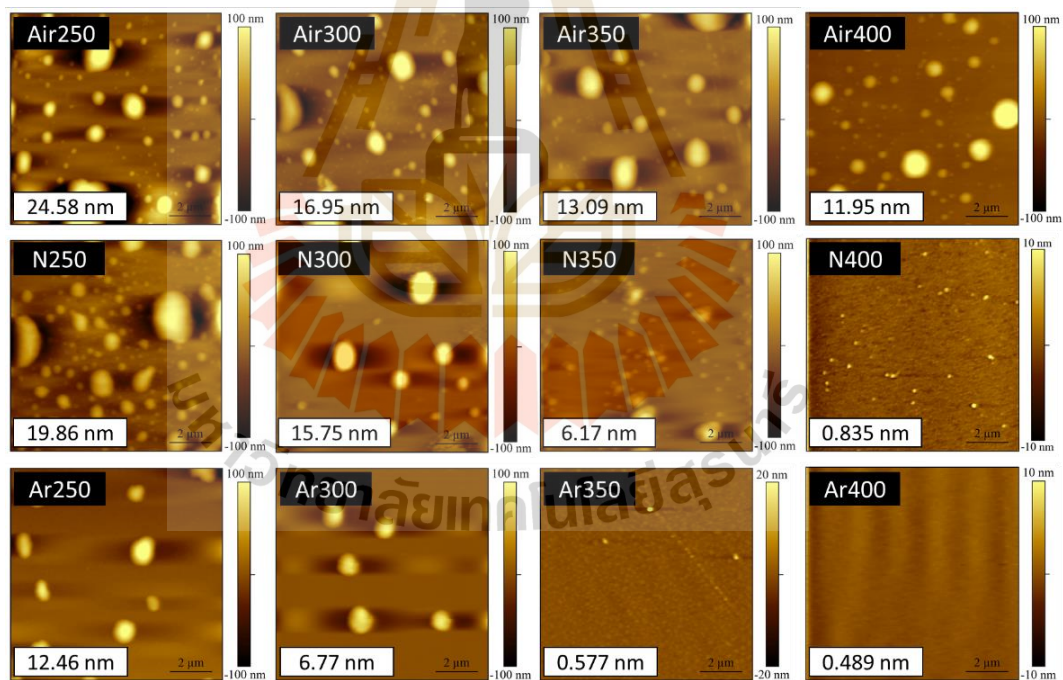


Figure 5.4 10×10 μm² AFM scan on the MgO thin film after being annealed at 250, 300, 350, 400°C (a) in air, (b) in N₂ atmosphere and (d) in Ar atmosphere.

The reason that annealing in Ar gas can improve the film surface roughness could be assumed that flowing an inert gas into the annealing chamber may prevent contaminations and unwanted reactions during the annealing process (Takahashi, 2003; Ye, 2013). Furthermore, with the excellent thermal conductivity of the Ar gas, it could thoroughly disperse the thermal in furnace resulting in the improvement of the film surface roughness (Neyrat, 2003).

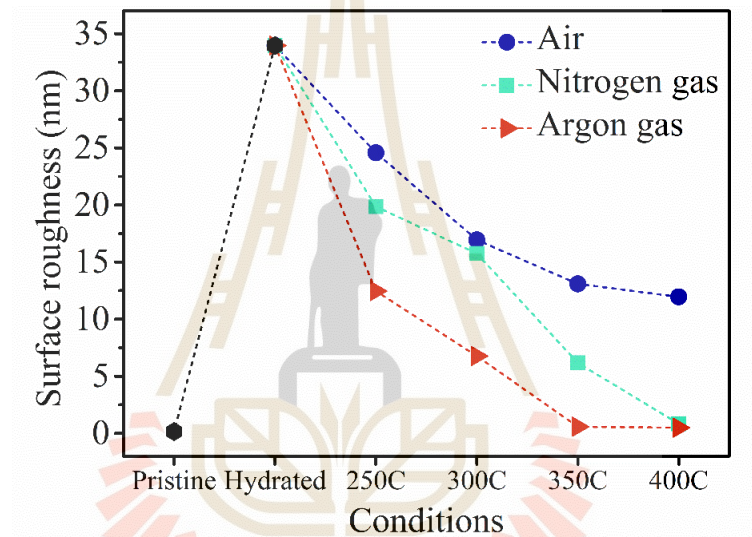


Figure 5.5 The change of surface roughness of the pristine MgO thin film, the hydrated MgO thin film and the films after being annealed in different conditions.

5.3.2 Thickness of the Film

5.3.2.2 X-Ray Reflectivity (XRR)

XRR was used to determine the thickness of the MgO thin film and the thickness of the Mg(OH)₂ layer which forms over the MgO thin film. The obtained XRR spectra are fitted using the GenX program and exhibits in Figure 5.6(a),

(b) and (c). Then, the thickness of the MgO thin film and Mg(OH)₂ layer obtained from the fitting of the XRR spectra of all samples are listed in Table 5.1.

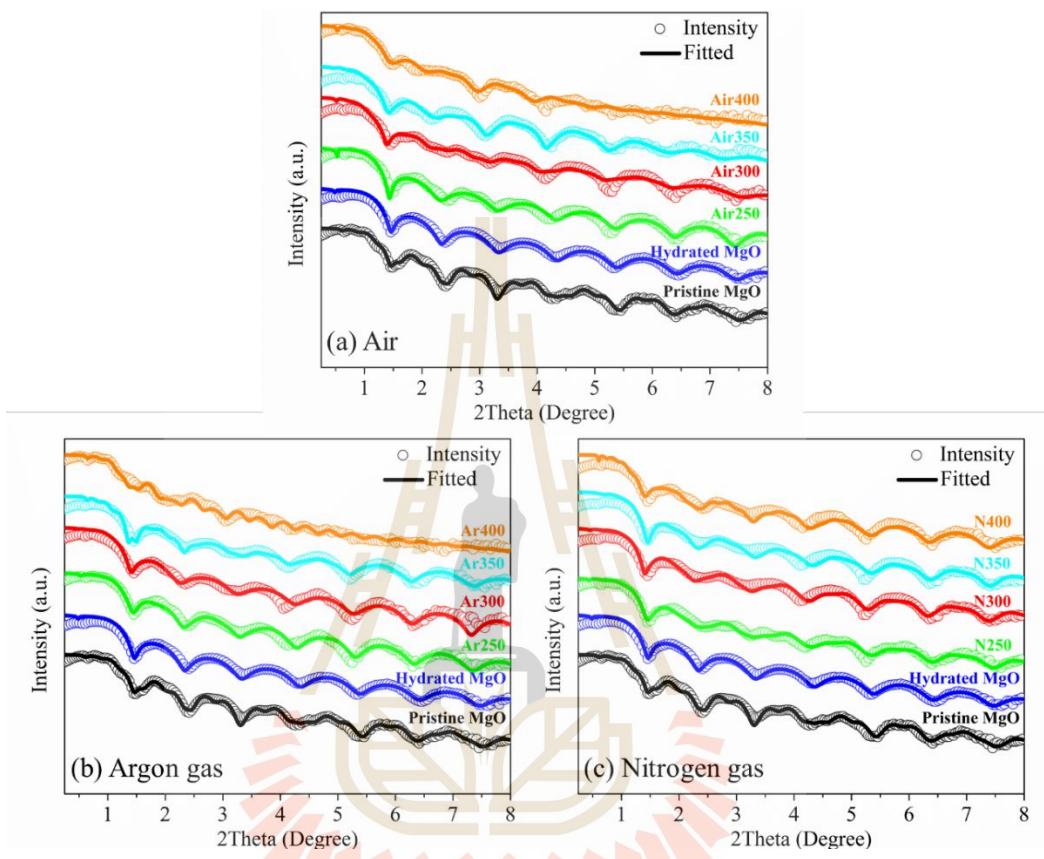


Figure 5.6 A comparative of the XRR spectra of the pristine MgO thin film, the hydrated MgO thin film and the film annealed in (a) air, (b) Ar atmosphere and (c) N₂ atmosphere.

The results show that prior to exposure to a humid environment, the thickness of the MgO thin film is 20.31 nm. However, after the film was exposed to the humid environment, it is found that the thickness of the film increase to 25.50 nm while this comprises 10.19 nm thickness of MgO thin film and 15.31 nm thickness of Mg(OH)₂ layer. The increase in the film thickness could be a result of volume

expansion during the conversion of cubic MgO to hexagonal Mg(OH)₂ (Ali and Al-Mowali, 2013; Amaral, 2011; Dobrzanski, 2020).

Table 5.1 The thickness of all sample obtained from the fitting of XRR spectra

Sample	Thickness (nm)			
	MgO	Mg(OH) ₂	Total	
Pristine MgO thin film	20.31	0	20.31	
Hydrated MgO thin film	10.19	15.31	25.50	
Air	250°C	12.91	11.49	24.40
	300°C	14.47	10.41	24.88
	350°C	15.70	8.65	24.35
	400°C	17.89	6.06	23.95
N ₂ gas	250°C	10.79	14.91	25.70
	300°C	15.78	10.19	25.97
	350°C	16.17	8.27	24.44
	400°C	18.61	2.65	21.26
Ar gas	250°C	12.94	10.13	23.07
	300°C	13.87	9.23	23.10
	350°C	15.17	7.95	23.12
	400°C	19.43	1.09	20.52

Then, after the films were annealed in various conditions, the thickness of the film decrease with an increase of annealing temperature. It is found that the thickness of the film annealed in Ar atmosphere is less than that of the film annealed in N₂ atmosphere and in air. This could confirm that annealing in Ar atmosphere does not only improve the surface roughness of the film, but it also increases the thickness of the MgO thin film.

To understand the dehydration behavior of the MgO thin film, the change in the thickness of the MgO thin film and the Mg(OH)₂ layer are plotted as a graph as shown in Figure 5.7. The result exhibits that the MgO thin film thickness increases while the thickness of Mg(OH)₂ decreases. It is also observed that the

decrease of $\text{Mg}(\text{OH})_2$ layer strongly depends on the temperature and atmosphere during the annealing process. It is found that the thickness of the film almost completely recovers after annealing at 400°C in Ar atmosphere; the thickness of the MgO thin film grows to 19.43 nm while the thickness of the $\text{Mg}(\text{OH})_2$ layer falls to 1.09 nm. The increase of the MgO thin film and decrease of the $\text{Mg}(\text{OH})_2$ could be attributed to the decomposition of water molecules that occur during the annealing process.

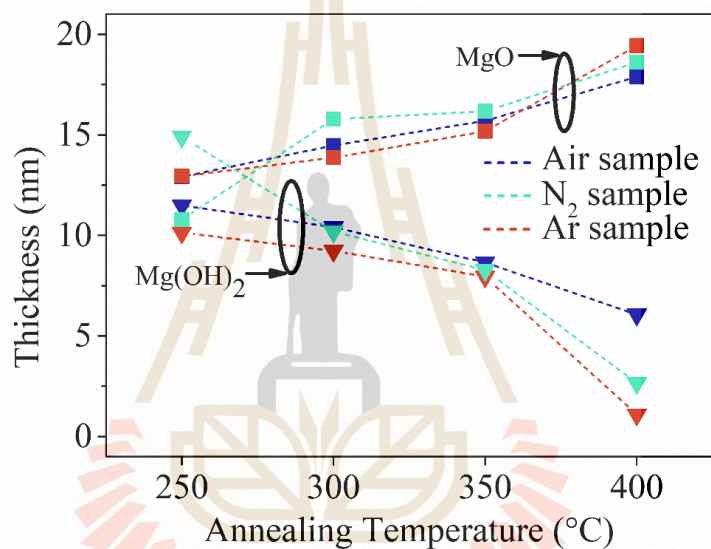


Figure 5.7 Thickness of MgO thin films and $\text{Mg}(\text{OH})_2$ layer after being annealed at 250, 300, 350 and 400°C in air, N_2 atmosphere and Ar atmosphere.

5.3.2.2 Transmission Electron Microscope (TEM)

TEM was used as a complementary technique to XRR to provide a direct view of the change in thickness and the structural evolution of the MgO thin film. The high magnification cross-sectional TEM images of the pristine MgO thin film and the hydrated MgO thin film are exhibited in Figure 5.8. The visual estimations of the range of the film thickness are indicated by a red arrow. The TEM results confirm

that before the hydration process, the thickness of the pristine MgO thin film is 20.28 nm. After the film is kept in the humid box for 24 hours, the thickness of the film rises up to 22.53 nm. This is in line with the thickness of the hydrated MgO thin film obtained from the XRR results.

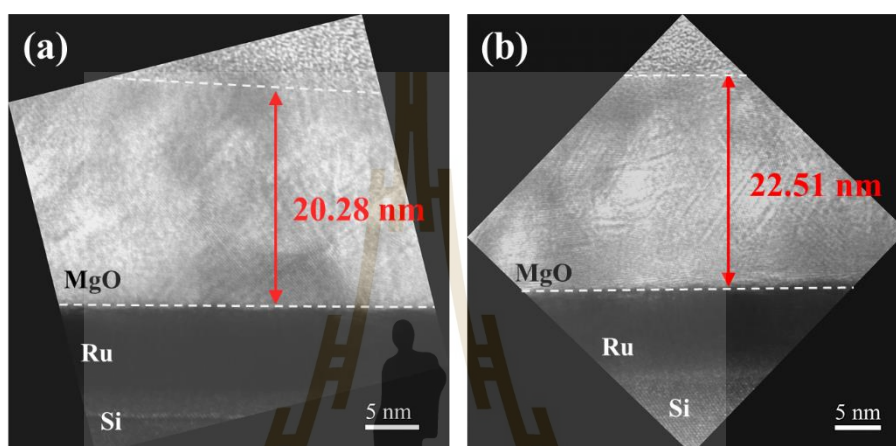


Figure 5.8 High magnification cross-sectional TEM images of (a) the pristine MgO thin film (b) the hydrated MgO thin film.

The TEM was used to verify the change in thickness of the films which is annealed at 350 and 400°C in air, N₂ atmosphere and Ar atmosphere. Figure 5.9 illustrates the cross-sectional TEM images of those samples. The results indicate that the thickness of the hydrated MgO thin film decrease with an increase of annealing temperature. It is further found that at the same annealing temperature, the decreasing of the film thickness of the sample annealed in the Ar atmosphere is greater than that of the other annealing atmosphere. These results are also in agreement with the results obtained by XRR analysis in section 5.3.2.1

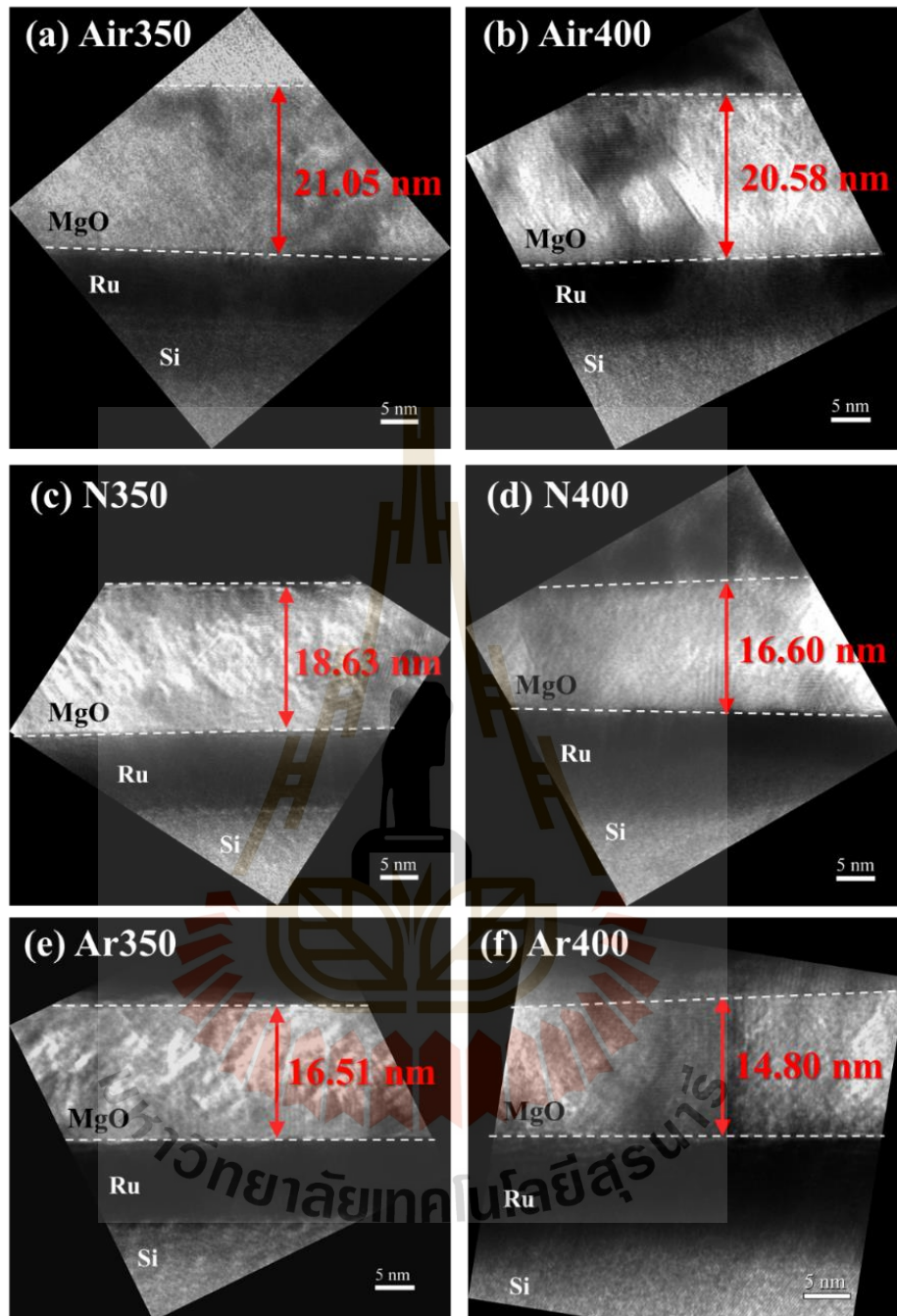


Figure 5.9 The cross-sectional TEM images of MgO thin films after being annealed at 350 and 400°C in air, in N₂ atmosphere and in Ar atmosphere.

5.3.3 Electronic Structure of the MgO Thin Film

The normalized Mg K-edge XANES spectra of the pristine MgO thin film, the hydrated MgO thin film and the samples annealed in N₂ atmosphere and in Ar atmosphere are exhibited in Figure 5.10 and Figure 5.11. The XANES spectrum obtained from the pristine MgO thin film is in perfect agreement with Mg K-edge XANES spectrum of MgO reported by Khamkongkaeo *et al.* (2018), Yoshida *et al.* (1995) and Yoshimura *et al.* (2013). The Mg-edge XANES spectra can be described by three features as labeled A, B and C. It is known that the shift of the feature A is the signature of the transition of electrons from 1s to an unoccupied bound 3p-like state. However, no energy shift was observed in all spectra.

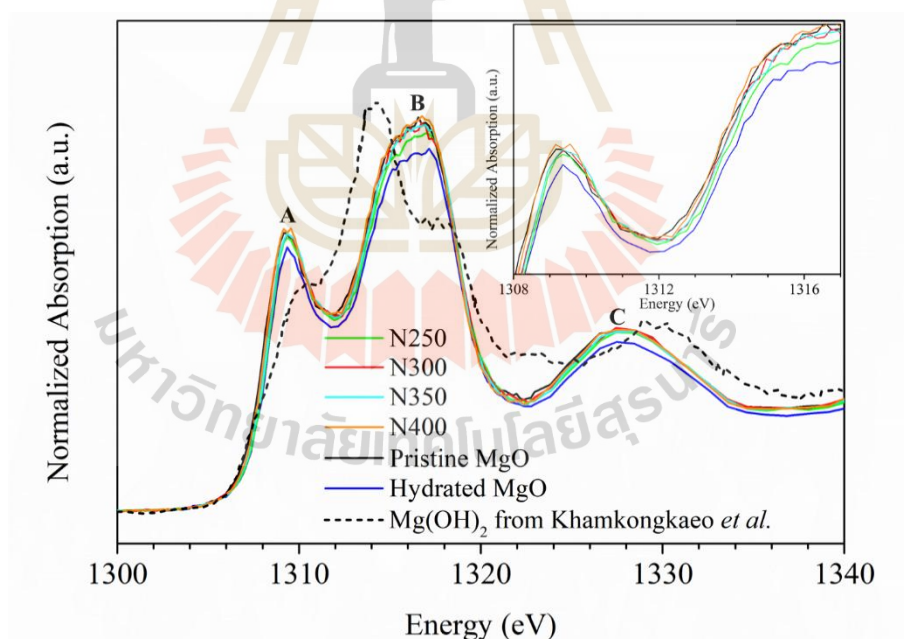


Figure 5.10 The normalized Mg K-edge XANES spectra of the MgO thin films annealed in N₂ atmosphere at different temperatures.

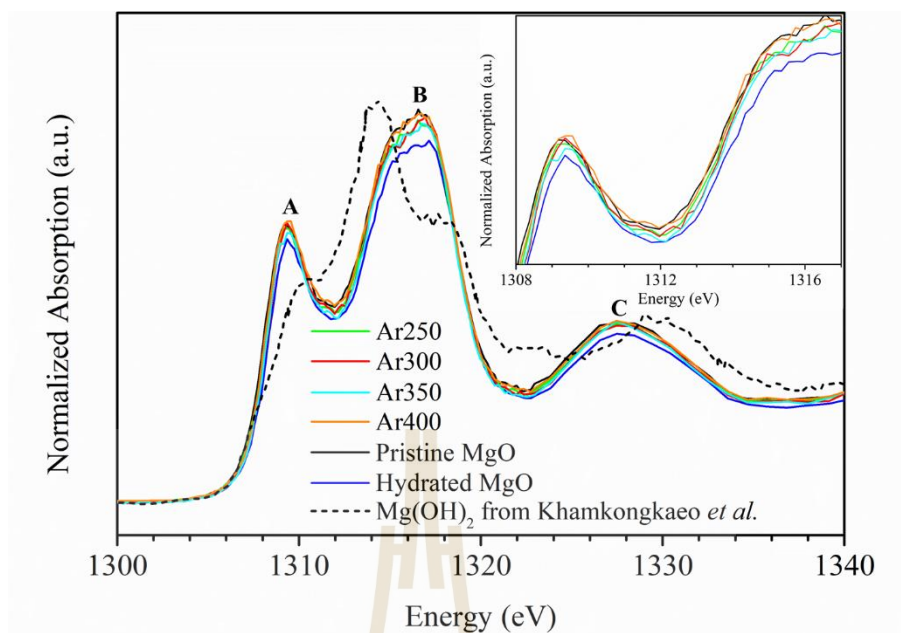


Figure 5.11 The normalized Mg K-edge XANES spectra of the MgO thin films annealed in Ar atmosphere at different temperatures.

In order to interpret the XANES spectrum of the hydrated MgO thin film, the feature of this spectrum is compared to the XANES spectrum of $\text{Mg}(\text{OH})_2$ reported by Khamkongkaeo et al. (2018). It is expected that the $\text{Mg}(\text{OH})_2$ layer forms over the MgO thin film surface after it was exposed to humid environment. However, the results reveal that the XANES spectrum feature of the hydrated MgO thin film, which contains $\text{Mg}(\text{OH})_2$ over the surface, is quite different from the XANES spectrum of $\text{Mg}(\text{OH})_2$ reported by Khamkongkaeo et al. (2018). It is instead found that the XANES spectra feature of the hydrated MgO thin film is similar to the XANES spectra of the MgO thin film, but its intensity is lower than that of the MgO thin film. This is possibly because after the film exposed to humid, only a part of the film transforms to $\text{Mg}(\text{OH})_2$ as detected by the XRR (Section 5.3.2.2).

Considering the XANES spectra obtained from the samples annealed in N_2 gas (Figure 5.10) and the samples annealed in Ar atmosphere (Figure 5.11), it is found that after the films were annealed, the intensity of the XANES spectra increase with an increase of annealing temperature. At the annealing temperature of $400^\circ C$, the intensity of XANES spectra obtained from both gas atmospheres are similar to the XANES spectra obtained from the pristine MgO thin film.

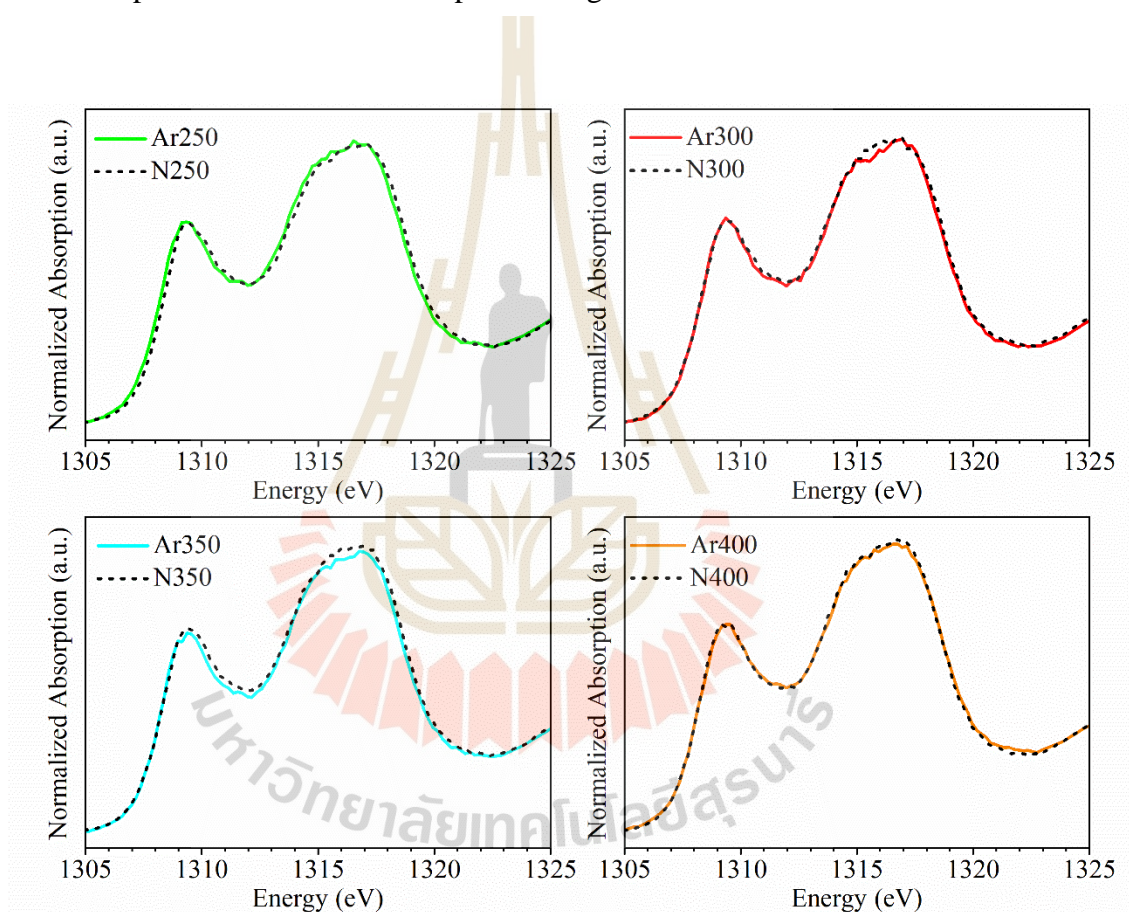


Figure 5.12 A comparative Mg K-edge XANES spectra of samples annealed at same annealing temperature in N_2 atmosphere and in Ar atmosphere.

To understand the effect of atmosphere on the dehydration of MgO thin film, the normalized Mg K-edge XANES spectra obtained from the samples annealed

in Ar atmosphere and in N₂ atmosphere, are presented in Figure 5.12. Although we observed that the change in the XANES spectra of the film after the film was annealed, at the same annealing temperature, it seems like that there is no significant difference in feature between samples annealed in N₂ atmosphere and Ar atmosphere. This may imply that the electronic structure of the film annealed in Ar atmosphere and N₂ atmosphere is similar.

5.3.4 Dehydration Mechanism of the MgO Thin Film

From the overall results, the possible dehydration mechanism of MgO thin film is concluded and displayed as a schematic drawing in Figure 5.13. After the MgO thin film is exposed to the humid environment, the film absorbs the molecules of water from the surrounding and hydrates by forming the Mg(OH)₂ clusters over its surface (as observed in the AFM image).

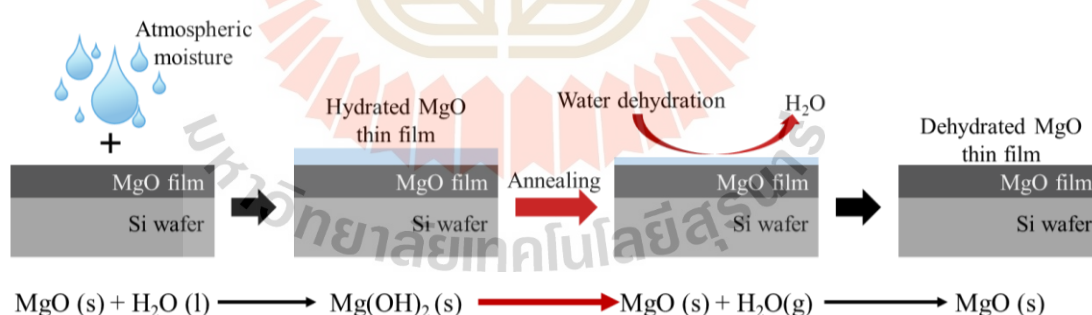


Figure 5.13 A schematic drawing of the dehydration mechanism of the hydrated MgO thin film.

After the films are annealed at different temperatures in different atmospheres, the water molecule can be reversibly driven off from the film leading to

the dehydration of hydroxide hence MgO thin film formation. The reversible hydration and dehydration reaction of the MgO thin film can be expressed in the Equation (5.2)



5.4 Chapter Summary

In this chapter, the role of annealing temperature and annealing atmosphere on the dehydration characteristic of the MgO thin film is investigated. Results demonstrate that hydration reaction can induce the volume expansion in the film leading to the increase of the film thickness and film surface roughness. However, after the films were annealed at different temperatures and atmospheres, it is found that the surface roughness and thickness of the film can be recovered. This is probably because the annealing could drive off molecules of water leading to the dehydration of the hydroxide layer. Results obviously reflect that after being annealed at 400°C in Ar atmosphere, the surface roughness and thickness of the film can be recovered. The possible reason is that the inert of the Ar gas act as a protective layer that prevents contamination and/or humidity from the air which react with the film during the annealing process. The information obtained in this study could be a guideline for the protection and development in the manufacturing process of devices containing MgO thin film.

5.5 References

Ali, A. M., and Al-Mowali, A. H. (2013). Ceramic expansion by water layers on magnesium oxide: AB Initio Study. **Am. J. Mater. Sci.** 1: 50-53.

- Amaral, L. F., Oliveira, I. R., Bonadia, P., Salomao, R., and Pandolfelli, V. C. (2011). Chelants to inhibit magnesia (MgO) hydration. **Ceram. Int.** 37: 1537-1542.
- Dobrzanski, L. Bamberger, A. M., and Totten, G. E. (2020). **Magnesium and Its Alloys: Technology and Applications**. Florida: CRC Press Taylor & Francis Group.
- Gay, Ian D., and Harrison, N. M. (2005). A density functional study of water and methanol chemisorption on MgO(110). **Surf. Sci.** 591: 13-22.
- Hill, M. R., Jones, A. W., Russell, J. J., Roberts, N. K., and Lamb, R. N. (2004). Dialkylcarbamato magnesium cluster complexes: precursors to the single-source chemical vapour deposition of high quality MgO thin films. **J. Mater. Chem.** 14: 3198-3202.
- Khamkongkao, A., Klysubun, W., Boonchuduang, T., Sailuam, W., Sriwattanac, P., and Phetrattanarangsia, T. (2018). X-ray Absorption Spectroscopy Investigation of Relationship Between Mg Vacancy and Magnetic Properties of MgO powder. **J. Magn. Mater.** 460: 327-333.
- Kurosawa, R., Takeuchi, M., and Ryu, J. (2019). Comparison of the Effect of Coaddition of Li Compounds and Addition of a Single Li Compound on Reactivity and Structure of Magnesium Hydroxide. **ACS Omega.** 4(18): 17752-17761.
- Lee, J. H., and Eun, J. H. (2003). Hydration behavior of MgO single crystals and thin films. **J. Mater. Res.** 18(12): 2895-2903.
- L'vov, B. V., Novichikin, A. V., and Dyakov, A. O. (1998). Mechanism of thermal decomposition of magnesium hydroxide. **Thermochim. Acta.** 315: 135-143.

- Moon, S. H., Heo, T. W., Park, S. Y., Kim, J. H., and Kim, H. J. (2007). The Effect of the Dehydration of MgO Films on their XPS Spectra and Electrical Properties. **J. Electrochem. Soc.** 154(12): J408-J412.
- Neyret, E., Arene, E., and Ecartot, L. (2003). **Process for improving the surface roughness of a wafer.** France: WO2005055308A1.
- Oka, Y., Yokoyama, M., and Dairaku, T. (1988). **Method of carrying out chemical dehydration reaction and an apparatus therefor.** United States: US477882A.
- Pass, G., and Sutcliffe, H. (1974). **Practical Inorganic Chemistry.** Netherlands: Springer.
- Stanish, M. A., and Perlmutter, D. D. (1983). Kinetics and transport effects in the dehydration of crystalline potassium carbonate hydrate. **AIChE Journal.** 29(5): 806-812.
- Takahashi, S. (2003). **Method for continuous heat-treatment of metals under argon atmosphere.** United States: US20030000611A1.
- Ye, Z., Zhang, R., and Sun, X. (2013). Bustling argon: biological effect. **Med Gas Res.** 3: 22.
- Yim, T., Kim, H. S., and Lee, J. Y. (2018). Cyclic Assessment of Magnesium Oxide with Additives as a Thermochemical Material to Improve the Mechanical Strength and Chemical Reaction. **Energies.** 11: 2366.
- Yoshida, T. Tanaka, T., Yoshida, H., Funabiki, T., and Yoshida, S. (1995). Study of Dehydration of Magnesium Hydroxide. **J. Phys. Chem.** 99: 10890-10896.
- Yoshimura, T., Tamenori, Y., Iwasaki, N., Hasegawa, H., Suzukie, A. and Kawahata H. (2013). Magnesium K-edge XANES spectroscopy of geological standards. **J. Synchrotron. Radiat.** 20: 734-740.

CHAPTER VI

GENERAL DISCUSSION

This chapter presents a general discussion of an overview of the major findings of this thesis based on the existing literature review and the hypotheses proposed in **Chapter 1**.

6.1 Influence of Gas Atmosphere on the Dissolution Behavior of Magnesium Oxide Thin Film

The influence of the gas atmosphere on the dissolution behavior of the magnesium oxide (MgO) thin film was investigated and demonstrated in detail in **Chapter 3**. In this section, the findings are discussed to address the postulated hypothesis. The MgO thin films were exposed to deionized water which saturated by different gas including nitrogen gas (N₂), oxygen gas (O₂) and carbon dioxide gas (CO₂) for either 1 hour or 4 hours. The results indicate that the chemical composition, surface morphology and thickness of the film changes after the interaction with water.

Scanning electron microscopy (SEM) result shows that the MgO thin films create coral-like clusters over its surface after being exposed to deionized water resulting in the change of the film morphology. X-ray photoelectron spectroscopy (XPS) result reveals that after being exposed to deionized water, the MgO thin film absorbs molecules of water over its surface and transforms its chemical composition into Mg(OH)₂ because the bonding of O–OH is observed after the deconvolution of O 1s

spectra. After sputtering into the deeper layer of the film, the bonding of O–OH in the O 1s spectra is still detected. This implies that water does not absorb only over the film surface, but it can infiltrate into the deeper layer of the film. XPS depth profile results further indicate that the interaction with water can also result in a decrease in the film thickness. It is found that at the same immersion time, the thickness of the film dramatically decreases in CO₂-saturated DI water and it slightly decreases in N₂-saturated DI water. The results of the remaining thickness of the film obtained using a focused ion beam equipped with scanning electron microscopy (FIB-SEM) also confirm that the thickness of MgO thin film is thinnest in the dissolution under CO₂ gas.

The observation of the increase of Mg concentration in deionized water obtained from the dissolution process using atomic absorption spectroscopy (AAS) suggests that the MgO thin film dissolves in deionized water by releasing of Mg²⁺ ions and OH⁻ ions into the water while the highest concentration of Mg is obtained from the dissolution under CO₂ gas and lowest in the dissolution under N₂ gas. This is because the different gas atmospheres affect the deionized water pH differently. It is found that the CO₂ gas can react with the molecules of water and produces carbonic acid/bicarbonic acid resulting in the reduction of the pH value of deionized water, while on the other hand, N₂ gas has no reaction with the deionized water.

The overall results confirm that the dissolution reaction could cause the changes in thickness, morphology and chemical composition of the MgO thin films. Furthermore, the dissolution behavior of the MgO thin film strongly depends on the gas atmosphere used during the dissolution process.

6.2 Effect of Water Temperature on the Dissolution Behavior of Magnesium Oxide Thin Film

In order to expand our understanding of the dissolution behavior of the MgO thin film, in **Chapter 4**, the effect of water temperature on the dissolution of the MgO thin film was studied.

SEM images show that the films form clusters over its surface while an increase in water temperature can cause an increase in the number of clusters. Furthermore, the XPS results point out that the chemical composition of the film transforms into $\text{Mg}(\text{OH})_2$, not only over the surface of the film but also at the deeper layer of the film. XPS depth profile and FIB-SEM cross-sectional results further exhibit that the water temperature strongly affects the decrease of the film thickness. It is found that the thickness of the film thinnest in sample MgO-75. This is because an increase in water temperature enhances the kinetic energy of the molecules of water. Therefore, the probability of water molecules interacts with the MgO film is greater in high-temperature water. The results prove that the increase of water temperature enhances the kinetic energy of the molecules of water resulting in the increase of dissolution rate of the MgO thin film.

6.3 Role of Temperature and Atmosphere on the Dehydration Characteristic of Magnesium Oxide Thin Film

Besides the dissolution reaction, in this chapter, we investigate the role of temperature and atmosphere on the dehydration characteristic of the MgO thin film. The results obtained in **Chapter 5** reflect that the hydration could cause the formation

of clusters over the MgO thin film surface resulting in the increase of the film thickness and surface roughness.

Atomic force microscopy (AFM) images show that the number of clusters, which form over the MgO thin film surface after being exposed to a humid environment, reduces after the films were annealed. This results in a decrease in the surface roughness of the MgO thin film. It is further found that the decrease in the number of clusters and surface roughness strongly depend on the temperature and atmosphere used. X-ray reflectivity (XRR) results reveal that the thickness of the film tend to decrease with an increase of annealing temperature while the annealing at 400 in Ar atmosphere, the thickness of the film can return to having a similar thickness to a pristine sample. This is in agreement with the results receive from the transmission electron microscopy (TEM). The improvement of the film surface roughness and thickness could be a result of the decomposition of the water molecules which absorb over the film surface.

Overall results confirm that the dehydration could lead to the decomposition of the water molecules resulting in the recovery of the film surface roughness and thickness. It further found that the annealing temperature and annealing atmosphere play a crucial on the dehydration characteristic of the MgO thin film.

CHAPTER VII

CONCLUSION AND FUTURE PERSPECTIVES

This chapter is the conclusion of the dissertation. It also presents the perspectives for the future work.

7.1 General Conclusions

The goals of this thesis are to acquire extensive knowledge of dissolution and dehydration mechanism of the MgO thin film used in MTJs of magnetic sensors in HDDs. In this thesis, all testing systems were designed to be comparable to the wet cleaning and polishing process of the HDDs manufacture. The aspects of the mechanisms obtained from these studies have been elucidated.

The main findings of this thesis are concluded and listed below.

1. From the study of the influence of gas atmospheres on the dissolution behavior of MgO thin film in **Chapter 3**, it is found that the dissolution reaction begins with the absorption of the molecules of water into the deeper layer of the MgO thin film. This reaction transforms the chemical composition of the film into $\text{Mg}(\text{OH})_2$ and subsequently dissolves by releasing Mg^{2+} ions and OH^- ions into water resulting in the decrease of the film thickness. Results reveal that the dissolution rate of this film strongly depends on the immersion time and the gas atmosphere because each gas reacts with water differently. It is found that the thickness of the MgO thin films after being exposed to CO_2 gas-saturated deionized water dramatically decreases while those were exposed to O_2 and N_2 gas-saturated deionized water slightly reduce. This is because the

CO₂ can interact with the molecules of water and produce H₂CO₃/HCO₃⁻ acid leading to the reduction of the pH value of deionized water; on the other hand, N₂ has no reaction with the deionized water. These results obtained in this study fully support the hypothesis which we purposed in **Chapter 1** (section 1.3.1) stated that the gas could change the chemistry and pH of water and could affect the dissolution rate of the MgO thin film. The CO₂ gas could induce the decrease of water pH leading to the increase of dissolution rate of the MgO thin film.

2. In **Chapter 4**, the investigation of the effect of water temperature on the dissolution mechanism of the MgO thin film reveals that the temperature of water significantly affects the dissolution behavior of the MgO thin film. The results correspond to the hypothesis which we proposed in section 1.3.2 that the water temperature relates to the kinetic energy of water. Low temperature could lead to low kinetic energy and subsequently low dissolution rate. We found that an increase in water temperature enhances the kinetic energy of the molecules of water resulting in the increase of dissolution rate. At the higher temperature of water, the thickness of the film decreases faster than that of the film exposed to water at the lower temperature. Finally, the qualitative model is purposed to explain the effect of the water temperature of the MgO thin film.

3. The investigation of the dehydration behavior of the MgO thin film, as showed in **Chapter 5**, was hypothesized that the thermal decomposition of water in the hydroxide Mg(OH)₂ could lead to the recovery of the microstructure/crystal structure, surface roughness and thickness of the MgO thin film. The results obtained in this study indicates that after the MgO thin films were annealed at various annealing temperatures, the surface roughness and the thickness of the MgO thin film can be recovered. It is

further found that the dehydration behavior of the MgO thin film strongly depends on the annealing temperature and atmosphere. The result shows that annealing in the inert gas atmosphere can improve the surface roughness and thickness of the MgO thin film better than annealing in air does. This is because the inert gas may act as a protective layer preventing contaminations and/or moistures that may react with the film during annealing.

4. The basic principle, advantages, and limitations of characterization techniques that were used in this thesis including XPS, XRR, XAS and TEM are reviewed and summarized in a comparative way (**Chapter 2**). This review could be fruitful information and guideline for the researchers who would like to apply such techniques for thin film characterization.

7.2 Future Perspectives

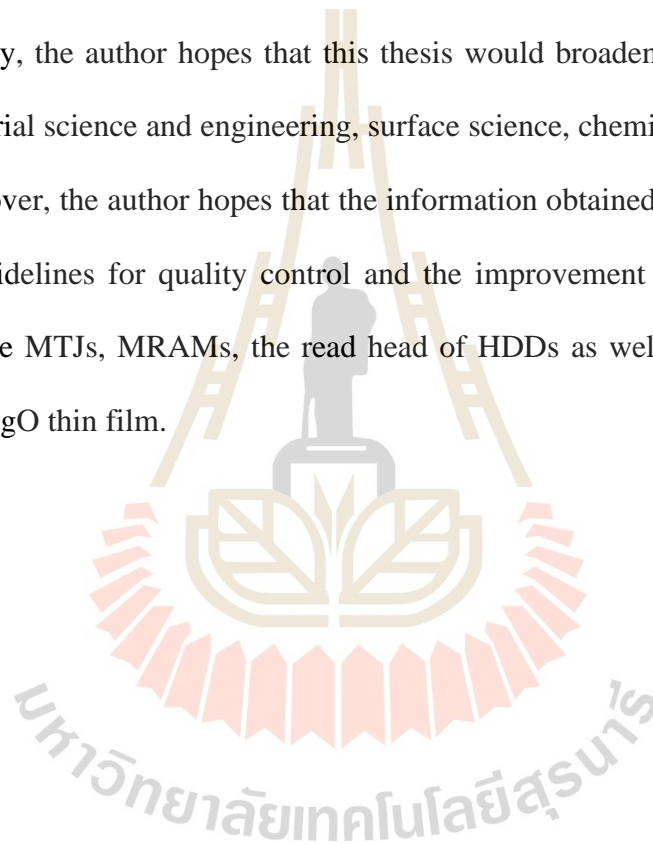
This thesis successfully investigates the dissolution and dehydration behaviors of the MgO thin film. The results obtained in this thesis provide the basic knowledge of the influence of environment (e.g. temperature and atmosphere) on mechanism of dissolution and dehydration of the MgO thin film.

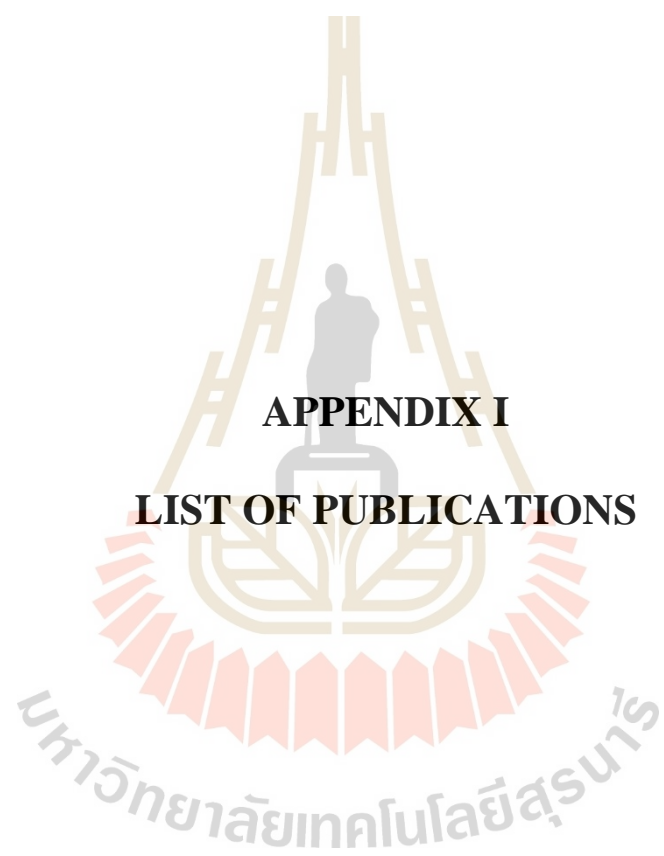
The following recommendations are for the future studies.

1. In this thesis, the author obtained an understanding of the dissolution mechanism of MgO thin film in water. Therefore, it would be of interest to extend the framework to consider the dissolution reaction of the MgO thin film in other solutions, for example, acetone, ethanol, methanol because various types of lubricants and/or solutions are used in the cleaning or polishing processes.

2. This thesis reported the impact of dissolution and dehydration reactions on the thickness, chemical composition and surface morphology of the film. Therefore, it would be of great interest to further investigate the other properties of the MgO thin film including mechanical properties and electrical properties because this could be a useful information for the manufacturing process of devices containing MgO thin film, such as MTJs, MRAMs and read head of HDDs.

Finally, the author hopes that this thesis would broaden understanding in the field of material science and engineering, surface science, chemistry, and other related fields. Moreover, the author hopes that the information obtained from this work could be useful guidelines for quality control and the improvement of the manufacturing process of the MTJs, MRAMs, the read head of HDDs as well as the other devices containing MgO thin film.



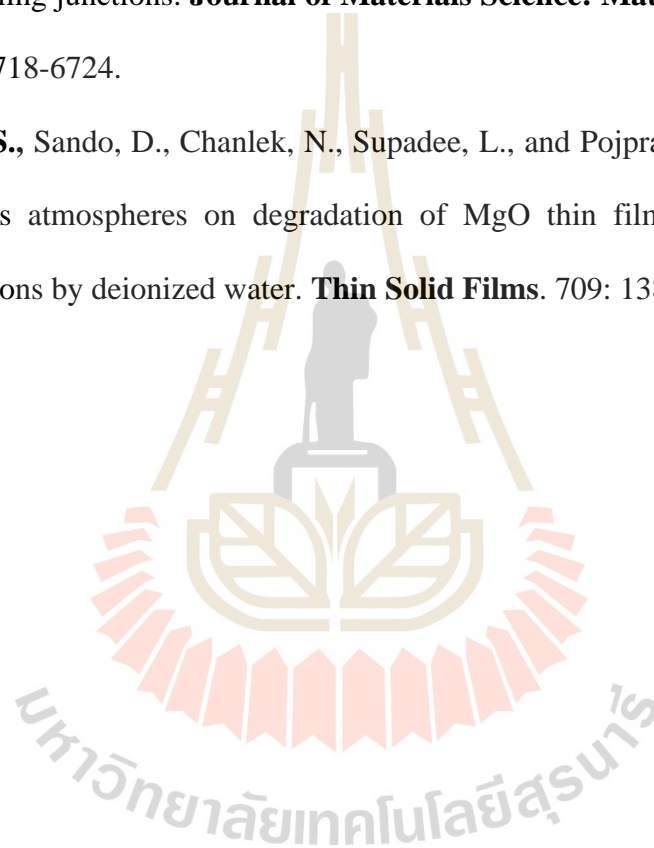


APPENDIX I

LIST OF PUBLICATIONS

List of Publications

1. **Tigunta, S.**, Khlikhum, P., Kidkhunthod, P., Chanlek, N., Supadee, L., and Pojprapai, S. (2019). Dissolution behavior of MgO thin film-barrier magnetic tunneling junctions. **Journal of Materials Science: Materials in Electronics**. 30: 6718-6724.
2. **Tigunta, S.**, Sando, D., Chanlek, N., Supadee, L., and Pojprapai, S. (2020). Effect of gas atmospheres on degradation of MgO thin film magnetic tunneling junctions by deionized water. **Thin Solid Films**. 709: 138185.



BIOGRAPHY

Siriporn Tigunta was born on June 2, 1988, in Chiang Mai, Thailand. In 2011, She received her bachelor's degree in Materials Science from Physics and Materials Department, Faculty of Science, Chiang Mai University. In the same year, she continued her studies in a master's degree in Materials Science at Chiang Mai University. Then, after graduating from her master's degree in 2013, she has been employed under the position of an assistant researcher by Doc choo's Management Pte., Ltd. In 2015, she decided to come back to continue her studies as a Ph.D. candidate in the Materials Engineering Program, Institute of Engineering, Suranaree University of Technology.

